

WIRELESS POWER TRANSFER

Fundamentals and Technologies



Eugen Coca, editor

Wireless Power Transfer Fundamentals and Technologies

Edited by Eugen Coca

Wireless Power Transfer: Fundamentals and Technologies

Edited by Eugen Coca

Published by ExLi4EvA

Copyright © 2016

All chapters are Open Access distributed under the Creative Commons Attribution 3.0 license, which allows users to download, copy and build upon published articles even for commercial purposes, as long as the author and publisher are properly credited, which ensures maximum dissemination and a wider impact of our publications. After this work has been published, authors have the right to republish it, in whole or part, in any publication of which they are the author, and to make other personal use of the work. Any republication, referencing or personal use of the work must explicitly identify the original source.

As for readers, this license allows users to download, copy and build upon published chapters even for commercial purposes, as long as the author and publisher are properly credited, which ensures maximum dissemination and a wider impact of our publications.

Notice

Statements and opinions expressed in the chapters are those of the individual contributors and not necessarily those of the editors or publisher. No responsibility is accepted for the accuracy of information contained in the published chapters. The publisher assumes no responsibility for any damage or injury to persons or property arising out of the use of any materials, instructions, methods or ideas contained in the book.

Publishing Process Manager

Technical Editor

Cover Designer

AvE4EvA MuViMix Records

First published June 30, 2016

ISBN-10: 953-51-2468-4

ISBN-13: 978-953-51-2468-9

Print

ISBN-10: 953-51-2467-6

ISBN-13: 978-953-51-2467-2

Contents

Preface

Chapter 1 Fundamentals of Inductively Coupled Wireless Power Transfer Systems
by Ali Abdolkhani

Chapter 2 Analysis of Wireless Power System Efficiency in Dependency on Configuration of Resonant Tank
by Michal Frivaldsky, Pavol Spanik, Peter Drgona, Viliam Jaros and Marek Piri

Chapter 3 Wireless Power Transfer by Using Magnetically Coupled Resonators
by Ali Agcal, Selin Ozcira and Nur Bekiroglu

Chapter 4 Innovative Wireless Power Receiver for Inductive Coupling and Magnetic Resonance Applications
by Young-Jun Park, Hongjin Kim, Hyung-Gu Park and Kang-Yoon Lee

Chapter 5 Microwave Power Transmission Based on Retro-reflective Beamforming
by Xin Wang and Mingyu Lu

Chapter 6 A Review of Dynamic Wireless Power Transfer for In - Motion Electric Vehicles
by Kai Song, Kim Ean Koh, Chunbo Zhu, Jinhai Jiang, Chao Wang and Xiaoliang Huang

Preface

Wireless power transfer techniques have been gaining researchers' and industry attention due to the increasing number of battery-powered devices, such as mobile computers, mobile phones, smart devices, intelligent sensors, mainly as a way to replace the standard cable charging, but also for powering battery-less equipment.

The storage capacity of batteries is an extremely important element of how a device can be used. If we talk about battery-powered electronic equipment, the autonomy is one factor that may be essential in choosing a device or another, making the solution of remote powering very attractive.

A distinction has to be made between the two forms of wireless power transmission, as seen in terms of how the transmitted energy is used at the receiving point:

- Transmission of information or data, when it is essential for an amount of energy to reach the receiver to restore the transmitted information;
- Transmission of electric energy in the form of electromagnetic field, when the energy transfer efficiency is essential, the power being used to energize the receiving equipment.

The second form of energy transfer is the subject of this book.

Fundamentals of Inductively Coupled Wireless Power Transfer Systems

Ali Abdolkhani

Additional information is available at the end of the chapter

<http://dx.doi.org/10.5772/63013>

Abstract

The objective of this chapter is to study the fundamentals and operating principles of inductively coupled wireless power transfer (ICWPT) systems. This new technology can be used in various wireless power transfer applications with different specifications, necessities, and restrictions such as in electric vehicles and consumer electronics. A typical ICWPT system involves a loosely coupled magnetic coupling structure and power electronics circuitries as an integrated system. In this chapter, the emphasis is placed on the magnetic coupling structure, which is the most important part of the system. Although this technology has motivated considerable research and development in the past two decades, still there are several theoretical studies such as the level of the operating frequency, operating at high secondary circuit quality factor, coupling efficiency, etc., that need further investigation to fully develop the governing mathematical relationships of this technology.

The chapter begins with an outline about the ICWPT systems highlighting their major application areas, followed by present challenges in the field. Then, the operating principle of such a technology is presented, which includes system tuning, electrical equivalent circuit, power transfer capability, and power losses associated with the system. The chapter ends with detailed derivations of the system coupling efficiency, which is the most important portion of the system efficiency analysis for both series- and parallel-tuned secondary side.

Keywords: Compensation, Coupling efficiency, Inductive power transfer, Magnetic coupling, Power transfer capability, Resonant converters, Wireless power transfer

1. Introduction

Wireless power transfer is to transfer electrical power from one point to another through an air gap without any direct electrical contacts. This technology has been used for applications as in electric vehicles (EVs), consumer electronics, biomedical, etc. where conventional wires are inconvenient, hazardous, unwanted, or impossible. For instance, supplying electrical power using mechanical slip-rings in rotary applications results in a system with a reduced life span because of the frequent maintenance requirements due to wear and tear caused by friction. Moreover, mechanical slip-rings are associated with arcing, which make them unsafe to operate in the presence of explosive gases. Increasing the lifespan, reliability, and low-maintenance operation can be achieved by eliminating the cables, mechanical slip-rings, as well as plugs and sockets.

In the early days of electromagnetism before the electrical-wire grid was deployed, serious interest and effort were devoted (most notably by Nikola Tesla) towards the development of schemes to transfer energy over long distances without any carrier medium. These efforts appear to have met with little success. Radiative modes of omni-directional antennas (which work very well for information transfer) are not suitable for power transfer, because a vast majority of power is wasted into free space. Today, we face a different challenge than Tesla. Now that the existing electrical-wire grids carry power almost everywhere, wireless power transfer technology creates new possibilities to supply portable devices with electrical energy, which has been used in many different applications. A range of applications has been considered and several approaches have been proposed based on the individual requirements. Currently, the main areas of wireless power transfer applications can be categorised as follows [1]:

- Industrial (operation in harsh environment, e.g. mining, next to explosive gases)
- Automotive (electric cars and general battery charging)
- Aerospace (transferring energy to moving parts)
- Consumer electronics (charging a cell phone or a laptop wirelessly)
- Biomedical (inductive interface to power implantable biomedical devices)

2. Present challenges

2.1. Theoretical developments

The aim of an inductively coupled wireless power transfer (ICWPT) system is to provide power to a movable object across a gapped magnetic structure. Its theoretical development relies on both magnetic and power electronics together as an integrated system. In the case of magnetic structure, designing a magnetic coupling structure with a small air gap would result in high magnetic coupling coefficient and increased power transfer capability. Modelling and

representing the magnetic circuit and associate its geometrical characteristics with its electrical behaviour are very important as: (1) to enable predicting the circuit performance and (2) to provide the insight needed to achieve an optimised design. Furthermore, the magnetic structure of an ICWPT system combines the magnetic properties of both an ideal transformer and an inductor. There are more room for theoretical improvements in magnetisation, mutual inductance, leakage inductance, and their connection with the structure geometry and AC losses that are critical in power electronic designs. In ICWPT systems, in order to reduce the skin and proximity effects associated with the coils, multi-strands-woven Litz wire is often used. Modelling and developing functional analysis of such a phenomenon associated with Litz wire are of high importance for the development of an efficient ICWPT system.

Power electronics, on the other hand, covers a large area including electronics, control, and communications. Analysis and modelling of switch-mode non-linear circuits are the main concerns. Like most other power electronic applications, the further development of ICWPT systems depends largely on some fundamental advances in switch-mode non-linear theories. Moreover, the loose magnetic coupling between the primary and the secondary coils of an ICWPT power supply is more difficult to analyse than a traditional closely coupled transformer. This further increases the circuit complexity so that proper compensation and control have to be taken into consideration in the design [2].

2.2. Technical limitations

Because of the air gap, designing an ICWPT system poses some unusual design constraints compared to the traditional compactly coupled design. The relatively large gap in the magnetic circuit results in a low mutual inductance and high leakage inductances. Eddy currents caused by fringing flux can be formed in the magnetic material near the air gap and cause power losses and EMI. Operating at high frequencies presents unique design problems due to the increased core losses, leakage inductance, and winding capacitance. This is because physical orientation and spacing of the windings determine the leakage inductance and winding capacitance which are distributed throughout the windings in the magnetic structure [3]. Experienced SMPS (switch-mode power supply) designers know that SMPS success or failure heavily depends on the proper design and implementation of the magnetic components. Inherent parasitic elements in high-frequency inductive power transfer applications cause a variety of circuit problems including: high power losses, high-voltage spikes necessitating snubbers or clamps, poor cross regulation between multiple outputs, noise coupling to input or output, restricted duty cycle range, etc. [4, 5].

Some major constrains associated with the design and practical implementations are:

- **Meeting the power demand.** It is often difficult to deliver the required power to a load via ICWPT system due to limited space on the receiver side and specific power flow regulations.
- **Switching speed.** Operating at a higher frequency can help reduce the size of an ICWPT system. However, the switching speed of the switches is one of the major constraints. The most suitable switching devices for ICWPT applications seem to be insulated gate bipolar transistors (IGBTs) with commercial products up to the power level of 3kV/2kA, and a

switching frequency up to 80 kHz. Power metal oxide silicon field effect transistors (MOS-FETs) can switch at a speed up to MHz levels, but their voltage levels are too low for high-power ICWPT applications.

- **Efficient operation.** Due to various copper and ferrite losses, achieving high system power efficiency is a challenging task.
- **Maximum temperature rise.** This is an important factor to keep the system operating in an acceptable range of temperature, especially when the system is used in a specified temperature environment.
- **System size/weight.** The size and weight are limiting factors in designing an ICWPT system. The conversion process in power electronics requires the use of magnetic components that are usually the heaviest and bulkiest items of the circuit. The design of such components has an important influence on the overall system size/weight, power conversion efficiency, and cost.
- **System stability and control.** It is always important to have a stable system under full range of load and magnetic coupling variations in practical applications. Variable frequency controlled ICWPT power supplies can become unstable if not designed properly [6].
- **Cost effectiveness.** Existing ICWPT systems are costlier than traditional wired counterparts due to the complicated power electronic circuitry and magnetic coupling design. It is a challenging task to improve the system design to bring the cost down for practical applications.
- **Compliance.** Final practical products of ICWPT systems need to pass electromagnetic compatibility (EMC) and safety standards, which can be a challenging engineering design task.

The above mentioned challenges may interact with each other, making the system optimisation very difficult. Trade-offs often need to be made depending on practical constraints and requirements.

3. Operating principle and general diagram of ICWPT systems

3.1. Operating principle

The fundamental theory of ICWPT systems is governed by Faraday and Ampere's laws as shown in **Figure 1**. Based on Ampere's law, current I generates a magnetic field H . Some of this magnetic field links the secondary power pickup coil and according to Faraday's law causes a voltage V to be induced.

Ampere's law can be mathematically expressed as:

$$\oint \vec{H} \cdot d\vec{l} = I \quad (1)$$

This equation states that the line integral of the magnetic field intensity around a closed loop is equal to the current flowing through it.

Faraday's law, on the other hand, is expressed by:

$$V = -N_2 \frac{d\phi}{dt} \quad (2)$$

where N_2 is the number of turns of the secondary coil.

The negative sign in (6) is described by Lenz's law, which states that the current flow in the secondary coil (when a load is connected) will be such that it creates a magnetic field that opposes the primary magnetic field.

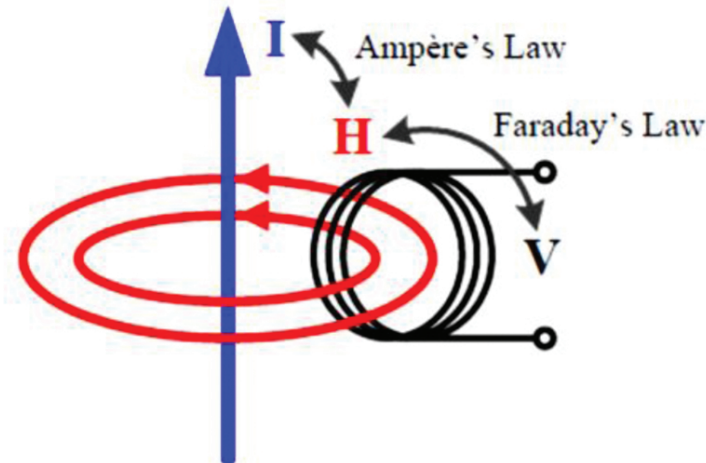


Figure 1. Fundamental theory of an ICWPT system.

3.2. General block diagram of an ICWPT system

A typical ICWPT system is normally constructed by winding the primary and secondary coils into separate halves of ferrite cores parted by an air gap as shown in **Figure 2**. Since direct physical contacts are eliminated in such a system, magnetic link is used to provide a reliable and efficient power transfer across an air gap. As it can be seen, the magnetic flux ϕ_m couples from one half of the core to the other half and provides a mutual inductance M that couples energy from the primary to the secondary side. The mutual inductance M is a function of geometry and can be found by simulation, measurement, or modelling the physical structure [7, 8].

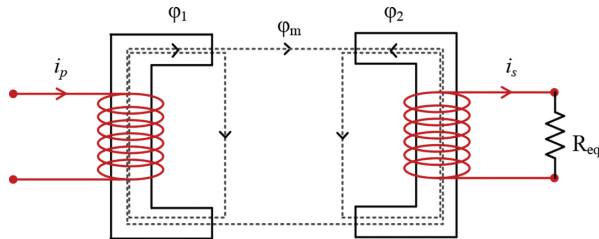


Figure 2. Typical flux linkage in an ICWPT system.

In such a loosely coupled power transfer system, the leakage fluxes can be very large and cannot be ignored. The proportion of the primary coils flux that links with the secondary coil is known as the primary coupling coefficient expressed by:

$$k_1 = \frac{\phi_M}{\phi_1} \quad (3)$$

Likewise, the secondary coupling coefficient is given by:

$$k_2 = \frac{\phi_M}{\phi_2} \quad (4)$$

These two values are typically combined to give the overall system coupling coefficient as:

$$k = \sqrt{k_1 k_2} \quad (5)$$

The mutual inductance between the primary and the secondary coils then is given by:

$$M = k \sqrt{L_p L_s} \quad (6)$$

where L_p and L_s are the self-inductances of the primary and the secondary coils.

An ICWPT system can then be considered as a loosely coupled power transfer system using modern power conversion, control, and magnetic coupling techniques to achieve wireless power transfer as shown in **Figure 3**. It consists of a primary side AC/DC/AC resonant converter which converts the rectified AC power into high frequency AC power. The high-frequency AC power then is fed to the primary coil which is magnetically coupled to the secondary coil, while physically separated. The secondary side then can be movable (linearly or/and rotating), giving flexibility, mobility, and safeness for supplied loads. In the secondary side, the induced high-frequency power is converted and controlled by a secondary converter

to meet the requirements specified by the load parameters. In fact, the time-varying magnetic field generated by the primary coil induces an electromotive force in the secondary coil which forms the voltage source of the secondary power supply. Since the magnetic coupling of an ICWPT system is normally very loose compared to normal transformers, the induced voltage source is usually unsuitable to be used to drive the load directly. Thus, a power conditioner with proper circuit tuning and conversion is required to control the output power according to the load requirements [9].

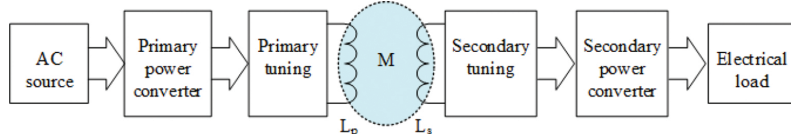


Figure 3. Fundamental elements of an ICWPT system.

4. System tuning

Tuning the primary and the secondary inductances of an ICWPT system is important for several reasons: (1) Compensating the primary inductance makes the power supply able to drive the given limited voltage ratings of the employed switches, (2) Constructing a resonant tank for resonant converters which is required to enable soft-switching operation of the switches to reduce switching losses and EMI, (3) Prevent the harmonic propagation in the circuit due to its filtering function, and (4) Compensating the secondary inductance improves the power transfer capability of the system.

4.1. Primary side tuning

Compensating the primary inductance improves the power factor and reduces the required Volt-Ampere rating of the primary power source. The compensation topologies are considered, namely series compensation, parallel compensation, and series-parallel compensation as shown in **Figure 4**. In series compensation, the voltage across the capacitance compensates the voltage drop of the primary equivalent reactance, making the required supply voltage to reduce. In parallel compensation, the current flowing through the capacitance compensates the current in the primary coil. Hence the required supply current is reduced. Series-parallel compensation realises the reduction of both in voltage and in current. In **Figure 4** in a series compensation topology, the output current from the inverter bridge (I_i) is equal to the primary current which is passing through the primary inductance (I_p). This signifies that the primary current in series compensation circulates through the inverter bridge which, in turn, causes significant power dissipation in the switching network. Moreover, in series compensation, the voltage is boosted because of the added voltage across the tuning capacitor. This results in an increased voltage across the primary coil (V_p) that is higher than the inverter output voltage (V_i). This is beneficial as it allows the power supply to drive a high primary inductance with

a desired primary current. The parallel compensation, on the other hand, has a current increase property. The primary current (I_p) is greater than the power converter output current (I_i). This is because the reactive current is circulating inside the resonant tank, and only the real current is flowing through the inverter bridge. As a result, in a parallel tuned power supply design, lower current rated switches may be used. The value of the primary compensation capacitor is often designed to fully compensate the primary inductance at the primary operating angular frequency (ω). In this case, the primary compensation capacitance is determined by:

$$C_p = \frac{1}{\omega^2 L_p} \quad (7)$$

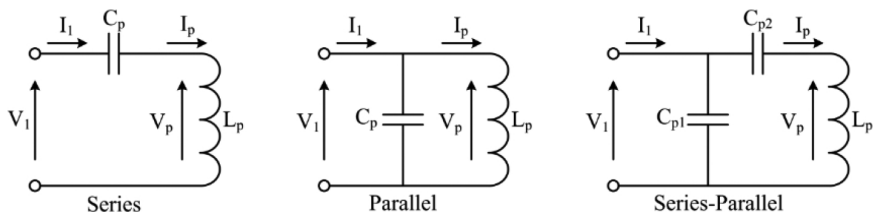


Figure 4. Primary tuning topologies.

Note that the capacitance of (7) is calculated for either a series- or a parallel-tuning topology. In the case of a composite topology, it is a combination of the two topologies. One simple way is to use C_{p2} to fully cancel the primary leakage inductance ($L_p - M$), and C_{p1} to fully tune the remaining portion of the primary self-inductance (M):

$$C_{p1} = \frac{1}{\omega^2 M} \quad (8)$$

$$C_{p2} = \frac{1}{\omega^2 (L_p - M)} \quad (9)$$

4.2. Secondary side tuning

In an ICWPT system, because of the large internal reactance, the power transferred from the primary to the secondary side is not sufficient for the load. For an uncompensated secondary inductance, the maximum output power occurs when the load resistance R_L is equal to the internal reactance ωL_s , and can be expressed by [9]:

$$P_{o,max} = \frac{1}{2} V_{oc} I_{sc} \quad (10)$$

where V_{oc} is the open-circuit voltage at the secondary terminals and I_{sc} is the short-circuit current of the secondary side.

In order to improve the power transfer capability of the system, normally the secondary side is tuned to the primary side operating frequency. There are two basic tuning topologies used in the secondary side, namely series compensation and parallel compensation as shown in **Figure 5**. An equivalent resistance (R_{eq}) represents the equivalent load on the secondary side.

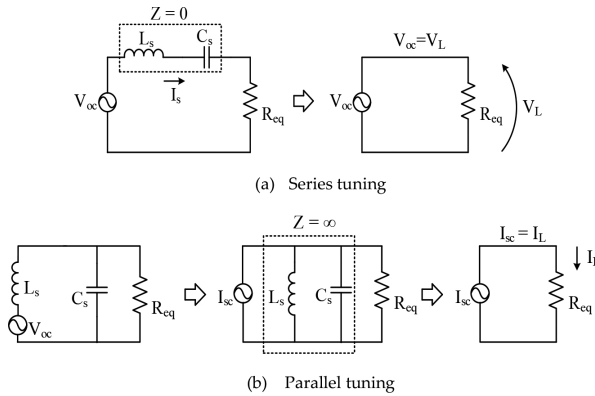


Figure 5. Secondary side-tuning topologies. (a) Series tuning. (b) Parallel tuning.

In **Figure 5(a)**; the equivalent reactance and its compensation capacitance cancel each other at the resonant frequency, making the output voltage independent of the load and equal to the secondary open-circuit voltage. Likewise, in parallel compensation the equivalent admittance and its compensating capacitance cancel each other at the resonant frequency, which makes the output current independent of the load and equal to the secondary short circuit current as illustrated in **Figure 5(b)**. For maximum power transfer, the secondary resonant frequency is normally designed to equal the nominal frequency. In this case, the secondary compensation capacitance is determined as:

$$C_s = \frac{1}{\omega^2 L_s} \quad (11)$$

5. Equivalent circuit and power transfer capability

5.1. T-equivalent circuit

Typical ICWPT systems are modelled using the conventional transformer model with an equivalent T-circuit as shown in **Figure 6**. It should be noted that normally the air gap in the path of the flux leads to low flux densities which tend to make the core losses very small, so

the core losses component may be neglected from the model without significant loss of accuracy.

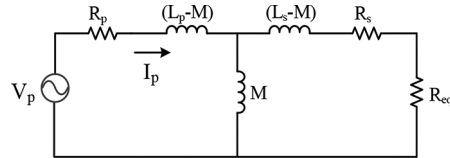


Figure 6. T-equivalent circuit.

From the above model, the power transfer capability of an ICWPT system is determined by two fundamental parameters: V_{oc} being the open-circuit voltage (when $R_{eq} = \infty$), and I_{sc} being the short-circuit current (when $R_{eq} = 0$) obtained from two basic open-circuit and short-circuit tests as [10]:

$$V_{oc} = j\omega M I_p \quad (12)$$

$$I_{sc} = I_p \cdot \frac{j\omega M}{R_s + j\omega[M + (L_s - M)]} \quad (13)$$

In practice, in order to reduce the coils losses, a woven Litz wire is normally used with low ESR (Equivalent Series Resistance); therefore, in (13) R_s can be neglected giving the short-circuit current as [10]:

$$I_{sc} = I_p \cdot \frac{M}{L_s} \quad (14)$$

From the above equations, the uncompensated power S_u of the secondary side can be expressed as follows [10]:

$$S_u = V_{oc} I_{sc} = \omega \frac{M^2}{L_s} I_p^2 \quad (15)$$

In practice, the maximum power transferred to the load side without compensation is $S_u/2$. The power presented by (15) can be boosted up Q_s times, using resonant techniques. As detailed in the previous section, a capacitance can be added to the circuit in series or parallel to tune the secondary inductance to the primary operating switching frequency. The maximum power transferred to the load side for a certain Q_s then can be given as follows:

$$P_2 = Q_s S_u = Q_s \cdot \omega \cdot \frac{M^2}{L_s} I_p^2 \quad (16)$$

where Q_s is the secondary circuit quality factor and it is different depending on the secondary tuning topology as given by:

$$Q_s = \begin{cases} \text{Series - tuned secondary : } \frac{\omega L_s}{R_{eq}} \\ \text{Parallel - tuned secondary : } \frac{R_{eq}}{\omega L_s} \end{cases} \quad (17)$$

It should be noted that for the parallel-tuned secondary, the secondary coil appears as a current source, while for a series-tuned secondary it acts as a voltage source. The tuned output of the secondary coil is then rectified and regulated to a constant output voltage using an appropriate switch-mode controller according to the load requirements. However, based on the tuning topology, different power regulation circuitry such as boost, buck, etc. is used on the secondary side [11]. The quality factor Q_s is determined by the secondary circuit parameters as well as the equivalent output load, which is related to the operation of the switch-mode controller. It is an important parameter which needs to be chosen carefully during design. Although higher Q_s increases the power transfer capability, for several reasons in practice, the highest Q_s reachable is limited to about 10. Firstly, the secondary operational bandwidth is inversely proportional to Q_s . Secondly, higher Q_s would be obtained at the expenses of the higher secondary VA rating so that practical size and thermal ratings also naturally limit Q_s in commercial systems. Thirdly, practical component tolerances and aging affect the sensitivity of the circuit and make power transfer at high Q_s impractical.

5.2. Mutual inductance model

The mutual inductance model uses the concepts of induced and reflected voltages to describe the coupling effect between the secondary and the primary networks. Both the induced and the reflected voltages are expressed in terms of the mutual inductance as shown in **Figure 7**. Note that coils losses are assumed to be very small and not considered in the presented model. In a mutual inductance model, the leakage inductance is not modelled separately from the mutual portion for circuit analysis as in other models such as T-equivalent circuit. This is a major advantage for ICWPT systems where the leakage inductance is too large to be ignored.

In the mutual inductance model, the reflected voltage is used to represent the total effect of the secondary on the primary side. However, the effect of the secondary must be considered together with the inherent properties of the primary coil in the analysis of the primary network. The reflected voltage is determined by the current flowing within the secondary coil and the mutual inductance between the primary and the secondary as given by:

$$V_r = -j\omega M I_s \quad (18)$$

The effect of the secondary can be represented by the equivalent reflected impedance by dividing the reflected voltage by the primary current as follows:

$$Z_r = \frac{V_r}{I_p} = \frac{-j\omega M I_s}{I_p} \quad (19)$$

The secondary current flowing through the secondary coil (I_s), on the other hand, is defined by the input impedance seen by the open circuit voltage as:

$$I_s = \frac{V_{oc}}{Z_s} = \frac{j\omega M I_p}{Z_s} \quad (20)$$

Combining (19) and (20), the equivalent reflected impedance of the secondary back on to the primary is expressed as:

$$Z_r = \frac{\omega^2 M^2}{Z_s} \quad (21)$$

The overall impedance of the secondary side for both series and parallel compensated secondary side can be expressed as:

$$Z_s(\text{series}) = j\omega L_s + \frac{1}{j\omega C_s} + R_{eq} \quad (22)$$

$$Z_s(\text{parallel}) = j\omega L_s + \frac{1}{j\omega C_s + \frac{1}{R_{eq}}} \quad (23)$$

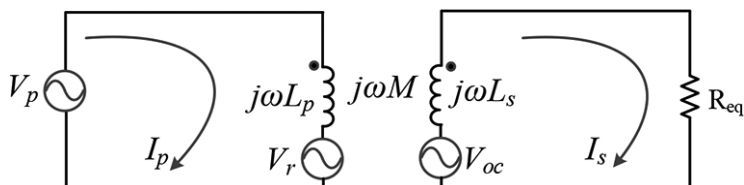


Figure 7. Frequency domain mutual inductance model.

Since the secondary network depends on the selected tuning topology, the reflected resistance and reactance at the resonant frequency onto the primary side are different as given in **Table 1**.

Tuning topology	Reflected resistance	Reflected reactance
Series	$\frac{\omega^2 M^2}{R_{eq}}$	0
Parallel	$\frac{M^2 R_{eq}}{L_s^2}$	$-\frac{\omega M^2}{L_s}$

Table 1. Reflected impedance for different secondary tuning.

It can be seen from **Table 1** that the reflected impedance for the series-tuned secondary coil is purely resistive, while the parallel-tuned secondary coil reflects both resistive and capacitive components. This is one of the major differences between the series and the parallel compensated secondary inductance. The reflected impedance can then be compared and combined with the impedance of the primary coil. The power transferred from the primary to the secondary is simply the reflected resistance (real part of the reflected impedance) multiplied by the squared primary current as given by:

$$P_2(\text{series tuning}) = \left[\frac{\omega^2 M^2}{R_{eq}} \right] I_p^2 \quad (24)$$

$$P_2(\text{parallel tuning}) = \left[\frac{M^2 R_{eq}}{L_s^2} \right] I_p^2 \quad (25)$$

6. Power losses associated with the magnetic structure of ICWPT systems

Two types of power losses are associated with the magnetic coupling structure of an ICWPT system: (1) core losses and (2) coils losses (conduction losses) as detailed below:

6.1. Core losses

Typically, core losses are divided into two groups: hysteresis and eddy current losses. Hysteresis loss increases with higher frequencies as more cycles are undergone per unit time and is associated with the applied voltage and its frequency. While, eddy currents loss is proportional to the square of the applied voltage and it is independent of frequency. In the case of core losses due to magnetic hysteresis, all ferromagnetic materials tend to retain some degree of magnetisation after disclosure to an external magnetic field. This tendency to stay magnetised is called *hysteresis*. And it takes a certain amount of energy to overcome this

opposition to change every time when the magnetic field produced by the primary coil changes polarity (twice per AC cycle). This type of loss can be mitigated by choosing a core with low hysteresis (with a ‘thin’ B-H curve), and designing the core for minimum flux density (large cross-sectional area). The hysteresis losses per unit volume are approximated by the following relationship [12]:

$$P_h = k f_{sw}^a \left(\frac{\Delta B}{2} \right)^d \quad (W / m^3) \quad (26)$$

where k , a , and d are the material-related constants, f_{sw} is the switching frequency, and ΔB is the flux excursion.

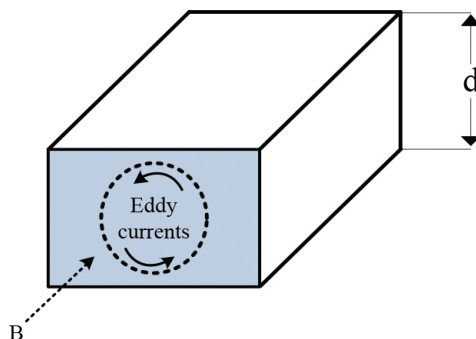


Figure 8. Eddy currents created in a magnetic material.

The second part of the core losses is due to magnetic effects of the core material. This type is resistive power dissipation due to the induced eddy currents in the core material. Usually, when a low resistivity material is placed in a variable magnetic field, electric currents are induced in the material similar to the currents induced in the secondary coil. These induced currents tend to circulate through the cross-section of the core perpendicular to the main flux path. Their circular motion gives them their unusual name: like eddies in a stream of water that circulates rather than move in straight lines. These ‘eddy currents’ must overcome an electrical resistance as they circulate in the core. To overcome the resistance offered by the core, they dissipate power in the form of heat. Hence, there will be a source of power loss in the core that is difficult to eliminate and largely depends on the conductivity of the material and the magnetic field density. Thus, eddy currents can be minimised by selecting magnetic core materials that have low electrical conductivity. Ferromagnetic materials such as ferrites have a considerably low electrical conductivity, making them more suitable for high-frequency applications. The eddy current losses in a volume like that of **Figure 8** are approximated by the following relationship [12]:

$$P_e = \frac{B^2 f_{sw}^2 d^2}{\rho} \quad (W / m^3) \quad (27)$$

where ρ is the resistivity of the material and f_{sw} is the switching frequency.

6.2. Conduction losses

In practice, there will always be power dissipated in the form of heat through the resistance of current-carrying conductors. Increasing the gauge of the wire can minimise this loss, but only with extensive increases in cost, size, and weight. Generally, the conduction losses of the coils are classified into two groups: (1) the DC and (2) the AC losses. When a DC current flows through an inductor, normally DC losses are the result of current I flowing through the wire with resistance R , power ($I^2 R$) is dissipated and, accordingly, developing heat in the wire. When an inductor is used in an AC circuit, on the other hand, normally due to the varying magnetic field around the coils, the current distribution in the conductors is not uniform. The self-inductance of the conductor, as well as the magnetic field created by adjacent turns of the same coil, redistributes the current flow within the wire and reduces the effective cross-sectional area of the conductor and accordingly increases the AC resistance. These effects are known as skin and the proximity effects, and they become stronger at higher operating frequencies as detailed below.

6.2.1. The skin effect

When a wire is carrying a DC current, the current is distributed uniformly over all the effective area of the wire. This current distribution is non-uniform when the wire is carrying an alternating current, as the current intensity and the magnetic field in a conductor change and results in a phenomenon known as '*skin effect*'. The skin effect is the restriction of the flow of alternating current to the surface of a conductor. This restriction is caused by the alternating magnetic field that the current itself generates within the conductor. As depicted in **Figure 9(a)**, the current flowing in the conductor generates a magnetic field around it. This field in turn creates circulating currents in the wire. These currents are opposite to the main current flow in the centre of the conductor and add to the main current closer to the surface of the wire. The result is that more net current is flowing closer to the surface of the conductor, and eventually an increase in the effective resistance of the conductor due to the reduced cross-sectional area for current flow as shown in **Figure 9(b)**. This area of current flow between the outer surface and a level of the conductor diameter is called the '*skin depth*'. The skin depth is thus defined as the depth below the surface of the conductor at which the current density has fallen to $1/e$ (about 0.37) of J_s . Typically, it is well approximated as:

$$\delta = \sqrt{\frac{2\rho}{\omega\mu}} \quad (28)$$

where ρ is the resistivity of the conductor, ω is the angular frequency of the current, and $\mu = \mu_r \mu_0$ is the absolute magnetic permeability of the conductor.

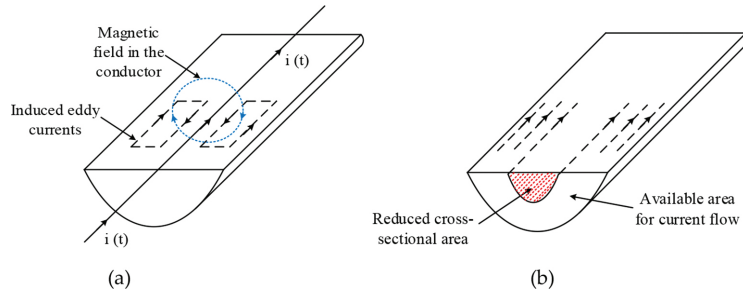


Figure 9. Impact of skin effect on the coil ESR: (a) generated eddy currents and (b) reduced cross-sectional area due to skin effect.

6.2.2. The proximity effect

Proximity effect is the tendency for current to flow in other undesirable patterns, loops, or concentrated distributions due to the presence of magnetic fields generated by nearby conductors as shown in **Figure 10(a)**. In fact, when another conductor is brought into proximity to one or more other nearby conductors, such as within a closely wound coil of wire, the distribution of current within the conductor will be constrained to smaller regions as shown in **Figure 10(b)** in blue. Field intensity is no longer uniform around each conductor surface. The resulting current crowding is termed as the '*proximity effect*' and increases with the frequency. This current crowding gives an increase in the effective resistance which results in higher power losses in the wire.

In transformers and inductors, proximity-effect losses typically dominate over skin-effect losses [13]. In Litz-wire windings, proximity effect may be further divided into internal proximity effect (the effect of other currents within the bundle) and external proximity effect (the effect of current in other bundles). The actual losses in one strand of a Litz bundle are

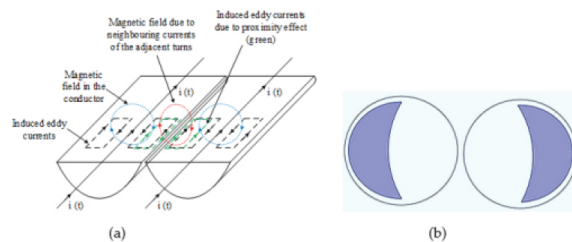


Figure 10. Two conductors in proximity: (a) magnetic fields generated by nearby conductors and (b) impact of proximity effect on the cross-sectional area of a conductor.

simply a result of the total external field, due to the currents in all the other strands present. One approach of calculating the loss in a Litz winding is to look at it as a single winding, made up of nN turns of the strand wire, each with current i/n flowing in it, where n is the number of strands, N is the number of turns of Litz wire, and i is current flowing in the overall Litz bundle. The loss in the Litz winding will be the same as in the equivalent single-strand winding as long as the currents flowing in all the strands are equal [13].

7. System magnetic coupling efficiency

7.1. Series-tuned secondary

Figure 11 shows a diagram of a magnetic coupling structure of two magnetically coupled coils. The inductances L_p and L_s represent the primary and the secondary coils, and R_{eq} represents the equivalent load resistance which includes the DC load resistance and any other resistive part of the circuit such as the rectifier, voltage regulator, etc.

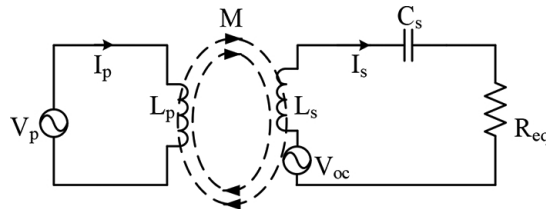


Figure 11. Simplified circuit with a series-tuned secondary.

The coupling efficiency of the circuit shown in **Figure 11** can be simply expressed by:

$$\begin{aligned} \eta_k &= \frac{\text{output power across } R_{eq}}{\text{output power across } R_{eq} + \text{power losses}} \\ &= \frac{P_{eq}}{P_{eq} + P_{loss1} + P_{loss2}} \end{aligned} \quad (29)$$

where P_{loss1} and P_{loss2} are the primary and secondary coils power losses respectively, and P_{eq} is the supplied active power to the load.

The power losses of the primary and secondary coils can be quantified based on their unloaded and loaded quality factors. The unloaded quality factors are basically the coils quality factors (Q_{Lp} & Q_{Ls}); and when a load is added, it is referred to as the loaded or circuit quality factor (Q_s & Q_p). The general definition of the quality factor is the ratio of stored energy in the circuit to the energy lost in the circuit as given by:

$$\begin{aligned} Q &= \frac{\text{Stored energy}}{\text{Dissipated energy}} = \frac{\text{Reactive power}}{\text{Active power}} \\ &= \frac{VAR}{WATT} = \frac{\omega L}{R} \end{aligned} \quad (30)$$

From the above definition, the primary and the secondary coils quality factors are:

$$Q_{Lp} = \frac{VAR_p}{P_{loss1}} = \frac{\omega L_p}{R_p} \quad (31)$$

$$Q_{Ls} = \frac{VAR_s}{P_{loss2}} = \frac{\omega L_s}{R_s} \quad (32)$$

From (31) and (32), the power losses of the primary and secondary coils can be written as:

$$P_{loss1} = \frac{VAR_p}{Q_{Lp}} \quad (33)$$

$$P_{loss2} = \frac{VAR_s}{Q_{Ls}} \quad (34)$$

Under load conditions, the secondary circuit quality factor is:

$$Q_s = \frac{VAR_s}{P_{loss2} + P_{eq}} \quad (35)$$

From (35), the secondary reactive power can then be expressed as:

$$VAR_s = (P_{loss2} + P_{eq})Q_s \quad (36)$$

Substituting (36) into (34):

$$P_{loss2} = \frac{P_{eq} \frac{Q_s}{Q_{Ls}}}{\left(1 - \frac{Q_s}{Q_{Ls}}\right)} = \frac{P_{eq} Q_s}{Q_{Ls} - Q_s} \quad (37)$$

The primary reactive power can also be expressed in terms of the secondary circuit quality factor as [14]:

$$VAR_p = \frac{P_{eq}}{k^2 Q_s} \quad (38)$$

Substituting (38) into (33), the primary coil power loss can be rewritten as:

$$P_{loss1} = \frac{P_{eq}}{k^2 Q_s Q_{Lp}} \quad (39)$$

Substituting (37) and (39) into (29) gives the *coupling efficiency for a series-tuned secondary* as:

$$\begin{aligned} \eta_k &= \frac{P_{eq}}{P_{eq} + \frac{P_{eq}}{k^2 Q_s Q_{Lp}} + \frac{P_{eq} Q_s}{Q_{Ls} - Q_s}} \\ &= \frac{1}{1 + \frac{1}{k^2 Q_s Q_{Lp}} + \frac{Q_s}{Q_{Ls} - Q_s}} \end{aligned} \quad (40)$$

If $Q_{Ls} \gg Q_s$, the term, $Q_{Ls} - Q_s \approx Q_{Ls}$. Hence:

$$\eta_k = \frac{1}{1 + \frac{1}{k^2 Q_s Q_{Lp}} + \frac{Q_s}{Q_{Ls}}} \quad (41)$$

7.2. Parallel-tuned secondary

A parallel-tuned secondary coil shown in **Figure 12** is in fact a Norton equivalent of the series-tuned secondary coil.

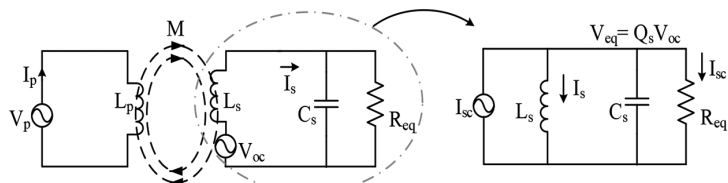


Figure 12. Simplified circuit with a parallel-tuned secondary.

Similar to the series-tuned secondary, the power losses within the primary and the secondary coils can be expressed in terms of the coils quality factors as:

$$P_{loss1} = \frac{VAR_p}{Q_{Lp}} \quad (42)$$

$$P_{loss2} = \frac{VAR_s}{Q_{Ls}} \quad (43)$$

The output power across R_{eq} is:

$$P_{eq} = I_{sc}^2 R_{eq} \quad (44)$$

In a parallel-tuned secondary, the resonant current through the coil is:

$$I_s = I_{sc} \sqrt{1 + Q_s^2} \quad (45)$$

The reactive power of the secondary coil then is:

$$\begin{aligned} VAR_s &= I_s^2 \omega L_s = \left[I_{sc} \sqrt{1 + Q_s^2} \right]^2 \omega L_s \\ &= I_{sc}^2 (1 + Q_s^2) \omega L_s \end{aligned} \quad (46)$$

Taking the ratio of (46) and (44):

$$\frac{VAR_s}{P_{eq}} = \frac{(1 + Q_s^2) \omega L_s}{R_{eq}} = \frac{(1 + Q_s^2)}{Q_s} \quad (47)$$

Substituting VARs from (47) into (43):

$$P_{loss2} = P_{eq} \frac{\frac{(1 + Q_s^2)}{Q_s}}{Q_{Ls}} = P_{eq} \frac{(1 + Q_s^2)}{Q_s Q_{Ls}} \quad (48)$$

Again the primary reactive power can also be expressed in terms of the secondary circuit quality factor as:

$$VAR_p = \frac{P_{eq}}{k^2 Q_s} \quad (49)$$

Substituting (49) into (42), the primary coil power loss can be rewritten as:

$$P_{loss1} = \frac{P_{eq}}{k^2 Q_s Q_{Lp}} \quad (50)$$

Substituting (48) and (50) into (29) gives the *coupling efficiency for a parallel-tuned secondary* as:

$$\eta_k = \frac{1}{1 + \frac{1}{k^2 Q_s Q_{Lp}} + \frac{(1+Q_s^2)}{Q_s Q_{Ls}}} \quad (51)$$

If $Q_s^2 \gg 1$, (51) becomes:

$$\eta_k = \frac{1}{1 + \frac{1}{k^2 Q_s Q_{Lp}} + \frac{Q_s}{Q_{Ls}}} \quad (52)$$

8. Summary

This chapter has presented the fundamentals of ICWPT systems. Their major application areas, operating principle, and present challenges associated with this technology have been discussed. This technology has the ability to deliver major advancements in industries and applications that are dependent on contacting connectors, which can be unreliable and prone to failure. The basis of a wireless power transfer system involves essentially two magnetically coupled coils separated by an air gap—a transmitter and a receiver coil. The transmitter coil is energised by alternating AC power to generate a magnetic field, which in turn induces a voltage in the receiver coil.

After a general overview of system compensation in this technology, a detailed modelling based on T-equivalent circuit as well as a mutual inductance model including system power transfer capability have been presented. Power losses associated with the magnetic coupling structure of such a system have been detailed. A comprehensive study with mathematical relationships has been conducted on the derivation of magnetic coupling efficiency of the system for both a series- and a parallel-tuned secondary side.

Author details

Ali Abdolkhani

Address all correspondence to: aabd104@aucklanduni.ac.nz

Power by Proxi Ltd, Auckland, New Zealand

References

- [1] C. Fernandez, O. Garcia, R. Prieto, J. Cobos, and J. Uceda, "Overview of different alternatives for the contact-less transmission of energy," IECON (Industrial Electronics Society, IEEE 2002 28th Annual Conference), 2002, vol. 2, pp. 1318–1323.
- [2] J. Boys, G. Covic, and A. W. Green, "Stability and control of inductively coupled power 16 transfer systems," IEE Proceedings – Electric Power Applications, 2000, vol. 147, pp. 37–43.
- [3] M. S. Rauls, D. W. Novotny, and D. M. Divan, "Design considerations for high-frequency coaxial winding power transformers," *IEEE Transactions on Industry Applications*, 2002, vol. 29, pp. 375–381.
- [4] R. W. Erickson and D. Maksimovi, *Fundamentals of Power Electronics*, Springer, The Netherlands, 2001.
- [5] M. H. Rashid, *Power Electronics Handbook*, Academic Press, 2001 .
- [6] T. Chunsen, D. Xin, W. Zhihui, S. Yue, and A. P. Hu, "Frequency bifurcation phenomenon study of a soft switched push-pull contactless power transfer system," *6th IEEE Conference on Industrial Electronics and Applications*, 2011, pp. 1981–1986.
- [7] A. Abdolkhani, A. P. Hu, and N. C. K. Nair, "Modelling and parameters identification of through-hole type wind turbine contactless sliprings," *SCIRP/Engineering*, 2012, vol. 4, pp. 272–283.
- [8] K. D. Papastergiou and D. E. Macpherson, "Contact-less transfer of energy by means of a rotating transformer," *Proceedings of the IEEE International Symposium on Industrial Electronics, 2005. ISIE 2005*, 2005, pp. 1735–1740.
- [9] A. P. Hu, "Selected resonant converters for IPT power supplies," PhD Thesis, University of Auckland, 2001.
- [10] S. Raabe, G. A. J. Elliott, G. A. Covic, and J. T. Boys, "A quadrature pickup for inductive power transfer systems," *2nd IEEE Conference on Industrial Electronics and Applications, 2007. ICIEA 2007*, 2007, pp. 68–73.

- [11] H. H. Wu, J. T. Boys, and G. A. Covic, "An AC processing pickup for IPT systems," *IEEE Transactions on Power Electronics*, 2010, vol. 25, pp. 1275–1284.
- [12] N. Mohan, T. M. Undeland, and W. Robbins, "*Power Electronics: Converters, Applications and Design*", 1995, John Wiley and Sons, New York, 1997.
- [13] C. R. Sullivan, "Optimal choice for number of strands in a litz-wire transformer winding," *IEEE Transactions on Power Electronics*, 1999, vol. 14, pp. 283–291.
- [14] G. A. Covic and J. T. Boys, "Inductive power transfer," *Proceedings of the IEEE*, 2013, vol. 101, pp. 1276–1289.

Analysis of Wireless Power System Efficiency in Dependency on Configuration of Resonant Tank

Michal Frivaldsky, Pavol Spanik, Peter Drgona,
Viliam Jaros and Marek Piri

Additional information is available at the end of the chapter

<http://dx.doi.org/10.5772/62998>

Abstract

This chapter compares various compensation methods for resonant coupling of the wireless energy transfer system. A proposed analysis is particularly relevant to any application where contactless battery charging is used. Main parameters that are investigated include efficiency and electrical variables (current and voltage) of the circuit. In order to analyze the most suitable solution of coupling compensation, the relevant equations are graphically interpreted for each discussed circuit topology. Finally, this chapter provides the recommendations how to design the wireless power-transfer system with the highest possible efficiency for the given system parameters (switching frequency and transmitting distance).

Keywords: Efficiency, wireless power transfer, configuration, resonant compensation, distance

1. Introduction

Nowadays, electrically powered automobiles show higher interest in the automotive industry. Electric vehicles gain this interest thanks to high efficiency. In the case of the asynchronous motor, the electrical energy can be converted into the mechanical with an efficiency of 90%, which is much more than the efficiency of the combustion engine that has an efficiency of only 25–34%. Due to the limitation of natural resources such as petroleum and natural gas, the power electronics and energy conversion along with the development of new battery types contribute to the development and application in the automotive industry. The main disadvantage of the electric car is the energy accumulation. Batteries are large, heavy, with short lifetime, and

long charging times. These reasons show how necessary it is to solve an issue of battery charging [1]. In general, charging systems can be classified as wired and these could be replaced with wireless (inductive) systems.

Wireless power transfer and issues relevant to wireless charging of various types of electronic devices are still important and emerging trends in electrical engineering [2–4]. Regarding of wireless power transfer, each application requires several self-specific operational properties or transfer characteristics. The most important of them are transmitting efficiency, value of the output power, mutual position between the transmitter and the receiver, and their geometric dimensions. One possible way how to influence these parameters lies in the main circuit configuration of a compensation network of the wireless energy transfer (WET) system. Inductively coupled power-transfer systems have been suited for a wide spectrum of consumer applications including electromobility (battery charging of vehicles). Even high system efficiency has been achieved (approximately 70%); however, the restriction to close range, typically shorter than 30% of the coil diameter, is the main limitation for perspective usage in high-efficiency or high-performance systems [5, 6].

It the beginning of 2000s, a team of researchers under charge of Prof. Soljacic introduced a new concept of strongly coupled magnetic resonance for wireless energy transfer systems [7]. In comparison with an inductively coupled system, the coils with resonant inductive coupling have several significant advantages. The most important of them are as follows: the coupling may be very efficient even at large transmission distances, it has low environmental impact, and can be variously tuned/configured based on the requirements of target application. The solution of the WET system based on the magnetic-resonance coupling represents constantly investigated phenomena. Most of the analyses are based on the pure theory of physical interactions, which are unable to provide clear and consistent overview of knowledge for researchers in the field of electrical engineering [8, 9]. Based on this, it can be said that some important relationships between system efficiency, amount of transmitted power, and transmitting distance for magnetic-resonance coupled WET systems need to be introduced.

This chapter describes a simple equivalent circuit model for magnetic-coupled and resonant magnetic-coupled WET systems. The resonant coupling is further described in details, whereby all key system equations for various configurations of a resonant compensation network with pure resistive load are derived. From the component design point of view, it is also important to have knowledge about values of voltage and current in the main circuit. In the last part of the chapter, the general recommendations for practical use of each variant are provided.

2. Nonresonant magnetic coupling of the WET system

In the case of nonresonant magnetic coupling, the system acts as an air-cored transformer with relatively low mutual inductance. Due to high supplying frequency, the primary and the secondary leakage reactance cause a significant voltage drop, which limits amount of power

delivered to the load. Equivalent circuit composed for this type of coupling is shown in **Figure 1**.

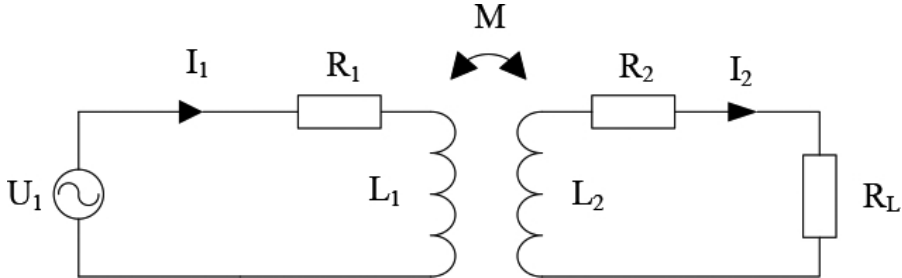


Figure 1. Equivalent circuit of the inductively coupled nonresonant WET system.

The circuit can be completely described by the system of loop currents calculated by Eq. (1):

$$\begin{bmatrix} \dot{U}_1 \\ 0 \end{bmatrix} = \begin{bmatrix} R_1 + j\omega L_1 & -j\omega M \\ -j\omega M & R_2 + R_L + j\omega L_2 \end{bmatrix} \begin{bmatrix} \dot{I}_1 \\ \dot{I}_2 \end{bmatrix} \quad (1)$$

The parameters R_1 and R_2 represent parasitic resistances of transmitting and receiving coils with self-inductances L_1 and L_2 , M forms the mutual inductance between respective coils, and R_L is the load (purely resistive). With regard to the high operational frequencies, the switched power source with square-wave voltage should be used to supply the system. In this case, Eq. (1) needs to be rewritten in Eq. (1) to consider selected frequency spectrum.

$$\begin{bmatrix} \frac{4}{\pi} \sum_{k=1,3,5,\dots}^{\infty} \frac{\dot{U}_1}{k} \\ 0 \end{bmatrix} = \begin{bmatrix} \sum_{k=1,3,5,\dots}^{\infty} R_1 + jk\omega L_1 & \sum_{k=1,3,5,\dots}^{\infty} -jk\omega M \\ \sum_{k=1,3,5,\dots}^{\infty} -jk\omega M & \sum_{k=1,3,5,\dots}^{\infty} R_2 + R_L + jk\omega L_2 \end{bmatrix} \begin{bmatrix} \dot{I}_1 \\ \dot{I}_2 \end{bmatrix} \quad (2)$$

On the other hand, the uncompensated leakage reactance forms in the circuit with a very high impedance even for a lower frequency component. This impedance causes a significant voltage drop and therefore the contribution of this harmonic component is very low. The system can be therefore analyzed only for the fundamental wave while keeping relatively good accuracy. The winding currents derived for the fundamental wave are provided in Eqs. (3) and (4):

$$\dot{I}_1 = \frac{R_2 + R_L + j\omega L_2}{(R_1 + j\omega L_1)(R_2 + R_L + j\omega L_2) + (\omega M)^2} \dot{U}_1 \quad (3)$$

$$\dot{I}_2 = \frac{-j\omega M}{(R_1 + j\omega L_1).(R_2 + R_L + j\omega L_2) + (\omega M)^2} \dot{U}_1 \quad (4)$$

The input power can be counted from the complex power on the primary side (5):

$$P_{IN} = \Re \left\{ \dot{U}_1 \dot{I}_1^* \right\} \quad (5)$$

The secondary side average power is then found using the loading resistance and the current flowing through it (Eq. (6)):

$$P_{OUT} = R_L \cdot |\dot{I}_2|^2 = R_L \cdot \left| \frac{-j\omega M}{(R_1 + j\omega L_1).(R_2 + R_L + j\omega L_2) + (\omega M)^2} \dot{U}_1 \right|^2 \quad (6)$$

The transmitting efficiency (7) is further given by the ratio of the output power (6) and the input power (5):

$$\eta = \frac{P_{OUT}}{|\dot{S}_{IN}| \cdot \cos(\phi)} = \left| \frac{R_L \omega^2 M^2}{[(R_1 + j\omega L_1).(R_2 + R_L + j\omega L_2) + (\omega M)^2] \cdot (R_2 + R_L + j\omega L_2) \cdot \cos(\phi)} \right| \quad (7)$$

where

$$\cos(\phi) = \frac{\Re(\dot{S}_{IN})}{|\dot{S}_{IN}|} = \frac{\Re \left(\frac{R_2 + R_L + j\omega L_2}{(R_1 + j\omega L_1).(R_2 + R_L + j\omega L_2) + (\omega M)^2} \dot{U}_1^2 \right)}{\left| \frac{R_2 + R_L + j\omega L_2}{(R_1 + j\omega L_1).(R_2 + R_L + j\omega L_2) + (\omega M)^2} \dot{U}_1^2 \right|} \quad (8)$$

The simulation parameters are taken from two constructed experimental prototypes of coupling coils, which are also identical. Their values are therefore the same on the primary as well as on the secondary side. The self-inductance equals $L_1 = L_2 = 127.4 \mu\text{H}$, parasitic resistance $R_1 = R_2 = 0.447 \Omega$, and the load $R_L = 8 \Omega$. The analyzed frequency range ($f_{\text{range}} = 290\text{--}340 \text{ kHz}$) is set according to the resonant frequency obtained from the resonant magnetic coupling discussed in the following chapter. The used compensation capacitors also have the same capacities $C_1 = C_2 = 2 \text{ nF}$. In the simulation, the minimal mutual inductance $M_{\min} = 1 \mu\text{H}$ corresponds to the transmitting distance of 50 cm, whereas its maximal value $M_{\max} = 11 \mu\text{H}$ represents the distance of 25 cm. This transmitting range is selected based on the application area, i.e., +battery charging of electric vehicles.

The results from simulation of the inductively coupled WET system plotted against frequency and mutual inductance are shown in **Figures 2–4**. The waveforms of the input and output powers are shown in **Figure 2**, the source and load current are shown in **Figure 3**, and the efficiency calculated using Eq. (7) together with a secondary induced voltage U_{L2} are shown in **Figure 4**.

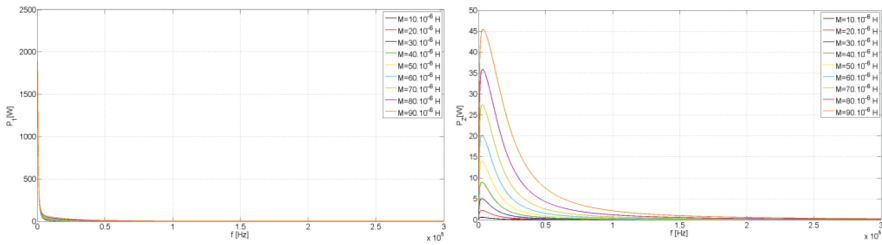


Figure 2. Input power (left) and output power (right) dependency on nonresonant coupling.

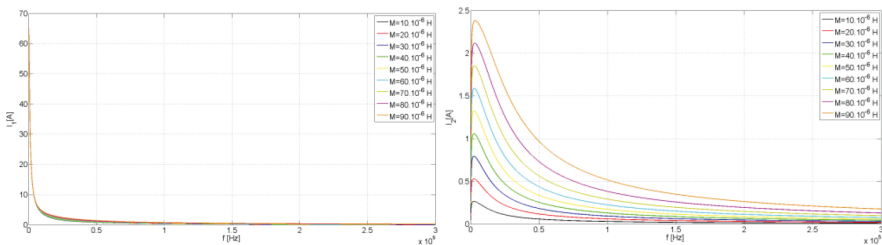


Figure 3. Source current (left) and load current (right) dependency on nonresonant coupling.

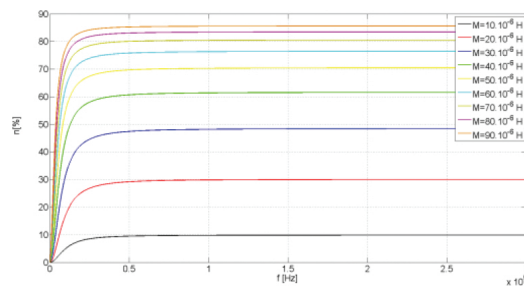


Figure 4. Efficiency dependency on nonresonant coupling.

As it can be seen from **Figure 4** (right), the transmitting efficiency mainly varies with given mutual inductance. The system is practically independent of frequency change even for the whole considered frequency range.

3. Series-series resonant coupling of the WET system

For series-series compensation, the capacitor is connected in series with transmitting and receiving coils (**Figure 5**).

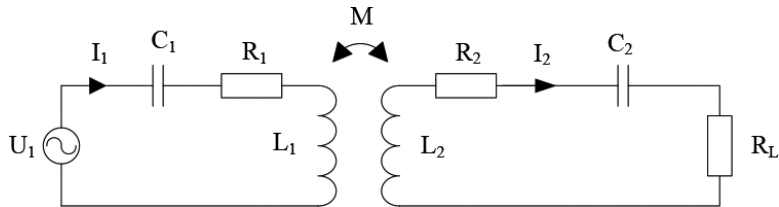


Figure 5. Equivalent circuit of the series-series compensated WET system.

Mathematical model of series-series compensation is, from the point of view of complexity, much easier than other compensation types. Using the methodology of loop currents, the impedance matrix of this configuration can be expressed as follows (11):

$$\left[R_1 + j \left(\omega L_1 - \frac{1}{\omega C_1} \right) \right] \dot{I}_{1_ss} - j \omega M \dot{I}_{2_ss} = \dot{U}_{1_ss} \quad (9)$$

$$-j \omega M \dot{I}_{1_ss} + \left[R_2 + R_L + j \left(\omega L_2 - \frac{1}{\omega C_2} \right) \right] \dot{I}_{2_ss} = 0 \quad (10)$$

$$\begin{bmatrix} \dot{U}_{1_ss} \\ 0 \end{bmatrix} = \begin{bmatrix} R_1 + j \left(\omega L_1 - \frac{1}{\omega C_1} \right) & -j \omega M \\ -j \omega M & R_2 + R_L + j \left(\omega L_2 - \frac{1}{\omega C_2} \right) \end{bmatrix} \begin{bmatrix} \dot{I}_{1_ss} \\ \dot{I}_{2_ss} \end{bmatrix} \quad (11)$$

From (11), the formula for the current of the transmitting and receiving parts in the complex form as (12) and (13) can be derived:

$$\dot{I}_1 = \dot{I}_{1_ss} = \frac{R_2 + R_L + j \left(\omega L_2 - \frac{1}{\omega C_2} \right)}{\left[R_1 + j \left(\omega L_1 - \frac{1}{\omega C_1} \right) \right] \cdot \left[R_2 + R_L + j \left(\omega L_2 - \frac{1}{\omega C_2} \right) \right] + (\omega M)^2} \dot{U}_{1_ss} \quad (12)$$

$$\dot{I}_2 = \dot{I}_{2_ss} = \frac{-j\omega M}{\left[R_1 + j\left(\omega L_1 - \frac{1}{\omega C_1}\right) \right] \cdot \left[R_2 + R_L + j\left(\omega L_2 - \frac{1}{\omega C_2}\right) \right] + (\omega M)^2} \dot{U}_{1_ss} \quad (13)$$

If the circuit is supplied by harmonic voltage with a frequency equal to the resonant frequency, then the value of the capacitive and inductive parts of the complex impedance will be the same and can be subtracted. Then, for the previous formulas (14) and (15), the following conditions are valid:

$$\dot{I}_1 = \dot{I}_{1_ss} = \frac{R_2 + R_L}{R_1 R_2 + R_1 R_L + (\omega M)^2} \dot{U}_{1_ss} \quad (14)$$

$$\dot{I}_2 = \dot{I}_{2_ss} = \frac{-j\omega M}{R_1 R_2 + R_1 R_L + (\omega M)^2} \dot{U}_{1_ss} \quad (15)$$

Equations (14) and (15) show that the circuit during resonance has only resistive characteristics, and circuit currents are given just by the parasitic resistances of coils, load resistance, and supply voltage. The input and output powers of the circuit with –series–series compensation can be expressed as Eqs. (16) and (17). The graphical interpretation of Eq. (17), as plotted in **Figure 6**, shows that the operation of the system with this kind of compensation should be excluded from resonant point. In other case, for low values of M (high distance of coils), the input power, as well as the output power (output current), rises too sharply, which might destroy the whole system.

$$\dot{S}_{IN_ss} = \dot{I}_1 \dot{U}_{1_ss} = \frac{R_2 + R_L + j\omega L_2}{\left[R_1 + j\left(\omega L_1 - \frac{1}{\omega C_1}\right) \right] \cdot \left[R_2 + R_L + j\left(\omega L_2 - \frac{1}{\omega C_2}\right) \right] + (\omega M)^2} \dot{U}_{1_ss}^2 \quad (16)$$

$$P_{OUT_ss} = R_L \cdot |\dot{I}_2|^2 = R_L \cdot \left| \frac{-j\omega M}{\left[R_1 + j\left(\omega L_1 - \frac{1}{\omega C_1}\right) \right] \cdot \left[R_2 + R_L + j\left(\omega L_2 - \frac{1}{\omega C_2}\right) \right] + (\omega M)^2} \dot{U}_{1_ss} \right|^2 \quad (17)$$

Dependence of efficiency for the series–series compensated circuit in the frequency domain can be expressed using Eq. (18):

$$\eta = \frac{\dot{P}_{OUT_SS}}{\dot{S}_{IN_SS} \cdot \cos(\varphi)} = \frac{R_L \omega^2 M^2}{\left[R_1 + j \left(\omega L_1 - \frac{1}{\omega C_1} \right) \right] \cdot \left[R_2 + R_L + j \left(\omega L_2 - \frac{1}{\omega C_2} \right) \right] + (\omega M)^2} \cdot (R_2 + R_L + j \omega L_2) \cdot \cos(\varphi) \quad (18)$$

where

$$\cos(\varphi) = \frac{\Re(\dot{S}_{IN})}{|\dot{S}_{IN}|} = \frac{\Re \left(\frac{R_2 + R_L + j \omega L_2}{\left[R_1 + j \left(\omega L_1 - \frac{1}{\omega C_1} \right) \right] \cdot \left[R_2 + R_L + j \left(\omega L_2 - \frac{1}{\omega C_2} \right) \right] + (\omega M)^2} \dot{U}_{1_SS}^2 \right)}{\left| \left[R_1 + j \left(\omega L_1 - \frac{1}{\omega C_1} \right) \right] \cdot \left[R_2 + R_L + j \left(\omega L_2 - \frac{1}{\omega C_2} \right) \right] + (\omega M)^2 \right|} \quad (19)$$

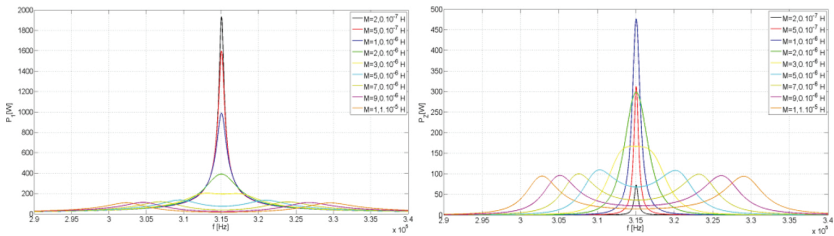


Figure 6. Input power (left) and output power (right) dependency on series-series coupling.

The highest efficiency can be achieved at the resonant frequency. Its value is above 90% when higher values of mutual inductance are considered. The main disadvantage of high efficiency achievement is that for a given value of M , the transmitted power is too low (**Figure 6**, right). This fact is crucial when simultaneously high efficiency together with high power transfer is required. The solution is to operate the system at the frequency which is given by Eq. (20).

$$\left[R_1 + j \left(\omega L_1 - \frac{1}{\omega C_1} \right) \right] \dot{I}_{1_SP} - j \omega M \dot{I}_{2_SP} = \dot{U}_{1_SP} \quad (20)$$

At such frequency, with value depending on the value of mutual inductance (distance between the transmitting and receiving coils), it is possible to achieve a quite high value of the system

efficiency together with peak power transfer. For example, when the system has $M = 5 \mu\text{H}$, which is relevant to 40 cm of distance between coils, then almost 85% of the system efficiency can be achieved at the peak power that is transferred to the load. As it can be further seen in **Figure 7** (right), the value of efficiency naturally depends on the value of the output load. Anyway, it is still possible to achieve an acceptable value of system efficiency even at the sharp change of the output load. Such behavior is mostly welcomed for perspective wireless charging systems, where high transmitting distance, high efficiency, high transferred power, and variable load are required.

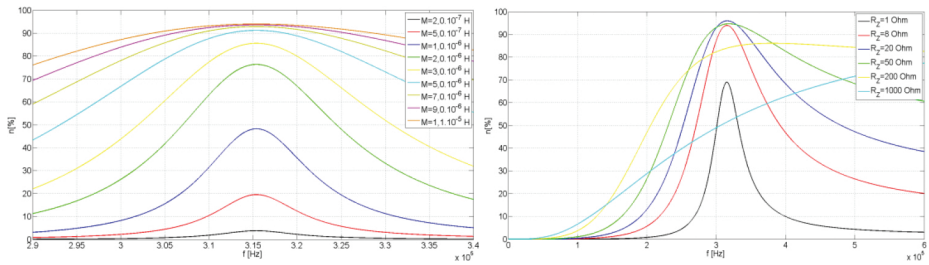


Figure 7. Dependency of efficiency on the series-series coupling (left) and on the output load change at $M = 11 \mu\text{H}$ (right).

From the practical point of view, during the design process of the system, it is necessary to know the voltage waveform at compensation capacitors because these components are the most critical. Figures 8 and 9 show voltage dependency for each system component. It can be seen that even for a very low value of the supply voltage (in this case 30 V), the peak voltage at each component multiplies several times. Situation is most critical when the system operates at resonant frequency and also when a low value of mutual inductance is presented. If the input voltage rises, then naturally each particular voltage rises correspondingly too. The selection of the proper capacitor structure and configuration therefore means the most difficult issue. Thus, the previous recommendation for system operation at border resonant frequencies (19) also gives advantages from the system component design point of view. The same is valid

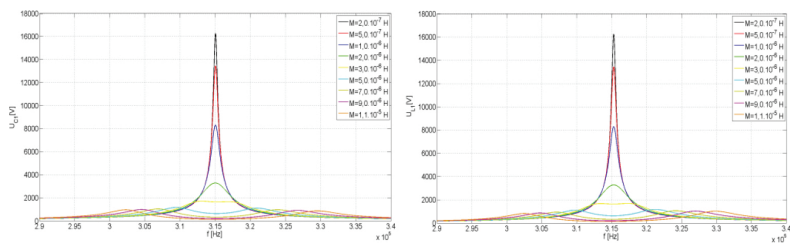


Figure 8. Dependency of voltage on the primary compensation capacitor C_1 (left) and on the primary coil L_1 (right) for series-series coupling.

for the wire selection of the transmitting and receiving coils, when the source and load current show similar dependency, as the previous circuit variables (**Figure 10**).

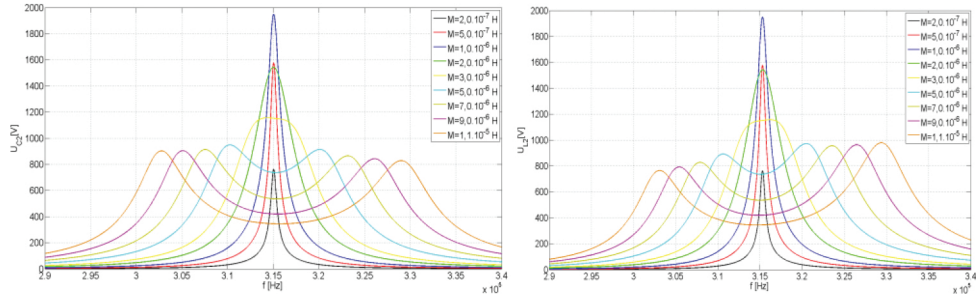


Figure 9. Dependency of voltage on the secondary compensation capacitor C_2 (left) and on the secondary coil L_2 (right) for series-series coupling.

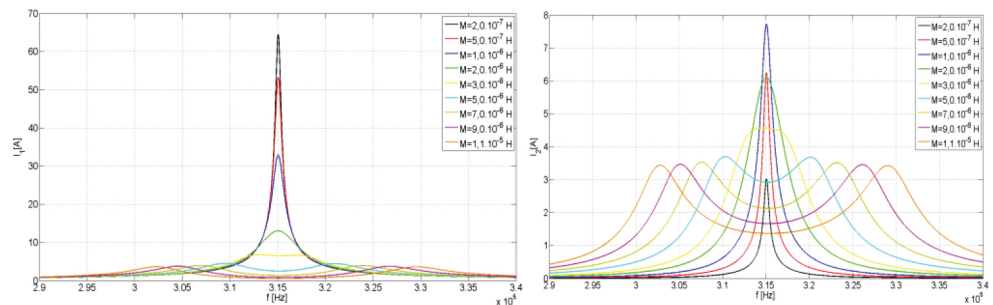


Figure 10. Source current (left) and load current (right) dependency on series-series coupling.

4. Series-parallel resonant coupling of the WET system

Series-parallel compensation means that one capacitor is connected in series to the transmitting coil and the other one is connected in parallel to the receiving coil, see **Figure 11**.

Using the method of loop currents, the impedance matrix of series-parallel compensated circuit can be expressed as follows (24):

$$-j\omega M \cdot I_{1_SP} + \left[R_2 + j \left(\omega L_2 - \frac{1}{\omega C_2} \right) \right] \cdot I_{2_SP} + j \frac{1}{\omega C_2} \cdot I_{3_SP} = 0 \quad (21)$$

$$\begin{aligned}
 Z_1 &= R_1 + j \left(\omega L_1 - \frac{1}{\omega C_1} \right) \\
 Z_2 &= R_2 + j \left(\omega L_2 - \frac{1}{\omega C_2} \right) \\
 j \frac{1}{\omega C_2} \dot{I}_{2_SP} + \left[R_L - j \frac{1}{\omega C_2} \right] \dot{I}_{3_SP} &= 0
 \end{aligned} \tag{22}$$

$$\begin{bmatrix} \dot{U}_{1_SP} \\ 0 \\ 0 \end{bmatrix} = \begin{bmatrix} R_1 + j \left(\omega L_1 - \frac{1}{\omega C_1} \right) & -j\omega M & 0 \\ -j\omega M & R_2 + j \left(\omega L_2 - \frac{1}{\omega C_2} \right) & j \frac{1}{\omega C_2} \\ 0 & j \frac{1}{\omega C_2} & R_L - j \frac{1}{\omega C_2} \end{bmatrix} \begin{bmatrix} \dot{I}_{1_SP} \\ \dot{I}_{2_SP} \\ \dot{I}_{3_SP} \end{bmatrix} \tag{23}$$

$$\begin{bmatrix} \dot{U}_{1_SP} \\ 0 \\ 0 \end{bmatrix} = \begin{bmatrix} R_1 + j \left(\omega L_1 - \frac{1}{\omega C_1} \right) & -j\omega M & 0 \\ -j\omega M & R_2 + j \left(\omega L_2 - \frac{1}{\omega C_2} \right) & j \frac{1}{\omega C_2} \\ 0 & j \frac{1}{\omega C_2} & R_L - j \frac{1}{\omega C_2} \end{bmatrix} \begin{bmatrix} \dot{I}_{1_SP} \\ \dot{I}_{2_SP} \\ \dot{I}_{3_SP} \end{bmatrix} \tag{24}$$

If we substitute $Z_1 = R_1 + j(\omega L_1 - \frac{1}{\omega C_1})$ and $Z_2 = R_2 + j(\omega L_2 - \frac{1}{\omega C_2})$, the circuit currents can be expressed as follows:

$$\dot{I}_1 = \dot{I}_{1_SP} = \frac{R_2 + j \frac{1}{\omega C_2(j\omega C_2 R_L + 1)}}{R_1 R_2 + \omega^2 M^2 + j \frac{R_1}{\omega C_2(j\omega C_2 R_L + 1)}} \dot{U}_{1_SP} \tag{25}$$

$$\dot{I}_2 = \dot{I}_{2_SP} = \frac{j\omega M}{R_1 R_2 + \omega^2 M^2 + j \frac{R_1}{\omega C_2(j\omega C_2 R_L + 1)}} \dot{U}_{1_SP} \tag{26}$$

$$\dot{I}_3 = \dot{I}_{2_SP} - \dot{I}_{3_SP} = \frac{-\omega^2 C_2 R_L M}{(R_1 R_2 + \omega^2 M^2)(j\omega C_2 R_L + 1) + j \frac{R_1}{\omega C_2}} \dot{U}_{1_SP} \tag{27}$$

$$\dot{I}_4 = \dot{I}_{3_SP} = \frac{j\omega M}{(R_1 R_2 + \omega^2 M^2)(j\omega C_2 R_L + 1) + j \frac{R_1}{\omega C_2}} \dot{U}_{1_SP} \quad (28)$$

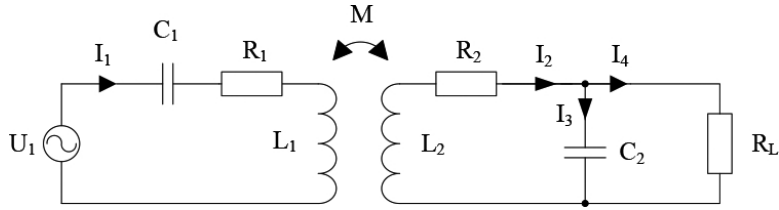


Figure 11. Equivalent circuit of the series-parallel compensated WET system.

Compared with the series-series compensation, in this case the reactance of capacitor C_2 influences circuit variables when circuit is powered by the resonant frequency because C_2 is in parallel to the load resistance R_L . In this case, the power consumption, output power, and efficiency can be calculated in the same way as in the case of series-series compensation (Eqs. (28)–(31)).

$$\dot{S}_{IN_SP} = \dot{I}_1 \dot{U}_{1_SP} = \frac{Z_2 + j \frac{1}{\omega C_2 (j\omega C_2 R_L + 1)}}{Z_1 Z_2 + \omega^2 M^2 + j \frac{Z_1}{\omega C_2 (j\omega C_2 R_L + 1)}} \dot{U}_{1_SP}^2 \quad (29)$$

$$P_{OUT_SP} = R_L |I_4|^2 = \left| \frac{-\omega^2 M^2 R_L}{\left[(Z_1 Z_2 + \omega^2 M^2)(j\omega C_2 R_L + 1) + j \frac{Z_1}{\omega C_2} \right]^2} \dot{U}_{1_SP}^2 \right| \quad (30)$$

$$\begin{aligned} \eta &= \left| \frac{P_{OUT_SP}}{\dot{S}_{IN_SP} \cdot \cos(\varphi)} \right| \\ &= \left| \frac{-\omega^2 M^2 R_L}{\left[Z_2 (j\omega C_2 R_L + 1) + j \frac{1}{\omega C_2} \right] \left[(Z_1 Z_2 + \omega^2 M^2)(j\omega C_2 R_L + 1) + j \frac{Z_1}{\omega C_2} \right] \cdot \cos(\varphi)} \right| \end{aligned} \quad (31)$$

$$\cos(\varphi) = \frac{\Re(\dot{S}_{IN})}{|\dot{S}_{IN}|} = \frac{\Re \left(\frac{Z_2 + j \frac{1}{\omega C_2(j\omega C_2 R_L + 1)} - U_{1_SP}^2}{Z_1 Z_2 + \omega^2 M^2 + j \frac{Z_1}{\omega C_2(j\omega C_2 R_L + 1)}} \right)}{\left| \frac{Z_2 + j \frac{1}{\omega C_2(j\omega C_2 R_L + 1)} - U_{1_SP}^2}{Z_1 Z_2 + \omega^2 M^2 + j \frac{Z_1}{\omega C_2(j\omega C_2 R_L + 1)}} \right|} \quad (32)$$

The graphical interpretations of the mentioned variables are introduced depending on frequency as well as M (Figures 12–14). Small change of frequency from resonant frequency causes that power consumption and power delivered to the load are significantly reduced (**Figure 12**). Considering similar dependency for efficiency, it shows no change when frequency is being changed (**Figure 13**, left). This is advantageous when power delivery at constant efficiency needs to be managed.

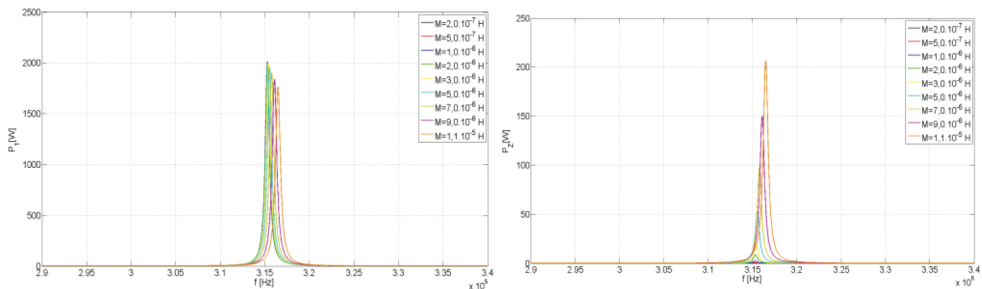


Figure 12. Input power (left) and output power (right) dependency on series-parallel coupling.

On the other hand, the poor efficiency is the highest disadvantage. Let now consider a different situation, when M reaches higher values (reduction of distance between coils). **Figure 13** (right) shows that the efficiency is significantly increased. This means that the best efficiency can be achieved for a short distance, while power transfer to the load is comparable with power transfer for series-series compensation, see **Figure 14** (left).

Efficiency also depends on the change of the load value. For series-parallel compensation, the higher efficiency can be achieved at higher values of load resistance (reduction of delivered power). **Figure 14** (right) shows dependency of system efficiency on series-parallel compensation at constant $M = 11 \mu\text{H}$ during load change. It can be seen that for lower transfer distances ($M = 11 \mu\text{H}$ is relevant to 20 cm of mutual distance), the efficiency can be kept at high values even for a wide range of load (**Figure 14**).

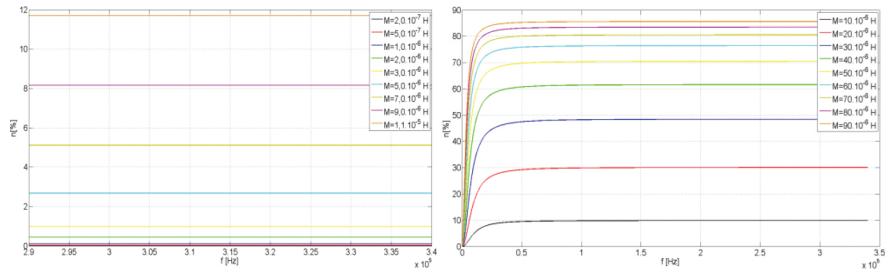


Figure 13. Dependency of efficiency on series-parallel coupling (left) and on higher values of mutual inductance (right).

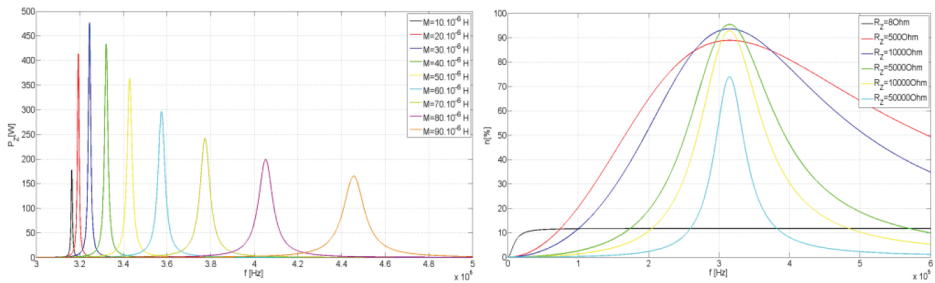


Figure 14. Dependency of the output power on higher values of mutual inductance (left) and dependency of efficiency (right) on variable load at constant $M = 11 \mu\text{H}$.

Voltage on capacitor C_1 (**Figure 15**) in the series-parallel compensated system also achieves high levels. A decrease or increase in the switching frequency not only reduces the voltage stresses on the capacitor, but also significantly reduces the transmitted power. The same situation is valid for the voltage on coil L_1 .

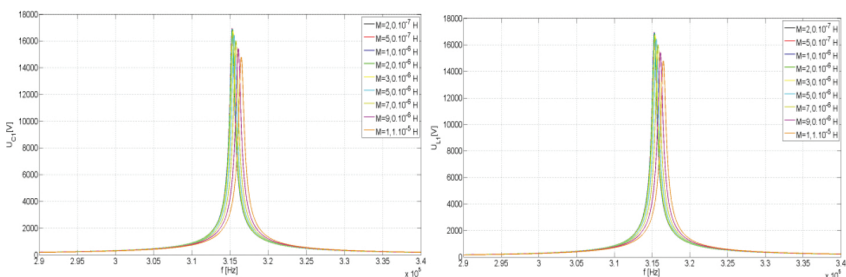


Figure 15. Dependency of voltage on the primary compensation capacitor C_1 (left) and on the primary coil L_1 (right) for series-parallel coupling.

Voltage on capacitor C_2 (**Figure 16**, left) is the voltage on the resistive load and the receiver coil L_2 too because they are connected in parallel. In contrast to the voltage on capacitor C_1 , the voltage on capacitor C_2 is smaller. This voltage is increased when value of M is increased too, but only up to a certain value of the mutual inductance, in our case it is $30 \mu\text{H}$. The voltage on capacitor C_2 falls above this value. Capacitor C_2 does not have to be necessarily designed for high voltage stresses, which reduces the overall costs of the system.

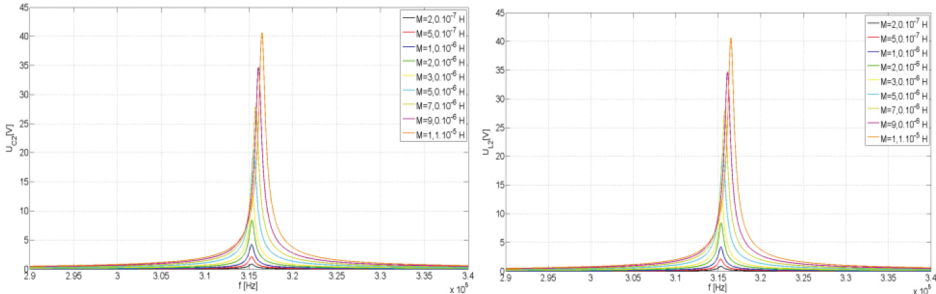


Figure 16. Dependency of voltage on the secondary compensation capacitor C_2 (left) and on the secondary coil L_2 (right) for series-parallel coupling.

Frequency dependencies of circuit currents are shown in Figures 17 and 18. It can be seen (**Figure 17**, left) that I_1 decreases with the increase in the mutual inductance and its peak point is shifted to higher frequencies contrary to resonant frequency.

Figures 17 (right) and 18 show the current of the receiving coil I_2 divided into current of capacitor C_2 and a load resistance R_L . Because the value of load resistor is realatively small, $R_L = 8 \Omega$, the majority of coil current flows just through load resistance, I_4 . Current I_3 of the secondary capacitor C_2 has smaller magnitude. With the increase in the mutual inductance, the maximum of all currents rises.

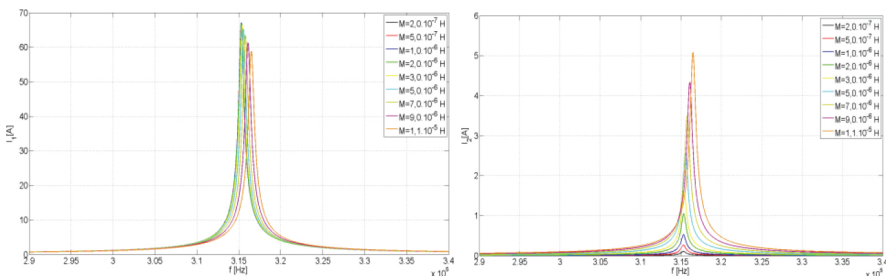


Figure 17. Dependency of current I_1 (left) and I_2 (right) on series-parallel coupling.

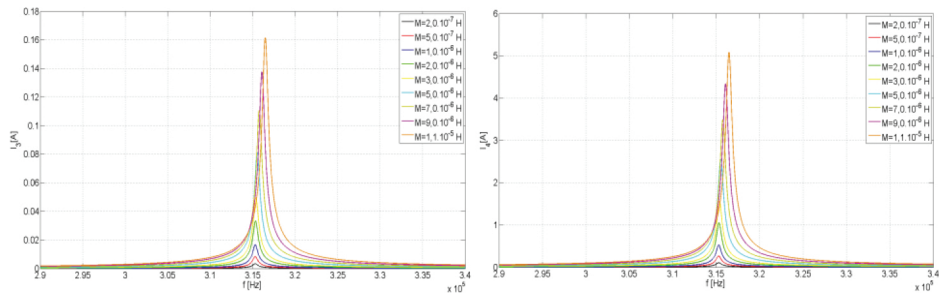


Figure 18. Dependency of current I_3 (left) and I_4 (right) on series-parallel coupling.

5. Parallel-series resonant coupling of the WET system

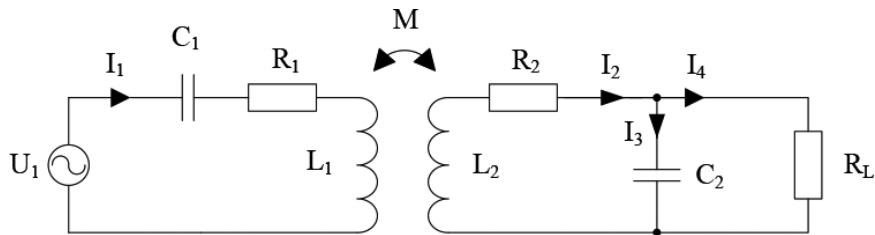


Figure 19. Equivalent circuit of the parallel-series compensated WET system.

Equivalent circuit for parallel-series compensation is shown in **Figure 19**. Capacitor C_1 is connected in parallel to the power supply and transmitting coil. The secondary consists of series connection of $L_2-C_2-R_L$.

With consideration of equivalent circuit shown in **Figure 9**, it is possible to express a system of three linear equations with three unknown parameters (14).

$$\begin{bmatrix} \dot{U}_{1_PS} \\ 0 \\ 0 \end{bmatrix} = \begin{bmatrix} -j\frac{1}{\omega C_1} & j\frac{1}{\omega C_1} & 0 \\ j\frac{1}{\omega C_1} & R_1 + j\omega L_1 - j\frac{1}{\omega C_1} & -j\omega M \\ 0 & -j\omega M & R_2 + R_L + j\left(\omega L_2 - \frac{1}{\omega C_2}\right) \end{bmatrix} \cdot \begin{bmatrix} \dot{I}_{1_PS} \\ \dot{I}_{2_PS} \\ \dot{I}_{3_PS} \end{bmatrix} \quad (33)$$

Equation (32) gives relatively complicated results and therefore some simplifying substitution should be applied: $Z_1 = R_1 + j\left(\omega L_1 - \frac{1}{\omega C_1}\right)$ and $Z_2 = R_2 + R_L + j\left(\omega L_2 - \frac{1}{\omega C_2}\right)$. The aimed winding and load currents are determined by Eqs. (33)–(35):

$$\dot{I}_1 = \dot{I}_{1_PS} = \frac{j\omega C_1(Z_1 Z_2 + \omega^2 M^2)}{Z_1 Z_2 + (\omega M)^2 + j \frac{Z_2}{\omega C_1}} \dot{U}_{1_PS} \quad (34)$$

$$\dot{I}_2 = \dot{I}_{1_PS} - \dot{I}_{2_PS} = \frac{j\omega C_1(Z_1 Z_2 + \omega^2 M^2) - Z_2}{Z_1 Z_2 + (\omega M)^2 + j \frac{Z_2}{\omega C_1}} \dot{U}_{1_PS} \quad (35)$$

$$\dot{I}_4 = \dot{I}_{3_PS} = \frac{j\omega M}{Z_1 Z_2 + (\omega M)^2 + j \frac{Z_2}{\omega C_1}} \dot{U}_{1_PS} \quad (36)$$

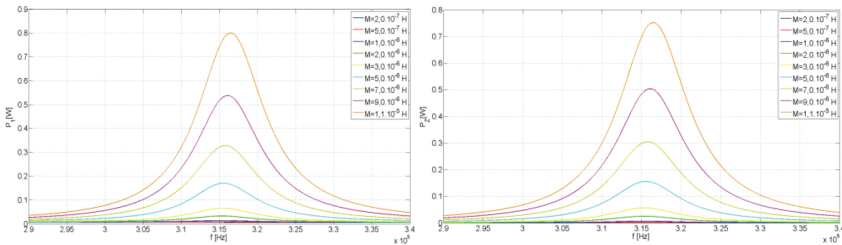


Figure 20. Input power (left) and output power (right) dependency on series-parallel coupling.

The input and output powers are then found in the same way as from previous analyses (36)–(37).

$$\dot{S}_{IN_PS} = \dot{I}_1 \dot{U}_{1_PS} = \frac{j\omega C_1(Z_1 Z_2 + \omega^2 M^2)}{Z_1 Z_2 + (\omega M)^2 + j \frac{Z_2}{\omega C_1}} \dot{U}_{1_PS}^2 \quad (37)$$

$$P_{OUT_SP} = R_L \cdot |\dot{I}_4|^2 = \left| \frac{-\omega^2 M^2 R_L}{Z_1 Z_2 + (\omega M)^2 + j \frac{Z_2}{\omega C_1}} \dot{U}_{1_SP}^2 \right| \quad (38)$$

where

$$\cos(\varphi) = \frac{\Re(\dot{S}_{IN})}{|\dot{S}_{IN}|} = \frac{\Re \left(\frac{j\omega C_1(Z_1 Z_2 + \omega^2 M^2)}{Z_1 Z_2 + (\omega M)^2 + j \frac{Z_2}{\omega C_1}} \dot{U}_{1_PS}^2 \right)}{\left| \frac{j\omega C_1(Z_1 Z_2 + \omega^2 M^2)}{Z_1 Z_2 + (\omega M)^2 + j \frac{Z_2}{\omega C_1}} \dot{U}_{1_PS}^2 \right|} \quad (39)$$

The graphical interpretation of Eq. (37) is shown in **Figure 20**. It shows that any frequency deviation from the resonant state reduces the power delivered to the load. However, in this case the system is less sensitive to frequency change as compared to the series-parallel compensation.

The power delivery to the load for this type of compensation and for the selected operational variables (load, mutual inductance, etc.) is, when compared to the previous types, very poor. Efficiency dependency (**Figure 21**) is comparable to series-parallel compensation, whereby the higher the value of the mutual inductance is, the higher efficiency can be achieved. Similarly, as for series-parallel compensation it is expected that the parallel-series compensation type is more valuable for higher values of mutual inductances, and thus for applications, where distance is not the primary attribution of the WET system.

The advantage of this configuration is the low electrical stress of individual components (Figures 22 and 23).

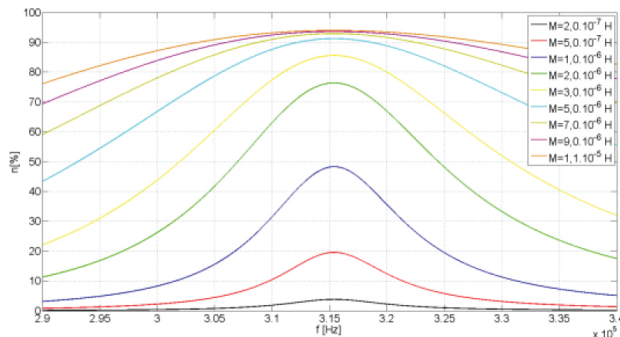


Figure 21. Dependency of efficiency on parallel-series coupling.

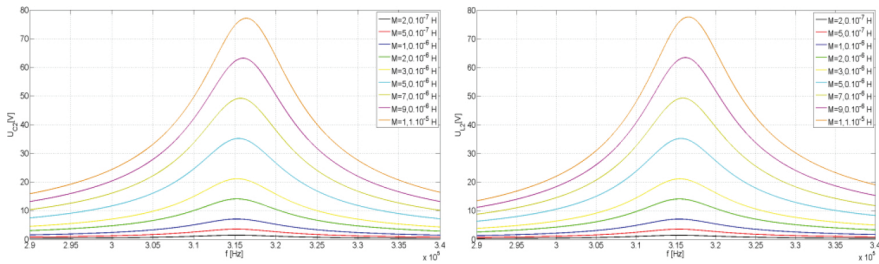


Figure 22. Dependency of voltage on the secondary compensation capacitor C_2 (left) and on the secondary coil L_2 (right) for parallel-series coupling.

6. Parallel-parallel resonant coupling of the WET system

Equivalent circuit of the system is shown in **Figure 23**. Both compensation capacitors are connected in parallel to the transmitting and receiving coils. Unlike the previous topologies, this model forms the system of four linear equations with four unknown parameters (26):

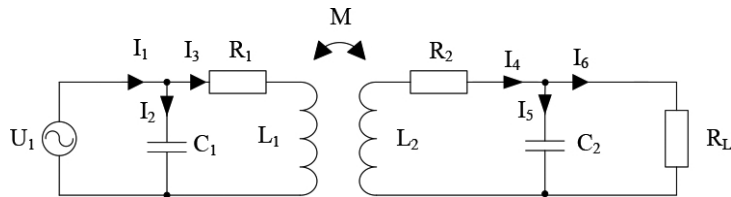


Figure 23. Equivalent circuit of the parallel-parallel compensated WET system.

$$\begin{bmatrix} \dot{U}_{1_PS} \\ 0 \\ 0 \\ 0 \end{bmatrix} = \begin{bmatrix} -j\frac{1}{\omega C_1} & j\frac{1}{\omega C_1} & 0 & 0 \\ j\frac{1}{\omega C_1} & R_1 + j\omega L_1 - j\frac{1}{\omega C_1} & -j\omega M & 0 \\ 0 & -j\omega M & R_2 + j\omega L_2 - j\frac{1}{\omega C_2} & j\frac{1}{\omega C_2} \\ 0 & 0 & j\frac{1}{\omega C_2} & R_L - j\frac{1}{\omega C_2} \end{bmatrix} \cdot \begin{bmatrix} \dot{I}_{1_PP} \\ \dot{I}_{2_PP} \\ \dot{I}_{3_PP} \\ \dot{I}_{4_PP} \end{bmatrix} \quad (40)$$

After substitution $Z_1 = R_1 + j\left(\omega L_1 - \frac{1}{\omega C_1}\right)$, $Z_2 = R_2 + j\left(\omega L_2 - \frac{1}{\omega C_2}\right)$, and $Z_3 = R_L - j\left(\frac{1}{\omega C_2}\right)$, the most important circuit variables can be obtained as follows:

$$\dot{I}_1 = \dot{I}_{1_PP} = \left[j\omega C_1 + \frac{1}{\left(Z_1 + j\frac{1}{\omega C_1} \right) + \frac{\omega^4 C_2^2 Z_3 M^2}{\omega^2 C_2^2 Z_2 Z_3 + 1}} \right] \dot{U}_{1_PP} \quad (41)$$

$$\dot{I}_6 = \dot{I}_{4_PP} = \frac{-\frac{M}{Z_3 C_2}}{\left(Z_1 + j\frac{1}{\omega C_1} \right) \left(\frac{1}{\omega^2 C_2^2 Z_3} + Z_2 \right) + (\omega M)^2} \dot{U}_{1_PP} \quad (42)$$

$$P_{OUT_PP} = R_L \cdot |\dot{I}_6|^2 = \left| \frac{R_L \left(-\frac{M}{Z_3 C_2} \right)^2}{\left[\left(Z_1 + j\frac{1}{\omega C_1} \right) \left(\frac{1}{\omega^2 C_2^2 Z_3} + Z_2 \right) + (\omega M)^2 \right]^2} \right| \dot{U}_{1_PP}^2 \quad (43)$$

$$\begin{aligned} \eta &= \left| \frac{P_{OUT_SP}}{\dot{S}_{IN_SP} \cdot \cos(\varphi)} \right| \\ &= \left| \frac{R_L M^2}{Z_3^2 C_2^2 \left[j\omega C_1 \left[\left(Z_1 + j\frac{1}{\omega C_1} \right) + \frac{\omega^4 C_2^2 Z_3 M^2}{\omega^2 C_2^2 Z_2 Z_3 + 1} \right]^2 + \left(Z_1 + j\frac{1}{\omega C_1} \right) + \frac{\omega^4 C_2^2 Z_3 M^2}{\omega^2 C_2^2 Z_2 Z_3 + 1} \right] \cos(\varphi)} \right| \end{aligned} \quad (44)$$

Regarding of the system performance, it is similar to characteristics found for nonresonant magnetic coupling. Thus, this type of compensation is not suitable for applications where simultaneously high power with high efficiency is required to transmit power on large distances.

7. Conclusion

Based on the study, a table (**Table 1**) of key operating features for the discussed compensation topologies is composed. **Table 1** only covers the system behavior at chosen frequency and distance range while considering constant supply voltage and low value of loading resistance.

In **Table 1**, attribute “A” marks the ability to transfer high power to the load, attribute “B” means that the system operates with maximal efficiency at the same time when it transmits

the maximal power. Attribute “C” distinguishes the compensation topology with higher frequency sensitivity and finally attribute “D” indicates the ability to reach theoretical transmitting efficiency, possibly higher than 90%.

Compensation	Evaluated categories			
	A	B	C	D
None		x		
Series-series	x		x	x
Series-parallel	x		x	
Parallel-series		x	x	x
Parallel-parallel		x		

Table 1. Overview of key performance features.

According to **Table 1**, the noncompensated system and the system with parallel-parallel compensation are both inappropriate for any type of wireless charger working at large distance and higher level of transmitting energy. On the other hand, they achieve maximum efficiency precisely at the moment they deliver maximum power. Hence, they should be used for low-cost micropower battery chargers which moreover require no frequency tuning.

In contrast to other topologies, the series-series compensation provides relatively high power even through a very large working air gap, but the efficiency reaches its peak only at off-resonant frequencies. The system should be therefore operated at compromise between useable energy and the transmitting efficiency. Despite this fact, the system is suitable for high-power chargers for electric vehicles.

The series-parallel compensation forms more disadvantages than advantages and therefore cannot be recommended for any battery charger. With respect to all evaluated categories, the parallel-series compensation provides the best performance, but from power delivering point of view, this solution is much worse. However, it could be recommended for high-end frequency tuned micropower battery chargers.

Acknowledgements

The authors wish to thank the Slovak grant agency VEGA for Project No. 0579/14 Research of topological structures of segments of power electronic system for wireless energy transfer.

Author details

Michal Frivaldsky*, Pavol Spanik, Peter Drgona, Viliam Jaros and Marek Piri

*Address all correspondence to: michal.frivaldsky@fel.uniza.sk

Department of Mechatronics and Electronics, Faculty of Electrical Engineering, University of Zilina, Slovakia

References

- [1] Wang, C.-S.; Stielau, O.H.; Covic, G.A. Design Considerations for a Contactless Electric Vehicle Battery Charger. *IEEE Transactions on Industrial Electronics*. 2005;52(5):1308–1314.
- [2] Hui, S.Y.R.; Zhong, W.; Lee, C.K. A Critical Review of Recent Progress in Mid-Range Wireless Power Transfer. *IEEE Transactions on Power Electronics*. 2014;29:4500–4511.
- [3] Covic, G.A.; Boys, J.T. Modern Trends in Inductive Power Transfer for Transportation Applications. *IEEE Journal of Emerging and Selected Topics in Power Electronics*. 2013;1:28–41.
- [4] Zhai, H.; Pan, H.K.; Lu, M. A practical wireless charging system based on ultra-wideband retro-reflective beam forming. *Antennas and Propagation Society International Symposium*. 2010:1–4.
- [5] Kim, S.; Jung, D.H.; Kim, J.J.; Bae, B.; Kong, S.; Ahn, S.; Kim, J.; Kim, J. High-Efficiency PCB- and Package-Level Wireless Power Transfer Interconnection Scheme Using Magnetic Field Resonance Coupling. *IEEE Transactions on Components Packaging and Manufacturing Technology*. 2015;5(7):863–878.
- [6] Covic, G.A.; Boys, J.T. Inductive Power Transfer. *Proceedings of the IEEE*. 2013;101(6):1–14.
- [7] Kurs, A.; Karalis, A.; Moffatt, R.; Joannopoulos, J.D.; Fisher, P.; Soljacic, M. Wireless Power Transfer via Strongly Coupled Magnetic Resonances. *Science*. 2007;317(5834):83–86.
- [8] Peschiera, B.; Williamson, S.S. Review of inductive power transfer technology for electric and plug-in hybrid electric vehicles, in *Industrial Electronics Society. IECON 2013—39th Annual Conference of the IEEE*. 2013:4672–4677.
- [9] Dai, J.; Ludois, D.C. A Survey of Wireless Power Transfer and a Critical Comparison of Inductive and Capacitive Coupling for Small Gap Applications. *IEEE Transactions on Power Electronics*. 2015;30(11):6017–6029.

Wireless Power Transfer by Using Magnetically Coupled Resonators

Ali Agcal, Selin Ozcira and Nur Bekiroglu

Additional information is available at the end of the chapter

<http://dx.doi.org/10.5772/64031>

Abstract

In this chapter, a wireless power transmission system based on magnetic resonance coupling circuit was carried out. Mathematical expressions of optimal coupling coefficients were examined with the coupling model. Equivalent circuit parameters were calculated with Maxwell 3D software, and then, the equivalent circuit was solved using MATLAB technical computing software. The transfer efficiency of the system was derived using the electrical parameters of the equivalent circuit. System efficiency was analyzed depending on the different air gap values for various characteristic impedances using PSIM circuit simulation software. Since magnetic resonance coupling involves creating a resonance and transferring the power without the radiation of electromagnetic waves, resonance frequency is a key parameter in system design. The aim of this research was to define the efficiency according to variations of coefficients in wireless power transfer (WPT) system. In order to do that, the calculation procedure of mutual inductance between two self-resonators is performed by Maxwell software. Equivalent circuit is solved in circuit simulator PSIM platform. The calculations show that using the parameters that are obtained by magnetic analysis can be used for the equivalent circuit which has the capability to provide the efficiency using electrical quantities. The chapter discusses the application of this approach to a coil excited by a sinusoidal voltage source and a receiver coil, which receives energy voltage and current. Both could be obtained to calculate the instantaneous power and efficiency. To do so, the waveforms for voltage and current were obtained and computed with the PSIM circuit simulator. As the air gap between the coils increased, the coupling between the coils was weakened. The impedance of the circuit varied as the air gap changed, affecting the power transfer efficiency. In order to determine the differences between the software programs, efficiency values were calculated using three kinds of software. And it is concluded that equivalent circuit analysis by means of numerical computing is proper to obtain the voltage and current waveforms. Correspondingly, transmission efficiency can be calculated using the electrical relations.

Keywords: wireless power transfer, magnetically coupling resonators, efficiency variations

1. Introduction

Wireless power transfer (WPT) has become popular recently and is expected to be used in plenty of technological devices. The main reason for the recent intense interest in WPT is the sharp increase in the use of electrical devices with various sizes and types of batteries. The main purpose of WPT research was the transfer of as much power as possible, with the goal of high system efficiency in spite of low mutual inductance between coils.

In the literature, one of the popular publications that take range variations into consideration is [1]. Critical coupling, frequency splitting, and impedance matching issues were analyzed in [1] using single-turn axillary loops to amplify the magnetic coupling added to resonators. In [1], the authors revealed 50% efficiency for their system, which is suitable for various positions of the receiver.

It has become widely accepted to use a series resonating circuit as the equivalent circuit of a resonator to conduct analysis for resonant frequency [2]. In this context, different attempts have been made to develop a sufficiently precise model [3,4]. There have been many methods employed such as modification circuits and magnetic design of the core properties [5]. In those studies, the scattering parameters were calculated by two port network theory using a network analyzer.

The state space model was created to obtain an accurate mathematical model of wireless power transfer (WPT) in [6,7], in which the transfer function of the bidirectional IPT system was obtained. As the Ziegler–Nichols method has high overshoot, it was optimized the PID parameters with a phase margin of 60° [8]. The PID parameters were optimized using the genetic algorithm in order to achieve better transient performance in [9]. The dynamic behavior ought to be as fast as possible in [10], in which the H-bridge circuit structure was inserted into the dynamic model. In [11], authors proposed a dynamic model for a multi-pickup system. To overcome the higher order problem and make a straightforward real dynamic model from the energy point of view, it was built a dynamic model of the WPT including a nonlinear inverter and rectifier in [12].

In [13], authors proposed a design methodology using a series-series (S-S) contactless power transfer system for an EV battery charger with two fixed operating frequencies. The converter operates at one of the fixed frequencies for a load-independent current output and at the other operating frequency for a load-independent voltage output. It was proposed hybrid topologies using either SS and PS compensation or SP and PP compensation for battery charging [14]. Controlling output current or voltage is achieved with two different methods. One is PWM (Pulse width modulation) control at a constant frequency at which huge changes in the duty

cycle will not allow zero voltage switching (ZVS) [15]. Cost analysis was performed in [16], and the results showed that coils are the most expensive part of the system.

System analysis in terms of electrical circuit is necessary since magnetic resonance coupling involves creating LC resonance. To derive the analytical equations of the input impedance and transferred power, a simplified circuit model of the WPT systems can be used. In order to calculate parameters such as current and voltage as a function of frequency at various air gap values and load conditions, mutual inductance between two self-resonators can be obtained from magnetic circuit analysis. And the parameters that are obtained by magnetic analysis can be used to solve the equivalent circuit which makes it possible to calculate the efficiency using electrical relations.

2. Magnetic resonance circuit

Resonance is observed in many different ways in nature. In general, resonance denotes the oscillation of energy between two different modes. For example, a mechanical pendulum oscillates between potential and kinetic forms of energy. While a system is in resonance, a huge amount of energy can be stored with lower excitation. If the energy intake speed ratio of the system is larger than the energy loss ratio of the system, energy accumulation occurs.

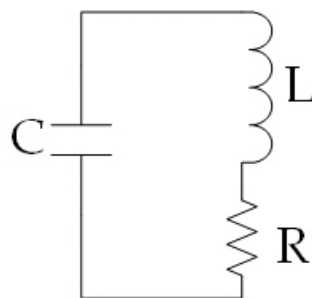


Figure 1. Resonator.

An example of an electro-magnetic resonator circuit with a coil, a capacitor, and a resistor is shown in **Figure 1**.

In this circuit, the energy oscillates between the coil (which stores energy in the magnetic field) and capacitors (which store energy in an electric field) at a certain resonance frequency.

$$\omega_0 = \frac{1}{\sqrt{LC}} \quad (1)$$

$$Q = \sqrt{\frac{L}{C}} \frac{1}{R} = \frac{\omega_0 L}{R} \quad (2)$$

From Eq. (2), it can be seen that the quality factor of the system increases, decreasing the circuit loss (the reduction of R).

In a high-resonance wireless power transfer system, the resonator system must have a high quality factor for efficient energy transfer. High quality factor electromagnetic resonators are normally made from the conductive components which have relatively narrow resonant frequency widths. The resonance frequency range is narrow, and resonators can be designed to reduce their interactions with foreign objects.

If two resonators are placed close to one another, the resonators can form a link and will be able to exchange energy. The efficiency of the energy exchange varies depending on each resonator and the coupling ratio k. The dynamics of a system with two resonators can be identified from the coupling mode theory or from equivalent circuit analysis of the connection system for the resonator. The equivalent circuit for coupled resonators has a series resonance circuit structure as shown in **Figure 2**.

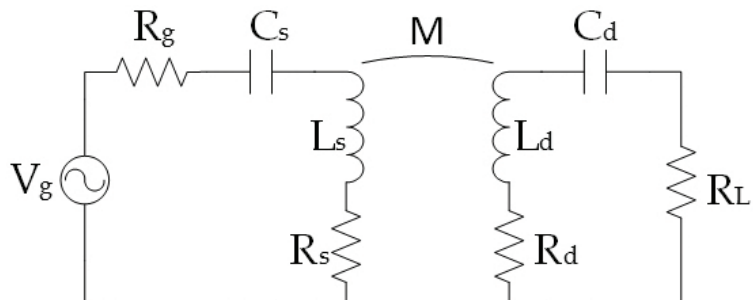


Figure 2. Equivalent circuit of coupled resonator system.

Here, R is the source internal resistance and the frequency is $\omega(2\pi f)$. Vg is called amplitude of the voltage source. L_s and L_d are source and device resonator coils, respectively. And mutual inductance is indicated by $M = k\sqrt{L_s L_d}$. Each coil has a series capacitor that forms a resonator. R_s and R_d resistors denote unwanted resistance (including ohmic and radiation losses) in the coil and the resonance capacitor for each resonator. AC load resistance is shown as R_L .

The yield for this circuit can be determined from the ratio of transmitted power for load resistance to the maximum available power of the source, while resonator system is strongly coupled.

$$\frac{P_L}{P_{g,max}} = \frac{4U^2 \frac{R_g R_L}{R_s R_d}}{\left[\left(1 + \frac{R_g}{R_s} \right) \left(1 + \frac{R_L}{R_d} \right) + U^2 \right]^2} \quad (3)$$

$$U = \frac{\omega M}{\sqrt{R_s R_d}} = k \sqrt{Q_s Q_d} \quad (4)$$

To provide the best system performance, proper load and source resistance can be selected or other resistance values can be captured using an impedance matching link. If the resistance is selected using Eq. (5),

$$\frac{R_g}{R_s} = \frac{R_L}{R_d} = \sqrt{1 + U^2} \quad (5)$$

power transfer efficiency can be expressed by Eq. (6)

$$\eta_{opt} = \frac{U^2}{\left(1 + \sqrt{1 + U^2} \right)^2} \quad (6)$$

Using Eq. (6), the maximum power transmission efficiency can be depicted as in **Figure 3**.

Systems with large values of U can achieve highly efficient energy transfer. Best wireless energy transfer system efficiency can be possible by determining the performance factors of the system, such as U which is depend on magnetic coupling coefficient k, and quality factors of the Q_s (source) and Q_d (device).

For certain applications, the resonator quality factor and magnetic coupling between resonators are used to determine the best possible performance for the system.

For wireless power transfer, it can be seen in Eq. (4) that the magnetic coupling coefficient and quality factor of the significance is greater. The magnetic coupling coefficient represents the magnetic flux connection between the source, while the device resonator is a dimensionless parameter with a value between 0 (unconnected) and 1 (complete flux linked). Conventional induction-based wireless power transmission systems (such as electric toothbrushes) have a high coupling value and a close range, aligned between the source and the device. Eq. (4) indicates that a high-quality resonator is more efficient than a traditional induction system. More importantly, it becomes possible to work efficiently at low coupling values. Also, for this reason, the need for precise positioning between the source and the device is eliminated. Unfortunately, the biggest drawback of the high quality factor is that the capacitor's peak

voltage is too high. The relationship between the peak value of the capacitor voltage and the quality is shown in Eq. (7) [17].

$$V_{Cpeak} = Q \frac{2V_s}{\pi} \quad (7)$$

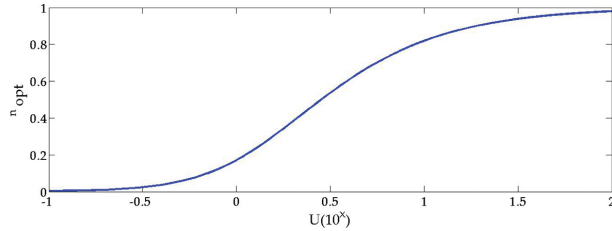


Figure 3. Depending on the U function, the optimum efficiency graph of energy transfer.

2.1. Magnetic coupling circuit

$$V_1 = I_1 \left(R + jL_1 \omega + \left(\frac{1}{j\omega C} \right) \right) - I_2 (jL_m \omega) \quad (8)$$

$$0 = I_2 \left(jL_2 \omega + \left(\frac{1}{j\omega C} \right) + Z_0 + R \right) - I_1 (jL_m \omega) \quad (9)$$

$$I_2 \left(jL_2 \omega + \left(\frac{1}{j\omega C} \right) + Z_0 + R \right) = I_1 (jL_m \omega) \quad (10)$$

$$I_2 = I_1 \left(\frac{jL_m \omega}{jL_2 \omega + \left(\frac{1}{j\omega C} \right) + Z_0 + R} \right) \quad (11)$$

$$V_1 = I_1 \left(R + jL_1 \omega + \left(\frac{1}{j\omega C} \right) \right) - I_1 \left(\frac{jL_m \omega}{jL_2 \omega + \left(\frac{1}{j\omega C} \right) + Z_0 + R} \right) (jL_m \omega) \quad (12)$$

$$V_1 = I_1 \left[\left(R + jL_1\omega + \left(\frac{1}{j\omega C} \right) \right) - \left(\frac{j^2 L_m^2 \omega^2}{jL_2\omega + \left(\frac{1}{j\omega C} \right) + Z_0 + R} \right) \right] \quad (13)$$

$$Z_{Eq} = Z_i = R + jL_1\omega + \left(\frac{1}{j\omega C} \right) + \left(\frac{L_m^2 \omega^2}{jL_2\omega + \left(\frac{1}{j\omega C} \right) + Z_0 + R} \right) \quad (14)$$

$$Z_{Eq} = R + jL_1\omega + \left(\frac{1}{j\omega C} \right) + \left(\frac{L_m^2 \omega^2}{jL_2\omega + \left(\frac{1}{j\omega C} \right) + Z_0 + R} \right) + jL_m\omega - jL_m\omega \quad (15)$$

$$Z_{Eq} = R + \left(\frac{1}{j\omega C} \right) + j(L_1 - L_m)\omega + \frac{-j^2 L_m^2 \omega^2 + j^2 L_m L_2 \omega^2 + jL_m\omega(Z_0 + R) + jL_m \left(\frac{1}{j\omega C} \right) \omega}{jL_2\omega + \left(\frac{1}{j\omega C} \right) + Z_0 + R} \quad (16)$$

$$Z_{Eq} = R + \left(\frac{1}{j\omega C} \right) + j(L_1 - L_m)\omega + \frac{(jL_m\omega)(j(L_2 - L_m)\omega + \left(\frac{1}{j\omega C} \right) + Z_0 + R)}{jL_2\omega + \left(\frac{1}{j\omega C} \right) + Z_0 + R} \quad (17)$$

$$Z_{Eq} = R + \left(\frac{1}{j\omega C} \right) + j(L_1 - L_m)\omega + \frac{1}{jL_2\omega + \left(\frac{1}{j\omega C} \right) + Z_0 + R + jL_m\omega - jL_m\omega} \\ \frac{(jL_m\omega)(j(L_2 - L_m)\omega + \left(\frac{1}{j\omega C} \right) + Z_0 + R)}{(jL_m\omega)(j(L_2 - L_m)\omega + \left(\frac{1}{j\omega C} \right) + Z_0 + R)} \quad (18)$$

$$Z_{Eq} = R + \left(\frac{1}{j\omega C} \right) + j(L_1 - L_m)\omega + \frac{1}{jL_m\omega + \frac{1}{j(L_2 - L_m)\omega + (1/j\omega C) + Z_0 + R}} \quad (19)$$

Since voltage and current are electrical quantities, the voltage equation can be written in a manner that calculates the electrical efficiency [18]. This leads to a set of equivalent impedance equations. The equivalent impedance is obtained by (19). Assuming $C = C_1 = C_2$ in the resonance coupling system, the efficiency can be defined by (22).

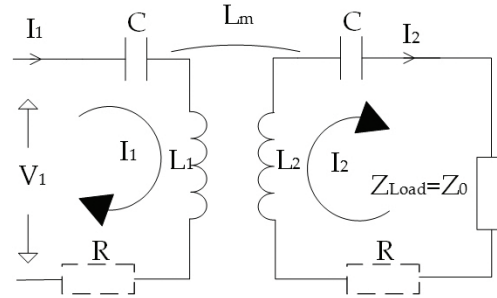


Figure 4. Magnetic coupling circuit.

2.2. Efficiency equation

$$\eta = \frac{P_{out}}{P_{in}} = \frac{I_{out}^2 Z_{out}}{I_{in}^2 Z_{Eq}} \quad (20)$$

Eq. (11) makes use of (21);

$$\frac{I_{out}}{I_{in}} = \frac{jL_m\omega}{jL_2\omega + \left(\frac{1}{j\omega C}\right) + Z_0 + R} \quad (21)$$

Eqs. (21) and (14) are substituted for Eq. (20);

$$\eta = \left(\frac{jL_m\omega}{jL_2\omega + \left(\frac{1}{j\omega C}\right) + Z_0 + R} \right)^2 \frac{Z_0}{R + jL_1\omega + \left(\frac{1}{j\omega C}\right) + \left(\frac{L_m^2\omega^2}{jL_2\omega + \left(\frac{1}{j\omega C}\right) + Z_0 + R} \right)} \quad (22)$$

At a given resonant frequency, the conditions for system efficiency are defined for three states, defined by Eqs. (23), (24), and (25).

$$L_m^2 = \frac{Z_0^2 - R^2}{\omega_0^2} \quad (23)$$

$$L_m^2 > \frac{Z_0^2 - R^2}{\omega_0^2} \quad (24)$$

$$L_m^2 < \frac{Z_0^2 - R^2}{\omega_0^2} \quad (25)$$

Eq. (23) describes the maximum efficiency condition, while Eq. (24) represents the double resonance frequency condition. Eq.(25) describes the condition of the system with a single-resonant frequency at low efficiency level [19].

3. Efficiency and characteristic impedance variation simulations with different software tools

Resonance frequency is a key parameter in system design, and the value can be changed by adjusting the distance between the transmission and characteristic impedance of the electrical circuit. First, the electrical circuit is created in a PSIM circuit simulator and the resulting voltage and current waveforms are obtained via the simulator. PSIM is simulation software designed for power electronics, motor control, and dynamic system simulation. The simulation is solved in the Matlab platform, and a procedure to calculate the parameters of the equivalent circuit is performed in Maxwell. For an air gap of 10 cm $L = 999.2\text{nH}$, $C = 124\text{pF}$, $L_m = 128.6\text{H}$, $Z_0 = 5\Omega$, the efficiency chart and variations in the equivalent impedance chart are given in **Figures 5 and 6**, respectively.

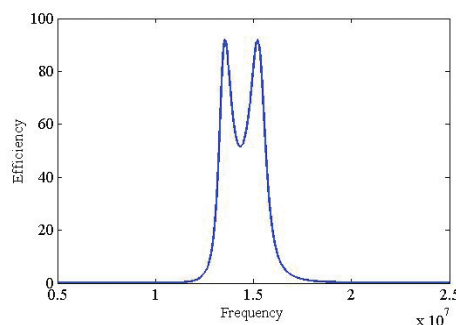


Figure 5. Efficiency chart.

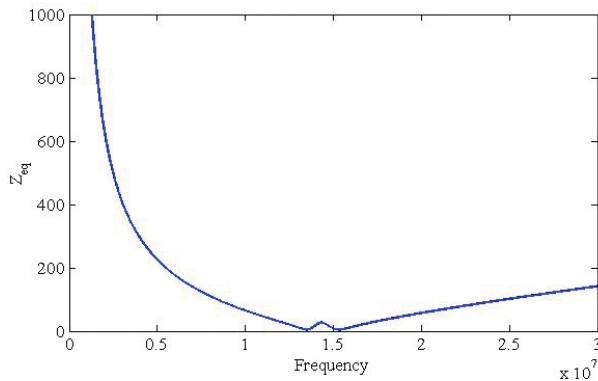


Figure 6. Equivalent impedance chart.

The transmitter and receiver coils have four different resonance coupling states: In the first state, both the transmitter and receiver coil loops are not resonant; in the second, the transmitter coil loop is in resonance, while the receiver coil loop is not; in the third, the transmitter coil loop is not resonant, while the receiver coil is; and in the last state, both the transmitter and receiver coil loops are resonant. When the whole coupling system is in resonance, the impedance value is at a minimum.

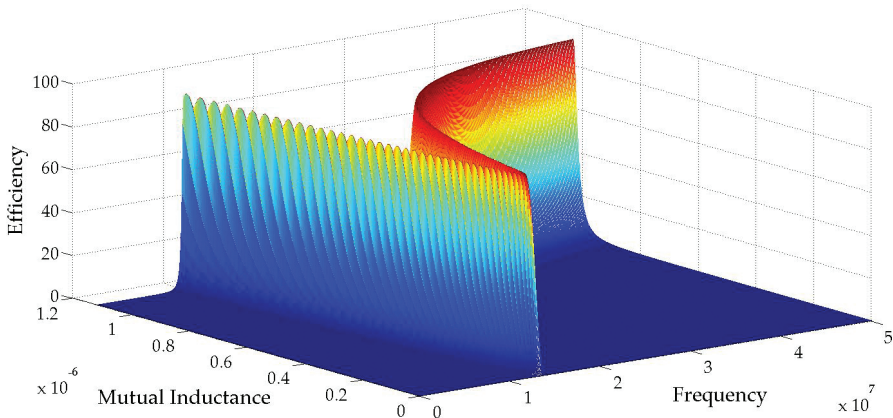


Figure 7. Function of efficiency according to mutual inductance and frequency.

The resonant frequencies change from two points to one depending on the length of the air gap. The double-resonance frequency region occurs at low impedance and short range. As the air gap distance and impedance increase, one resonance region appears. At this operation range, the efficiency falls sharply. The critical transmission efficiency would be the same as the peak efficiency over a coupled range.

The distance between the coils responsible for energy transfer should be kept at an optimum value since any increase in the air gap value will degrade the energy transfer ratio. This problem can be solved by optimizing the relation between the frequency and the quality factor.

Calculation of the parameters for the equivalent circuit was carried out in the Maxwell 3D software platform as well as in PSIM.

3.1. Maxwell 3D software simulation results

Hundred volts were used for the ideal sine source of 13.552 MHz. An inductance of winding value of 999.2 nH, mutual inductance of 128.6 nH, 124 pF capacitor values, R value of $0.22\ \Omega$, and Z_0 impedance value of $5\ \Omega$ were selected. The circuit scheme and modeled coils can be seen from **Figures 8 and 9**. The magnetic flux density graphs and waveforms of currents and voltage for air gap of 10 cm can be seen from **Figures 10–14**.

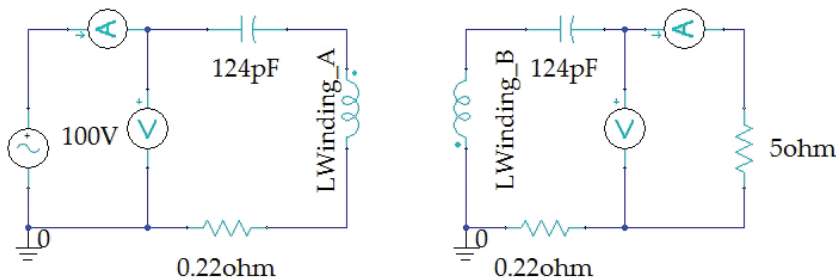


Figure 8. Maxwell 3D circuit scheme.

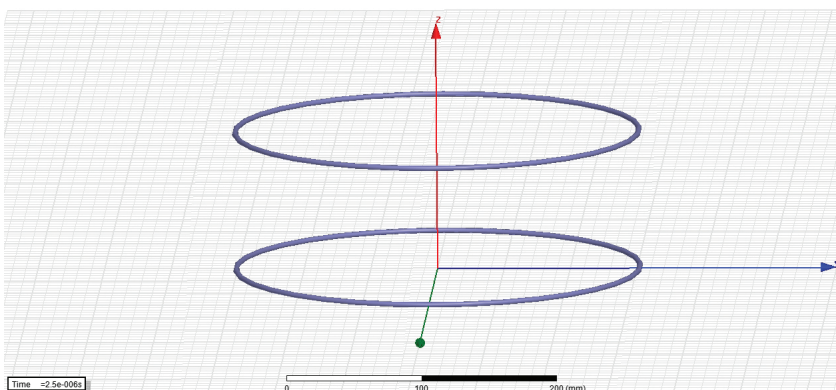


Figure 9. Receiver and transmitter coil for 10-cm air gap in Maxwell 3D.

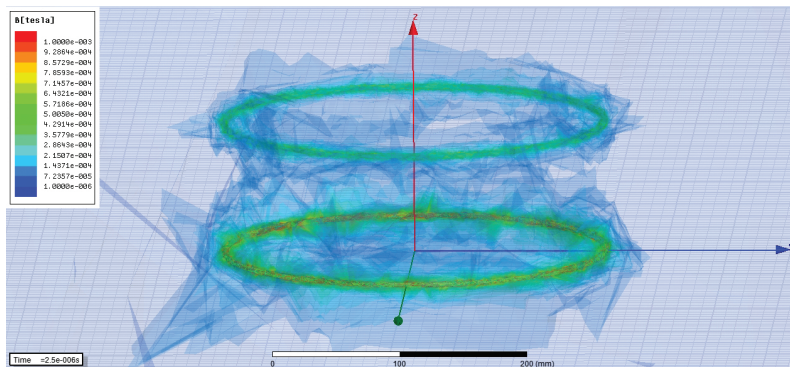


Figure 10. Magnetic flux density of receiver and transmitter coil for 10-cm air gap in Maxwell 3D.

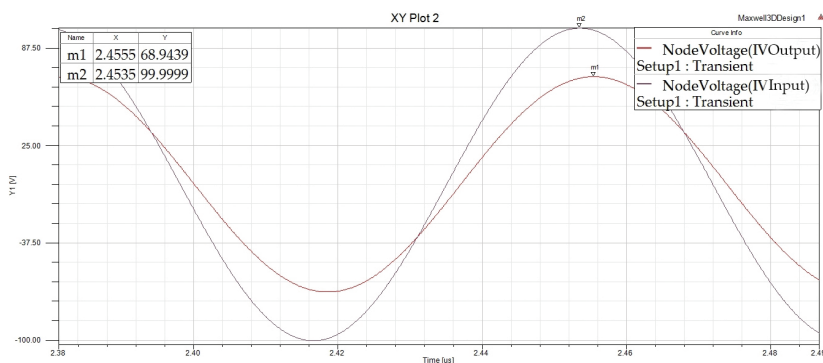


Figure 11. Maxwell 3D input and output voltages for 10-cm air gap and characteristic impedance of 5Ω .

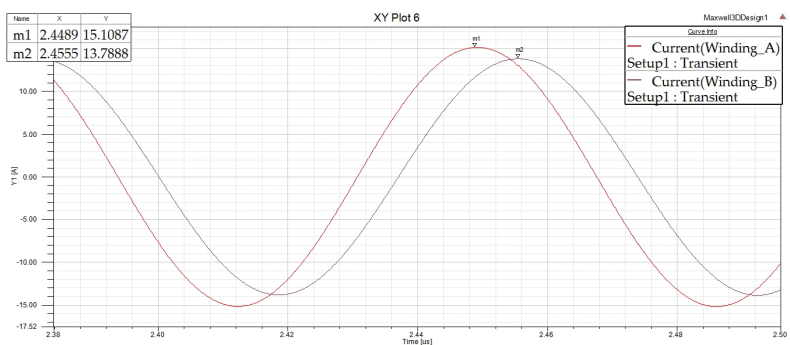


Figure 12. Maxwell 3D current passing through primary and secondary windings.

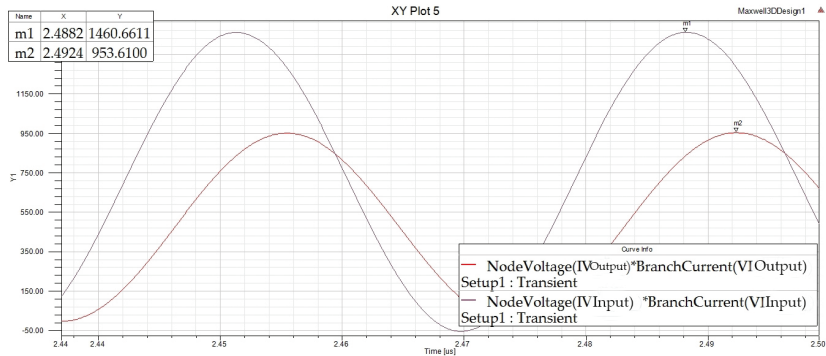


Figure 13. Maxwell 3D input and output power for 10-cm air gap and characteristic impedance of 5Ω .

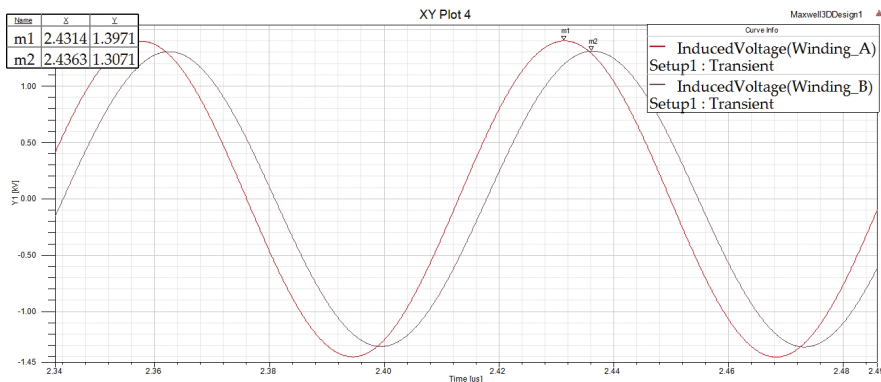


Figure 14. Maxwell 3D primary and secondary winding terminal voltage for 10-cm air gap and the characteristic impedance of 5Ω .

3.2. PSIM software simulation results

To determine the power and efficiency, the previously described methodology was followed. First, the mean required values for the circuit parameters for the Maxwell field simulator were computed. In the circuit simulation, the wireless power transfer system is driven by a sinusoidal voltage source with amplitude of 100 V. **Figure 15** shows the structure of the direct fed wireless power transfer. In order to illustrate how the model works, transient simulations were performed with the PSIM circuit simulator.

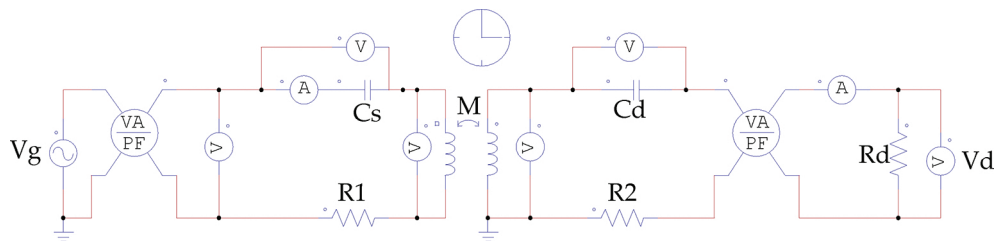


Figure 15. PSIM circuit scheme.

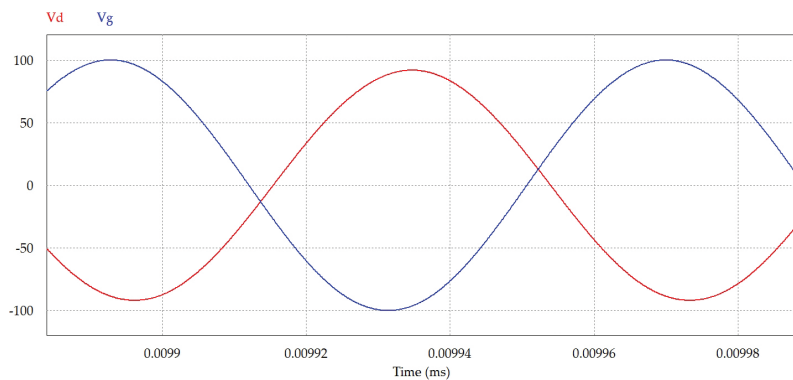


Figure 16. Air gap of 10 cm, characteristic impedance of 5Ω at 13.56 MHz input voltage (VP1 red line) and device voltage waveforms (VP2 blue line).

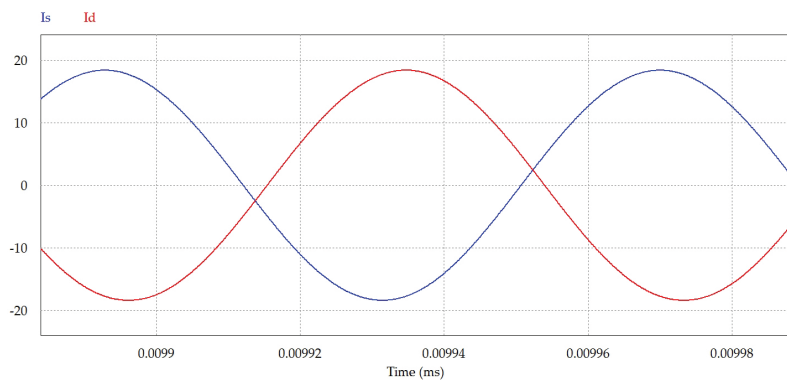


Figure 17. Air gap of 10 cm, characteristic impedance of 5Ω at 13.56 MHz input current (VP1 red line) and device input waveforms (VP2 blue line).

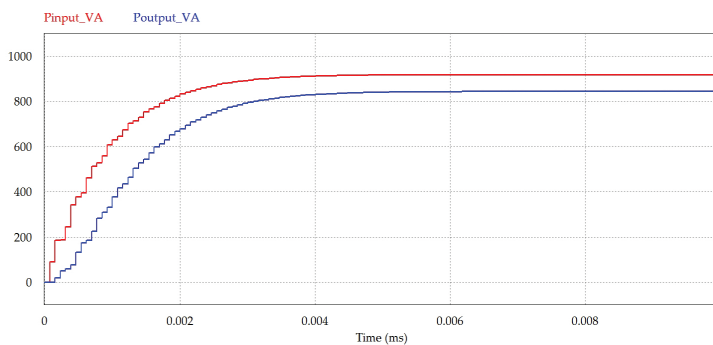


Figure 18. Air gap of 10 cm, characteristic impedance of 5Ω at 13.56 MHz (blue: input power, red: received power).

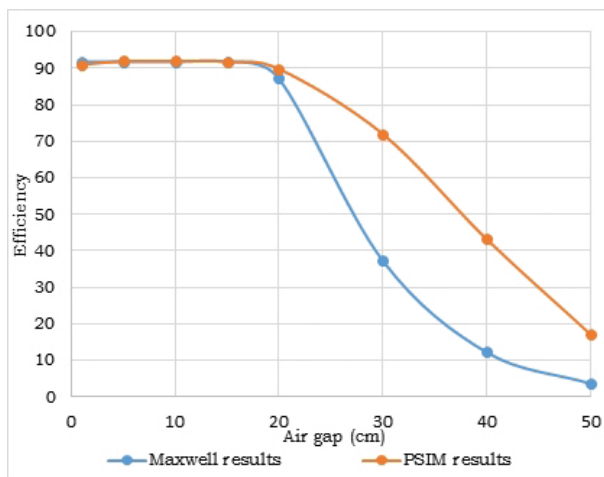


Figure 19. Magnetic resonance efficiencies according to software platforms.

The transmitting current was 13 A, and the receiving current was 12.88 A for a supply voltage of 70.71 V and the device voltage below 65 V. When input power was 919.2 VA, the amount of power delivery is 837 VA. Approximately 82.2 VA dissipated for losses and the transmitter required 0.098 W (an overhead loss) plus an additional input power of 1.098 VA for every additional 1 VA of power at the receiver.

When the same simulations run on Maxwell and PSIM software platforms for various air gap values, it is observed that for strongly magnetic coupled range up to air gap of 10 cm, efficiency values can be obtained similar. However, if the magnetic coupling gets loosely by the effect of elongated air gap distance, efficiency value differs. The reason of that is the numerical solution method. Therefore, numerical computing such as circuit simulators can calculate the quantities for strongly magnetic resonance couplings.

4. Conclusion

In this study, analysis of voltage and current waveforms in terms of magnetic resonance coupling is performed using numerical computing and a circuit simulator to define the efficiency of wireless power transfer in the time domain. This approach takes into consideration the nonlinear effects of power losses. The numerical results based on various air gap values are determined from equivalent circuit parameters which are obtained directly from Maxwell by the results of method of moments electromagnetics analysis. The calculation of mutual inductance between two self-resonators is also performed using the Maxwell software, and the equivalent circuit is solved in the circuit simulator PSIM platform.

The aim of this research was to define the efficiency according to the coefficients of variations for the WPT system. The parameters of the system affect the coupling coefficient; L_m is the mutual inductance parameter, while L_1 and L_2 are nonlinear loss resistance values that depend on the frequency and characteristic impedance of the system. The results were validated using the finite element method.

We concluded that equivalent circuit analysis by means of numerical computing is appropriate for determining the voltage and current waveforms. Additionally, transmission efficiency at a different distance range can be calculated based on the electrical relationship. Efficiency results with respect to load variation show that there are double-resonance frequency regions as well as one-resonance region. The resonant frequencies change from two points to one point depending on the length of the air gap. The double-resonance frequency region occurs at low impedance and short range. As the air-gap distance and impedance increase, one resonance region appears. The efficiency falls sharply at this operation range.

Author details

Ali Agcal, Selin Ozcira* and Nur Bekiroglu

*Address all correspondence to: selinozcira@gmail.com

Department of Electrical Engineering, Yildiz Technical University, Istanbul, Turkey

References

- [1] Sample A. P., Waters B. H., Wisdom S. T. and Smith J. R. Enabling seamless wireless power delivery in dynamic environments. Proc. IEEE. 2013;101(6):1343–1358. doi: 10.1109/JPROC.2013.2252453
- [2] Wei W., Narusue Y., Kawahara Y., Kobayashi N., Fukuda H. and Tsukagoshi T. Characteristic analysis on double side spiral resonator's thickness effect on transmis-

- sion efficiency for wireless power transmission. In: IEICE Tech. Committee Meeting; May 2012; Yokohama. IEICE; 2012. p. 1–5.
- [3] Chih-Jung C., Tah-Hsiung C., Chih-Lung L. and Zeui-Chown J. A study of loosely coupled coils for wireless power transfer. *IEEE Trans. Circ. Syst. II Express Briefs.* 2010;57(7):536–540. doi:10.1109/TCSII.2010.2048403
 - [4] Kim Y. H., Kang S. Y., Lee M. L., Yu B. G. and Zyung T. Optimization of wireless power transmission through resonant coupling. In: Power electronics electrical drives automation and motion (SPEEDAM), 2010 international symposium; Sep. 2010; Pisa, Italy. USA: IEEE; 2009. p. 1069–1073. doi:10.1109/SPEEDAM.2010.5544862
 - [5] Salasa R. A. and Pleite J. Accurate modeling of voltage and current waveforms with saturation and power losses in a ferrite core via two-dimensional finite elements and a circuit simulator. *J. Appl. Phys.* 2010;107(9):1–4.
 - [6] Swain A. K., Neath M. J., Madawala U. K. and Thrimawithana D. J. A dynamic multivariable state-space model for bidirectional inductive power transfer syst.. *IEEE. Trans. Power Electron.* 2012;27(11):4772–4778.doi:10.1109/TPEL.2012.2185712
 - [7] Zahid Z. U., Dalala Z. and Lai J. Small signal modelling of series-series compensated induction power transfer system. In: IEEE 29th Annual Applied Power Electronic Conference Expo; Mar. 2014; Fort Worth, USA: IEEE; 2014. p. 2847–2853. doi:10.1109/APEC.2014.6803708
 - [8] Neath M. J., Swain A. K., Madawala U. K., Thrimawithana D. J. and Vilathgamuwa D. M. Controller synthesis of a bidirectional inductive power interface for electric vehicles. In: IEEE third international conference on sustainable energy technologies (ICSET; Sept. 2012; Kathmandu, Nepal). USA: IEEE; 2012. p. 60–65. doi:10.1109/ICSET.2012.6357376
 - [9] Neath M. J., Swain A. K., Madawala U. K. and Thrimawithana D. J. An optimal PID controller for a bidirectional inductive power transfer system using multiobjective genetic algorithm. *IEEE. Trans. Power Electron.* 2014;29(3):1523–1531.
 - [10] Hao H., Covic G. A. and Boys J. T. An approximate dynamic model of LCL-T-based inductive power transfer power supplies. *IEEE Trans. Power Electron.* 2014;29(10): 5557–5567. doi:10.1109/TPEL.2013.2293138
 - [11] Swain A. K., Devarakonda S. and Madawala U. K. Modeling, sensitivity analysis, and controller synthesis of multipickup bidirectional inductive power transfer systems. *IEEE Trans. Ind. Inf.* 2014;10(2):1372–1380. doi:10.1109/TII.2014.2307159
 - [12] Li H., Wang K., Huang L., Chen W. and Yang X. Dynamic modeling based on coupled modes for wireless power transfer systems. *IEEE Trans. Power Electron.* 2015;30(11): 6245–6253. doi:10.1109/TPEL.2014.2376474
 - [13] Huang Z., Wong S. C. and Tse C. K. Design methodology of a series-series inductive power transfer system for electric vehicle battery charger application. In: Energy

- conversion congress and exposition (ECCE); Sep. 2014; Pittsburg, USA: IEEE; 2014. p. 1778–1782. doi:10.1109/ECCE.2014.6953633
- [14] Qu X., Han H., Wong S. C., Tse C. K. and Chen W. Hybrid IPT topologies with constant current or constant voltage output for battery charging applications. *IEEE Trans. Power Electron.* 2015;30(11):6329–6337. doi:10.1109/TPEL.2015.2396471
 - [15] Zahid Z. U., Dalala Z. M., Zheng C., Chen R., Faraci W. E., Lai J.S.J., Lisi G. and Anderson D. Modeling and control of series-series compensated inductive power transfer system. *IEEE J. Emerg Select Topics Power Electron.* 2015;3(1):111–123. doi:10.1109/JESTPE.2014.2327959
 - [16] Buja G., Bertoluzzo M. and Mude K. N. Design and experimentation of wpt charger for electric city car. *IEEE Trans. Ind. Electron.* 2015;62(12):7436–7447. doi:10.1109/TIE.2015.2455524.
 - [17] Fincan B. and Ustun O. Limits and Solutions of Wireless Energy Transfer Systems. In: 7 ELECO International Conference on Electrical and Electronics Engineering; Dec. 2012; Bursa, Turkey: 8 2012. p. 455–459.
 - [18] Agcal A., Bekiroglu N. and Ozcira S. Examination of efficiency based on air gap and characteristic impedance variations for magnetic resonance coupling wireless energy transfer. *J. Magn.* 2015;20(1):57–61. doi:10.4283/JMAG.2015.20.1.057.
 - [19] Imura T. and Hori Y. Maximizing air gap and efficiency of magnetic resonant coupling for wireless power transfer using equivalent circuit and neumann formula. *IEEE Trans. Ind. Electron.* 2011;58(10):4746–4752. doi:10.1109/TIE.2011.2112317

Innovative Wireless Power Receiver for Inductive Coupling and Magnetic Resonance Applications

Young-Jun Park, Hongjin Kim, Hyung-Gu Park and
Kang-Yoon Lee

Additional information is available at the end of the chapter

<http://dx.doi.org/10.5772/63341>

Abstract

This chapter presents a wireless power receiver for inductive coupling and magnetic resonance applications. The active rectifier with shared delay-locked loop (DLL) is proposed to achieve the high efficiency for different operation frequencies. In the DC–DC converter, the phase-locked loop is adopted for the constant switching frequency in the process, voltage, and temperature variation to solve the efficiency reduction problem, which results in the heat problem. An automatic mode switching between pulse width modulation and pulse frequency modulation is also adopted for the high efficiency over the wide output power. This chip is implemented using 0.18 μm BCD technology with an active area of 5.0 mm \times 3.5 mm. The maximum efficiency of the active rectifier is 92%, and the maximum efficiency of the DC–DC converter is 92% when the load current is 700 mA.

Keywords: wireless power receiver, high efficiency, active rectifier, DC–DC converter, inductive coupling, magnetic resonance

1. Introduction

In recent years, research on wireless charging system (WCS) has been actively carried out with the rapid development of smartphones and wearable devices. **Figure 1** shows the annual wireless power revenues by application. Since wireless charging techniques are applied not only for consumer electronics or mobile devices, but also for military applications and electric vehicles, the market is predicted to continue to keep expanding to over 11.8 billion dollars by 2020.

Especially, for recent technology such as Internet of Things (IoT), The WCS is essential since sensor and communication functions need to be embedded in a single chip and energy need to be supplied simultaneously, while the user is communicating with other objects.

The remainder of this chapter is organized as follows. In **Section 2**, the WCS is described. **Section 3** provides a description of building blocks including the active rectifier, DC–DC converter, successive approximation register (SAR) ADC, and low drop out (LDO) regulator. **Section 4** shows the experimental results from the implementation of a 0.18 μm BCD, and **Section 5** concludes the chapter.

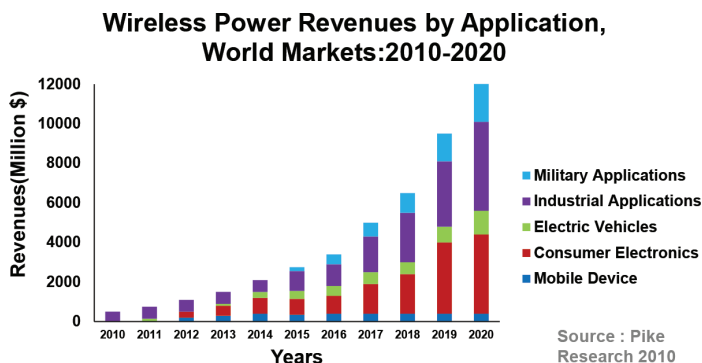


Figure 1. Annual wireless power revenues by application.

2. Wireless power receiver architecture

The WCS involves two major methods: inductive coupling and magnetic resonance. **Table 1** shows the characteristics of these two methods.

The inductive coupling method is used for distance <0.5 cm, and its transfer frequency ranges from 85 to 375 kHz. In-band communication is used for transmitting and receiving packets. This method applies to two standards: Wireless Power Consortium (WPC) and Power Matters Alliance (PMA). **Figure 2a** shows the conventional inductive coupling method WCS structure [1].

Method	Inductive coupling	Magnetic resonance
Power transfer distance	<0.5 cm	>1 cm
Power transfer frequency	85–357 kHz	6.78 MHz
Communication scheme	In-band communication	2.4 GHz BLE communication
Standard	WPC, PMA	A4WP

Table 1. Characteristics of inductive coupling method and magnetic resonance method.

The magnetic resonance method is used for distances over 1.0 cm, and its transfer frequency is 6.78 MHz ISM band. For the communication, 2.4 GHz Bluetooth Low Energy (BLE) communication is used, and the standard is Alliance for Wireless Power (A4WP). **Figure 2b** shows the conventional magnetic resonant method WCS structure [2]. The main differences between the two methods are the frequency and communication scheme, which means the two methods have different types of circuit implementations or issues.

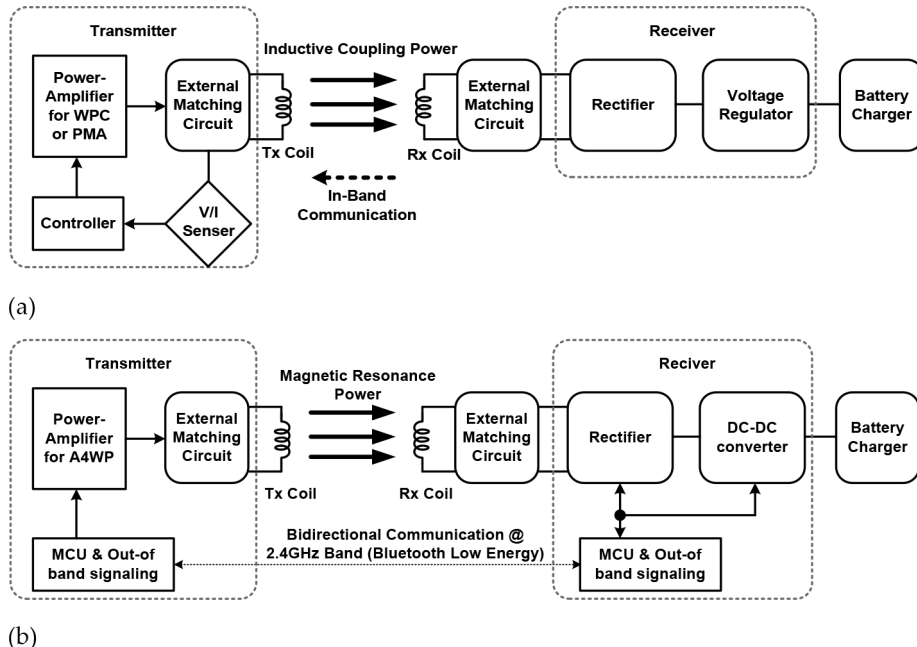


Figure 2. Conventional WCS (a) inductive coupling method (WPC, PMA), (b) magnetic resonance method (A4WP).

The issues of the two different charging methods are as follows. Compared to the inductive coupling method, the magnetic resonance method is a powerful WCS since it maintains high efficiency; even the distance between the transmitter and receiver is significantly more than several meters. However, since the frequency of the magnetic resonance method is 6.78 MHz, enhancing the efficiency of the rectifier (which accounts for the largest portion of the total efficiency of the receiver) is a very challenging task [2, 3].

The switching loss is relatively smaller for the inductive coupling method than that for the magnetic resonance method since its transfer frequency of 100–400 kHz is much lower than that of the magnetic resonance method. Although its charging distance is short, the inductive coupling method can achieve higher receiver efficiency. However, the on-resistance of the active rectifier and reverse leakage current should be minimized to enhance efficiency.

As explained above, the most important issue is the need to maintain high efficiency regardless of which charging method is used because heat from the chip caused by low efficiency will cause various problems. In WCSs, since the input power at the normal operation is above 5 W, the heat caused by the receiver inefficiency further reduces the efficiency of the receiver, which is a catch-22 situation [4, 5].

Figure 3 shows the detailed top block diagram of the receiver for the inductive coupling wireless battery charging system. The AC voltage at the Rx input is converted into a DC voltage by the rectifier. The power efficiency of the rectifier is very critical, as it provides the DC power supply to the following stages [6].

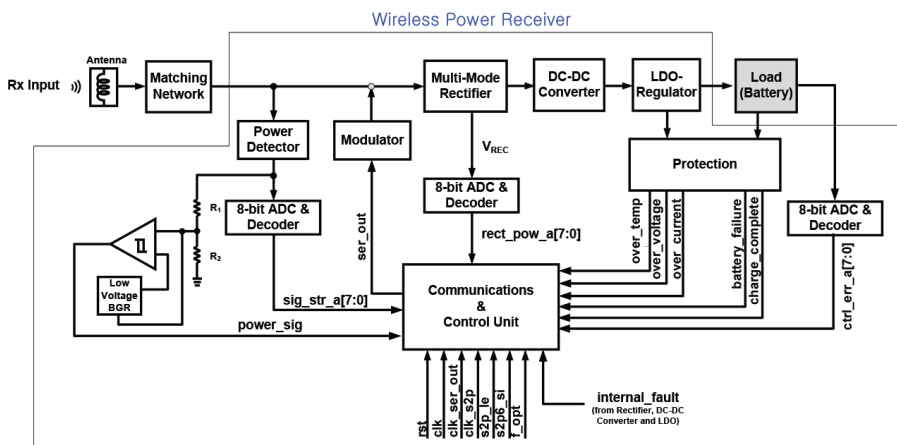


Figure 3. Top block diagram of the inductive coupling wireless power receiver [6].

The output of the multi-mode rectifier is converted into the desired DC voltage level through the DC-DC converter. LDO regulator generates the clean DC voltage required for the Battery. The power level of the input signal is measured at the power detector and converted into the digital code, $\text{sig_str_a}[7:0]$, by the 8-bit ADC and decoder. The DC output of the multi-mode rectifier, V_{REC} , is converted into the digital code, $\text{rect_pow_a}[7:0]$, by the 8-bit ADC and decoder. The communications and control unit receives various information from other blocks and configures the packet based on them [6].

Figure 4 shows the top block diagram of magnetic resonance wireless power receiver.

Power is transferred from the transmitter to the receiver through the coil and matching networks. The rectifier converts the AC voltage at the receiver input to DC voltage. The output of the rectifier is converted into the desired DC voltage level through the DC-DC converter [5].

The DC output of the rectifier, V_{RECT} , is converted into digital code, by the 10-bit SAR ADC. The output of the ADC is then transferred to the transmitter through the digital control block.

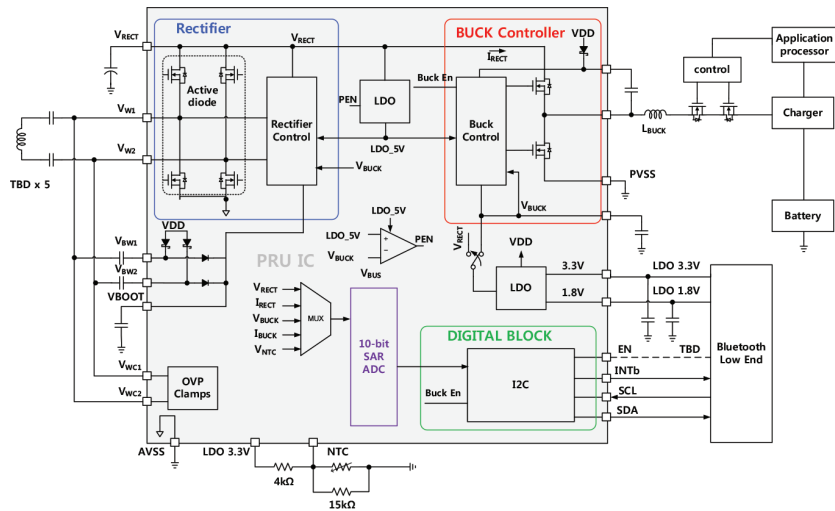


Figure 4. Top block diagram of the magnetic resonance wireless power receiver.

3. Building blocks of wireless power receiver

a. Active rectifier

Eq (1) defines the power conversion efficiency (PCE) of rectifier [7].

$$\begin{aligned}
 PCE &= \frac{V_{OUT}}{V_{IN}} \times \frac{I_{OUT}}{I_{IN}} \\
 &= \frac{V_{OUT}}{V_{OUT} + V_{LOSS}} \times \frac{I_{OUT}}{I_{IN} + I_{LOSS}}
 \end{aligned} \tag{1}$$

where V_{IN} , V_{OUT} , V_{LOSS} , I_{IN} , I_{OUT} , and I_{LOSS} are the amplitude of the input AC voltage, output DC voltage, voltage drop, input AC current, output DC current, and current loss of the rectifier, respectively.

Figure 5 shows the structure of a conventional passive full-wave rectifier. During the positive half cycle of the supply, diodes D₁ and D₂ conduct in series, while diodes D₃ and D₄ are reverse biased and the current flows through the load. Otherwise, during the negative half cycle of the supply, diodes D₃ and D₄ conduct in series, while diodes D₁ and D₂ are reverse biased. The current flowing through the load is the same direction as that for the positive half cycle of the supply. To generate a steady DC voltage, the load capacitor should be added to the output of the rectifier. The load capacitor converts the full-wave rippled output of the rectifier into a smooth constant DC output voltage.

The conventional rectifier using diodes has frequently been used in many applications since it is simple to implement. However, P-N junction diodes induce large forward voltage drops which directly lead to critical conduction loss. Although Schottky diodes have low dropout voltages, they also have a high leakage current and are not available in most standard CMOS/BCD processes.

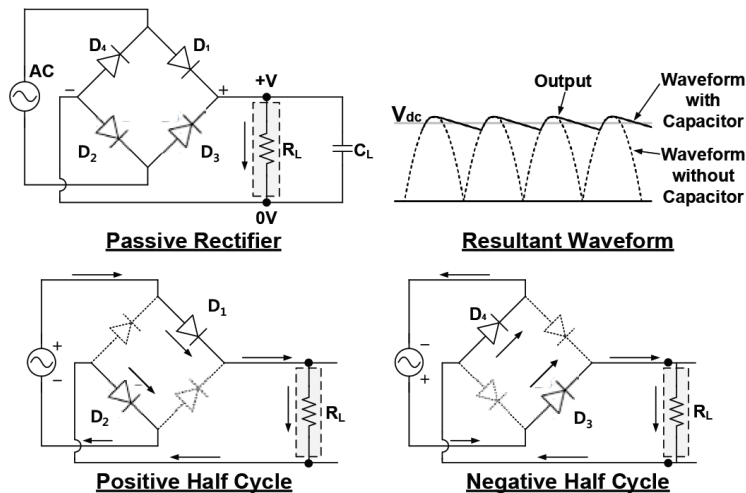


Figure 5. Conventional passive full-wave rectifier.

To address the issues explained above, a full-wave active rectifier which replaces diodes with MOSFETs should be designed. By implementing the active rectifier, voltage drop can be reduced to $2V_{DS}$, which is in the mV range when a single diode forward voltage drop is about 700 mV.

Figure 7a-c shows the active rectifier structures in prior works. **Figure 6a** shows the p-channel metal-oxide semiconductor (PMOS) diode connection structure with the bootstrap technique. This structure has the critical drawback of considerable conduction loss generated by the threshold voltage of 0.7 V from diode connection structure [8].

In the case of the comparator-based gate control structure shown in **Figure 6b**, the comparator is used to control a gate signal of active rectifier [8]. Since the delay caused by the comparator cannot be compensated in this structure, reverse leakage current occurs and efficiency is decreased. The structure in **Figure 6c** includes a zero delay circuit to compensate for the delay of the comparator [9]. The high-side MOSFET of this structure, however, consists of a PMOS cross-coupled structure, so that the size would be extremely large if the same on-resistance was used as that of an n-channel metal-oxide semiconductor (NMOS). As can be seen from the structures of **Figure 7a-c**, PMOS is used as high-side MOSFET. However, MOSFET involves a break issue since the maximum V_{SG} voltage of PMOS is designated as 5 V in the recent BCD process, which means that high voltage cannot be generated by the rectifier.

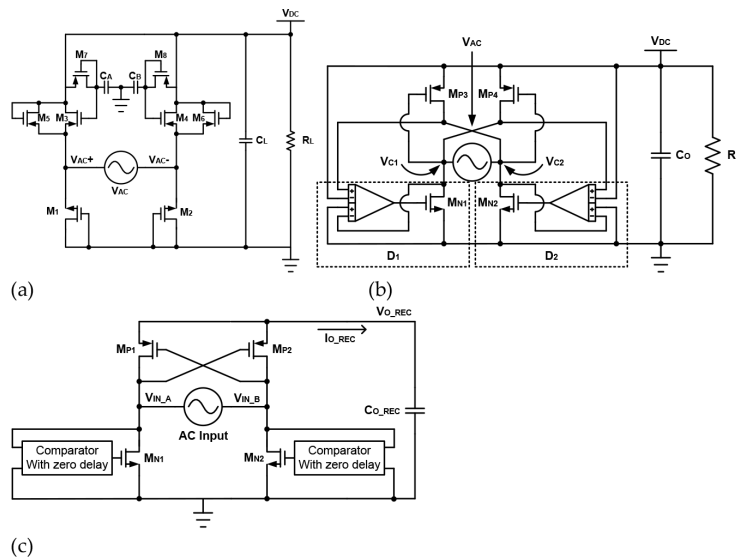


Figure 6. Active rectifier structures in prior works (a) PMOS diode connection structure [8], (b) comparator-based gate control structure [7], and (c) active rectifier with zero delay circuit [9].

A block diagram of the proposed active rectifier is illustrated in **Figure 7**. If a rectifier was implemented with passive diodes, the efficiency would be limited by the forward voltage drop of the passive diodes [5, 7, 10].

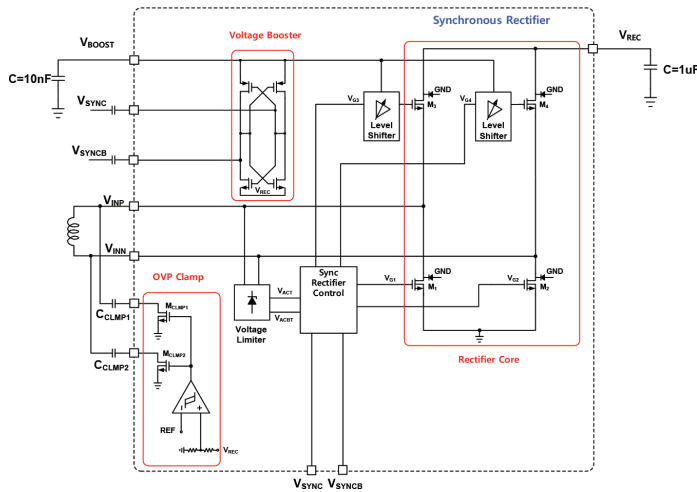


Figure 7. Block diagram of the proposed active rectifier.

In this work, the active rectifier is designed, where the MOS transistors are actively turned on and off depending on the polarity of the received AC input voltage. The voltage drop across the MOS transistors can be made to be significantly less than that of a diode-based passive rectifier, therefore achieving higher-power conversion efficiency [5].

Unlike passive diodes, however, the current flow through the MOS transistors is bidirectional, which means that the current can flow from the DC output to the AC input. This reverse leakage current severely degrades the power conversion efficiency (PCE) [9, 11, 12].

The frequency of the input power is 6.78 MHz for the A4WP standard. A propagation delay of the circuit generates reverse current; it then reduces the PCE. The frequency range of input power according to the WPC standard is from 85 to 205 kHz [1], while that according to the PMA standard is from 277 to 357 kHz [13].

Firstly, in the A4WP mode, DLL operates to maximize the efficiency while the adaptive zero current sensing (AZCS) circuit is off. The proposed active rectifier uses a shared DLL to compensate for the delay caused by the limiter, buffer, and level shifter. By compensating for the delay, the reverse leakage current can be removed while maximizing efficiency.

In the case of wireless charging standards such as WPC or PMA that specify hundreds of kHz frequencies, conduction loss is the most significant factor determining the total efficiency [1]. However, in the A4WP standard where the operating frequency is 6.78 MHz, the switching loss due to the high-voltage MOSFETs drastically increases. In order to reduce the conduction loss, MOSFETs should be designed to be as large as possible to minimize the on resistance [5].

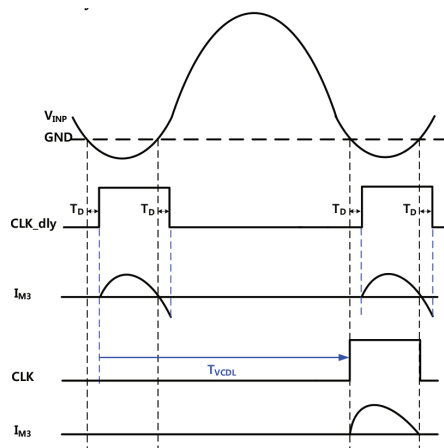


Figure 8. Timing diagram of the active rectifier with DLL.

Secondly, an AZCS is used to define the current path of the input current, I_{AC} . AZCS is only used in the WPC or PMA mode. The WPC and PMA modes do not have a constant frequency; the frequency is changeable. The active rectifier needs to operate switching according to the

input frequency. When the WPC or PMA mode is selected, the DLL circuit is turned off and only the voltage limiter, edge detector, and SR latch are operated.

The timing diagram of the active rectifier with the DLL is illustrated in **Figure 8**. As can be seen in **Figure 8**, the reverse leakage current is mainly due to the finite delay of the limiter, buffer, and level shifter that drive the power MOSFETs, which are large enough to minimize the voltage drop across them. The delayed turn-on of the power MOSFETs is not problematic because it does not cause any reverse leakage current. The delayed turn-off, however, results in reverse current flow which degrades the power conversion efficiency.

The measurement results of the WPR in A4WP mode for the output power of 6 W are shown in **Figure 9a**. The power efficiency of the WPR can be calculated using Eq (2) [5].

$$P_{IN} = \frac{V_{IN_PEAK} \times I_{IN_PEAK}}{2} \times \cos(\theta_V - \theta_I) \quad (2)$$

$$P_{\text{OUT}} = V_{\text{BUCK}} \times I_{\text{LOAD}} \quad (3)$$

$$\eta = \frac{P_{\text{OUT}}}{P_{\text{IN}}} \times 100 \quad (4)$$

In Eq (4), V_{IN_PEAK} , I_{IN_PEAK} , θ_V , θ_I , V_{BUCK} , and I_{LOAD} are the input peak voltage, input peak current, phase of input voltage, phase of input current, output voltage of buck DC-DC converter, and load current, respectively.

Figure 9b shows the measured power efficiency of the proposed active rectifier in A4WP mode. When the shared DLL function is used, the maximum efficiency of the active rectifier is 92% in A4WP mode.

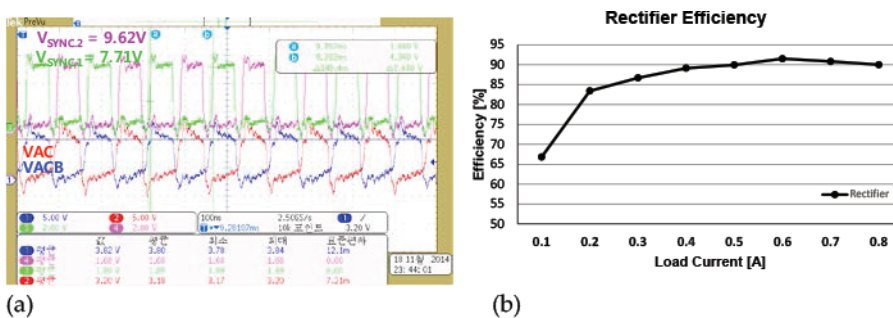


Figure 9. (a) Measured waveform (b) power efficiency of the active rectifier.

b. DC-DC converter

Figure 9 shows the structure of the conventional buck DC-DC converter.

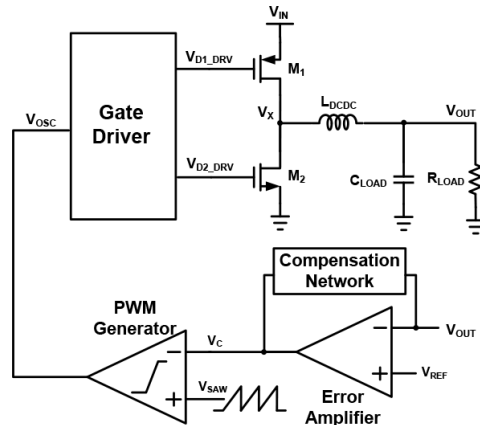


Figure 9. Block diagram of the conventional DC-DC converter.

M_1 energizes the inductor current, while M_2 de-energizes it. Therefore, both energized and de-energized inductor current flow to the load. The PWM generator activates the switch to regulate the outputs. The error amplifier and compensation network generate V_C voltage which is controlled by V_{OUT} voltage. The PWM generator determines the switching threshold by comparing V_{SAW} and V_C voltage. During this process, load current is changed by a feedback loop for DC output voltage [14].

There are several issues with the conventional DC-DC converter. First of all, the efficiency is reduced in the event of PVT variation since the switching frequency is varied. To solve this problem, phase-locked loop (PLL) is set to have a constant switching frequency regardless of PVT variation.

Secondly, the efficiency is reduced in light load condition. One of the drawbacks of the PWM method is a low efficiency in light load conditions. In the PWM method, switching loss is almost the same in the wide load current range because of the fixed switching frequency. In contrast to the PWM method, switching frequency in the PFM method changes in proportion to the load current. By changing the switching frequency, it is possible to reduce the switching loss at low load current conditions. By exploiting the two different methods, the proposed DC-DC converter adopts the PWM method in heavy load condition and adopts the PFM method in light load condition.

Figure 10 shows a block diagram of the proposed DC-DC converter.

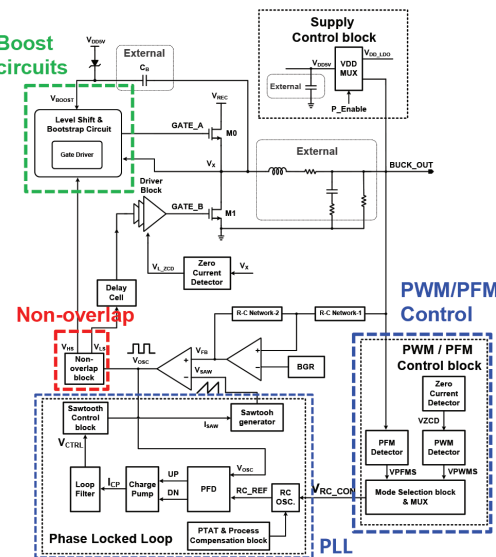


Figure 10. Block diagram of the proposed DC-DC converter.

The proposed DC-DC buck converter adopts a PLL to generate a constant frequency in spite of PVT variation and external circumstances [5].

Figure 11a shows the duty variation of the proposed DC-DC converter. As can be seen from the results, duty is varied by load current. When the load current is 700 mA, duty ratios of GATE_A and GATE_B are 335 ns (67%) and 160 ns (32%), respectively, also with about a 1% non-overlap period.

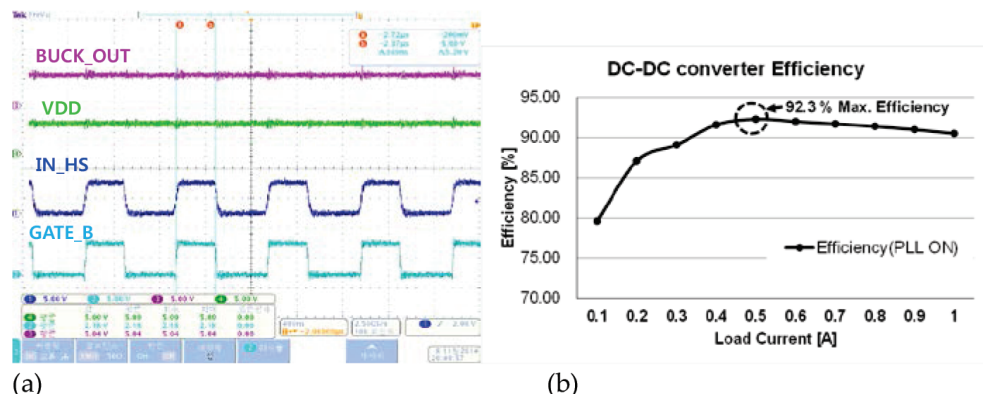


Figure 11. (a) Measured waveforms (b) measured efficiency of proposed DC-DC converter for load current of 700 mA.

Figure 11b shows the measured power efficiency of the proposed DC-DC converter. When the PLL function is used, the maximum efficiency of the DC-DC converter is 92% at the load current of 700 mA.

c. SAR ADC

Figure 12 shows the block diagram of conventional SAR ADC. In the conventional SAR ADC, the capacitance of capacitor digital-to-analog converter (CDAC) is changed and compared to the sampling value, using a binary searching mechanism to define the output code from the most significant bit(MSB) to the least significant bit(LSB).

The capacitor for CDAC should have $2^N C$ capacitance to satisfy the output resolution. This means that size becomes extremely large when designing high-resolution ADCs and the power consumption of the reference generator used as the charging and discharging capacitor increases as a result [15].

Since the proposed dual-sampling SAR ADC structure can be compared to the MSB signal through a sampling process, CDAC can be designed to have $2^{(N-1)} C$ capacitance.

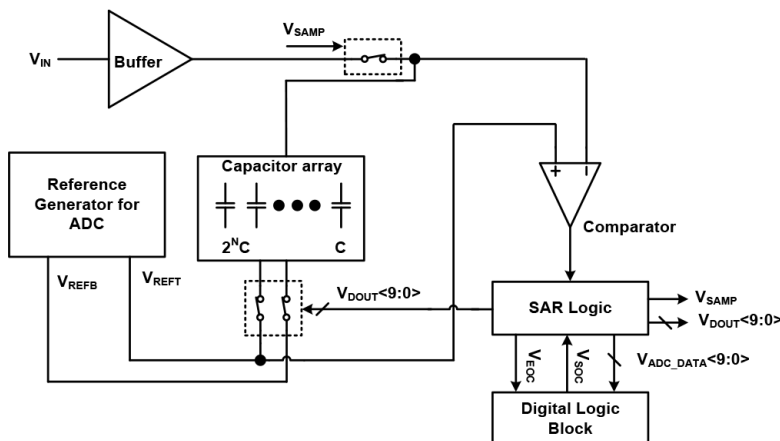


Figure 12. Block diagram of the conventional SAR ADC.

This means that the MSB capacitor can be reduced, and consequently, the size and power consumption can be reduced. Moreover, by adopting the adaptive power control (APC) technique for the comparator, power consumption can be reduced and overall system efficiency can be optimized.

A block diagram of the proposed SAR ADC is presented in **Figure 13** [5]. It consists of a simple analog block, including a DAC, comparator, reference voltage generator, and SAR.

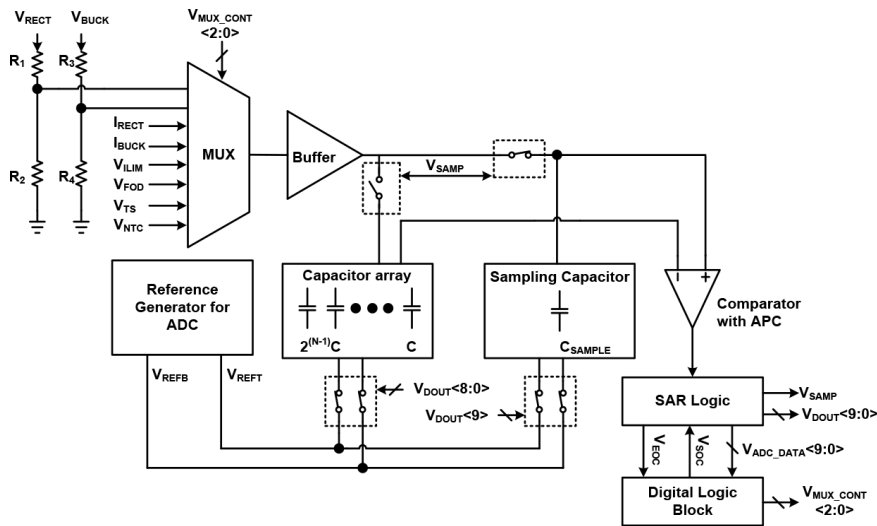


Figure 13. Block diagram of the proposed SAR ADC.

The proposed SAR ADC processes the voltage and current for the rectifier and DC-DC converter as well as information from the temperature sensing block through a MUX.

Figure 14 shows the timing diagram of the proposed SAR ADC.

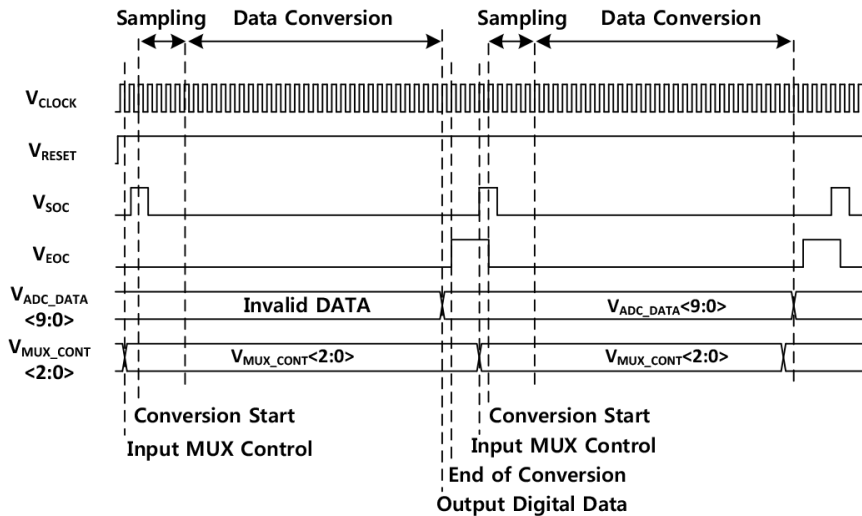


Figure 14. Timing diagram of the proposed SAR ADC.

In the MUX, the selection signal $V_{MUX_CONT}<2:0>$ was composed to save the data and processing during three cycles right after the EOC signal and then controlled by I^C [5].

d. LDO regulator

The input voltage range of conventional LDO regulators is decided by the rated voltage of the components. In general, the rate voltage of CMOS has a maximum of 5 V, so high output voltage from the rectifier cannot be processed. The proposed LDO regulator can operate at high voltage using laterally diffused mOS (LDMOS) as the power MOSFET and the input range of the LDO regulator is increased to a maximum of 20 V by using a high-voltage buffer for efficient driving. Moreover, a capacitor feedback circuit is proposed for power supply rejection ratio (PSRR) and fast settling.

Figure 15 shows a block diagram of the proposed LDO regulator. The output voltage drop due to rapid and large load variation could be minimized with a fast regulation loop.

Application of this fast transient LDO regulator is useful for low noise at wide input ranges and transient response (high voltage at rectifier input).

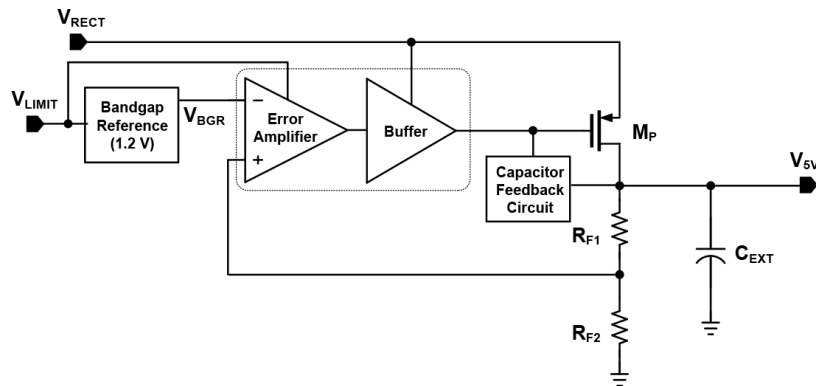


Figure 15. Block diagram of the LDO regulator.

In addition, the push-pull structure of the capacitor feedback circuit can provide a fast path for discharging and charging the gate of the pass transistor, which can respond to transient input with a buffer.

4. Experimental results

The chip was fabricated using the 0.18 μm BCD process with, a single poly layer, four layers of metal, MIM capacitors, and high sheet resistance poly-resistors. The chip microphotograph of the WPR is shown in **Figure 16**. The die area of the WPR is 5.0 mm \times 3.5 mm.

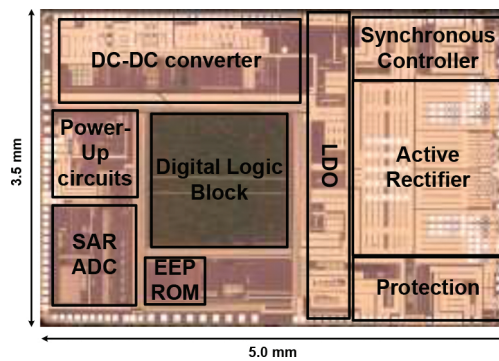


Figure 16. Chip microphotograph of the WPR.

Figure 17a shows the simulation results for the WPR in A4WP mode. Since the voltage for operation of the active rectifier is not generated at initial operation, the rectifier operates with the passive diode from the high-voltage MOSFET.

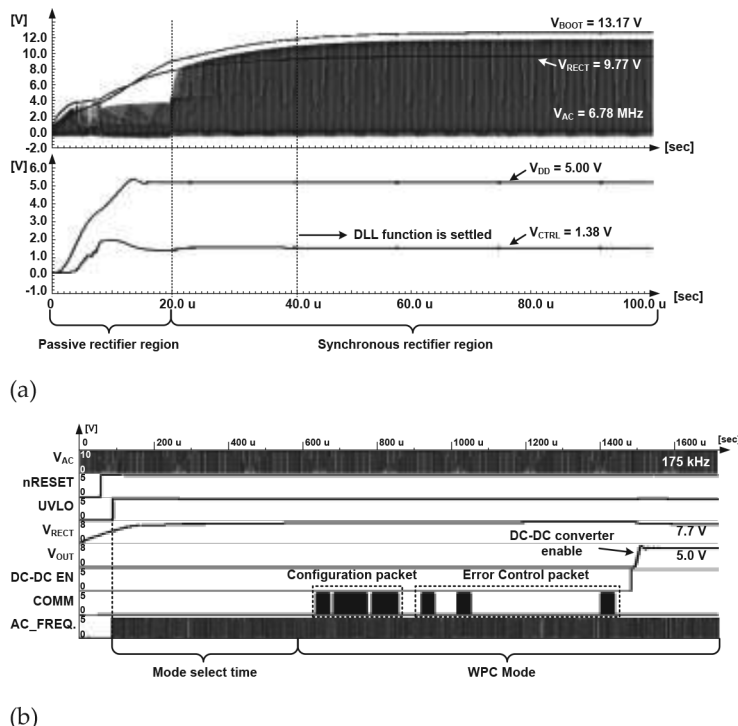


Figure 17. Simulation results of the active rectifier (a) A4WP mode (b)WPC mode.

When the output of the rectifier increases above 5.2 V, the active rectifier also begins to operate without any help from the passive diode [5].

As can be seen from the simulation results, with 7.5 W input and $13.83\ \Omega$ output load, a maximum power of 6.9 W and an efficiency of 92% were achieved at the maximum efficiency condition when DLL was locked.

Figure 17b shows the simulation waveform of WPR in WPC mode. WPR is supplied by VAC power, UVLO increases, detecting mode during mode select time. The frequency of VAC is 175 kHz, WPC mode is selected to send not only configuration packets but also error control packets.

The measurement board for the WPR is illustrated in **Figure 18a**. The Tx coil and Rx coil were located at the bottom and top sides, respectively. The power was transferred from the WPT board to the WPR board through the Tx and Rx antenna.

Figure 18b shows the measured system efficiency of the proposed WPR. The maximum system efficiencies are 84 and 86% in A4WP and WPC/PMA modes, respectively.

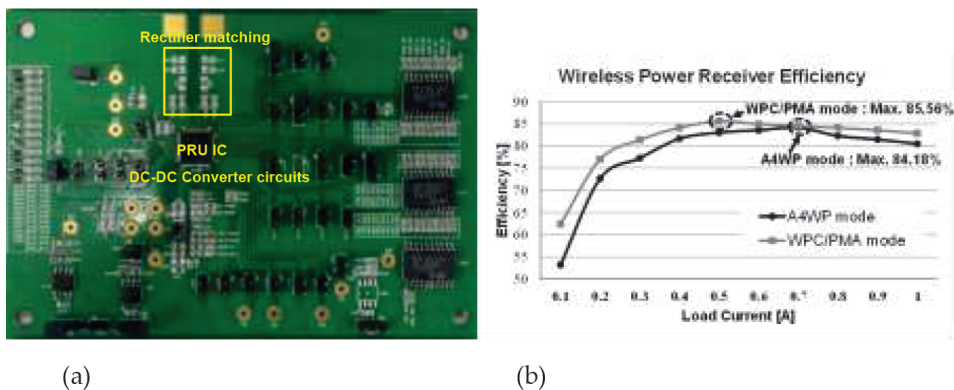


Figure 18. (a) Measurement board and (b) measured system efficiency of the WPR.

The comparison between the reported-related WPRs, and this work is summarized in **Table 2**. As can be seen from **Table 2**, the proposed WPR is the only chip that supports three different types of standards, namely A4WP, WPC, and PMA and shows the highest overall efficiency. Moreover, the results show that the proposed WPR has a wider input voltage range than the other references [2, 9, 16, 17], which is from 3 to 20 V.

5. Conclusion

This chapter presents a WPR for inductive coupling and magnetic resonance applications. Especially for the rectifier, which consumes the most significant portion of overall efficiency,

shared DLL and AZCS structures are proposed to improve the efficiency at different frequencies. In the DC–DC converter, PLL was adopted for a constant switching frequency during PVT variation to solve the efficiency reduction problem, especially due to heat.

References	[2]	[9]	[16]	[17]	This work
Technology	0.35 μm BCD	0.35 μm BCD	0.5 μm CMOS	0.18 μm CMOS	0.18 μm BCD
Supported standard	A4WP	A4WP	–	A4WP	A4WP, WPC/ PMA
Overall system efficiency (%)	86 (Off Chip Rectifier)	75/68	77 (rectifier only)	50	A4WP, 84 WPC/PMA, 86
Power transfer frequency (MHz)	6.78	3.23/6.78	13.56	6.78	6.78, 0.085–0.375
Input voltage range (V)	20	4–8	2.15–3.7	20	3–20
Maximum output power (W)	6	3	0.037	1	10.8
Output voltage (V)	5	5	3.1	3.1	5 or 9
Die area (mm^2)	5.52 (w/o rectifier)	18.3	0.585	6.25	17.5
Maximum output power/die area (W/ mm^2)	1.09 (w/o rectifier)	0.16	0.06	0.16	0.62

Table 2. Performance summary of the WPR.

This chip is implemented using 0.18 μm BCD technology with an active area of 5.0 mm \times 3.5 mm. The maximum efficiency of the active rectifier is 92%. The maximum efficiency of the DC–DC converter is 92% when the load current is 700 mA. Total system efficiency for the A4WP mode is a maximum 84% with 700 mA load current. Also, for the WPC/PMA mode, the maximum system efficiency is 86% with 500 mA load current.

In the future, the power conversion efficiency of the WPR needs to be improved since the maximum output power level is increasing more and more. The die area should be minimized for mobile applications at the same time.

Author details

Young-Jun Park, Hongjin Kim, Hyung-Gu Park and Kang-Yoon Lee*

*Address all correspondence to: klee@skku.edu

College of Information and Communication Engineering, Sungkyunkwan University, Suwon, South Korea

References

- [1] Wireless Power Consortium, "System Description Wireless Power Transfer", Volume I: Low Power, Part 1: Interface Definition Version 1.0, 2010.
- [2] Jun-Han Choi et al., "A Resonant Regulating Rectifier (3R) Operating at 6.78MHz for a 6 W Wireless Charger with 86% Efficiency", Solid-State Circuits Conference Digest of Technical Papers (ISSCC), pp. 64–65, 2013.
- [3] Ryota Shinoda et al., "Voltage-boosting wireless power delivery system with fast load tracker by $\Delta\Sigma$ -modulated sub-harmonic resonant switching", Solid-State Circuits Conference Digest of Technical Papers (ISSCC), pp. 288–290, 2012.
- [4] Ricky Tseng et al., "Introduction to the alliance for wireless power loosely-coupled wireless power transfer system specification version 1.0", Wireless Power Transfer (WPT), 2013 IEEE, pp. 79–83, 2013.
- [5] Hyung-Gu Park et al. "A Design of a Wireless Power Receiving Unit With a High-Efficiency 6.78-MHz Active Rectifier Using Shared DLLs for Magnetic-Resonant A4 WP Applications", IEEE Transactions on Power Electronics, Vol. 31, No. 6, pp. 4484–4498, 2016.
- [6] Yeon-Kug Moon et al., "Wide input range, high-efficiency magnetic resonant wireless power receiver," International Journal of Electronics, Vol. 102, No. 2, pp. 326–344, 2015.
- [7] Yat-Hei Lam et al., "Integrated Low-Loss CMOS Active Rectifier for Wirelessly Powered Devices", IEEE Transactions on Circuits and Systems II: Express Briefs, Vol. 53, No. 12, pp. 1378–1382, 2006.
- [8] Ji-Hun Kang et al., "A design of wide input range, high efficiency rectifier for mobile wireless charging receiver", Wireless Power Transfer Conference (WPTC), 2014 IEEE, pp. 154–157, 2014.
- [9] Young-Jin Moon et al., "A 3.0-W wireless power receiver circuit with 75-% overall efficiency", Solid State Circuits Conference (A-SSCC), 2012 IEEE Asian, pp. 97–100, 2012.
- [10] Yan Lu et al., "A 13.56 MHz CMOS Active Rectifier With Switched-Offset and Compensated Biasing for Biomedical Wireless Power Transfer Systems", IEEE Transactions on Biomedical Circuits and Systems, Vol. 8, No. 3, pp. 334–344, 2013.
- [11] Christian Peters et al., "A CMOS integrated voltage and power efficient AC/DC converter for energy harvesting applications", Journal of Micromechanics and Micro Engineering, Vol. 18, No. 10, 2008.
- [12] Song Guo et al., "An Efficiency-Enhanced CMOS Rectifier With Unbalanced-Biased Comparators for Transcutaneous-Powered High-Current Implants", IEEE Journal of Solid-State Circuits, Vol. 44, No. 6, pp. 1796–1804, 2009.

- [13] Siamak Bastami, "Magnetic Induction or Magnetic Resonance for Wireless Charging?" Bodo's Power systems, pp. 22–26, January 2013.
- [14] Wan-Rone Liou et al., "A High Efficiency Dual-Mode Buck Converter IC For Portable Applications", IEEE Transactions on Power Electronics, Vol. 23, No. 2, pp. 667–677, 2008.
- [15] Binhee Kim et al., "An energy-efficient dual sampling SAR ADC with reduced capacitive DAC", IEEE International Symposium on Circuits and Systems, 2009. ISCAS 2009, pp. 972–975, 2009.
- [16] Hyung-Min Lee et al., "An Adaptive Reconfigurable Active Voltage Doubler/Rectifier for Extended-Range Inductive Power Transmission", IEEE Transactions on Circuits and Systems II: Express Briefs, Vol. 59, No. 8, pp. 481–485, 2012.
- [17] Kazutoshi Tomita et al., "1-W 3.3–16.3-V Boosting Wireless Power Transfer Circuits With Vector Summing Power Controller", IEEE Journal of Solid-State Circuits, Vol. 47, No. 11, pp. 2576 – 2585, 2012.

Microwave Power Transmission Based on Retro-reflective Beamforming

Xin Wang and Mingyu Lu

Additional information is available at the end of the chapter

<http://dx.doi.org/10.5772/62855>

Abstract

Microwave power transmission has the potential to supply wireless power to portable/mobile electronic devices over long distances (on the order of meters or even kilometers) efficiently. Nevertheless, several technical challenges remain to be resolved in order to accomplish practical microwave power transmission systems, including (i) minimizing power loss due to microwave propagation, (ii) preventing humans and other electrical systems from exposure to excessive microwave radiation, and (iii) reconfiguring wireless power transmission in reaction to environmental changes (such as physical movements of portable devices) in real time. In this chapter, a microwave power transmission scheme based on retro-reflective beamforming is proposed to address the above challenges. In the retro-reflective beamforming, wireless power transmission is guided by pilot signals. To be specific, one or more than one mobile device(s) broadcast pilot signals to their surroundings, and based on analyzing the pilot signals, a wireless power transmitter delivers focused power beam(s) onto the mobile device(s). Preliminary numerical and experimental results are presented to demonstrate the feasibility of the proposed retro-reflective beamforming scheme.

Keywords: microwave power transmission, antenna array, retro-reflective beamforming, pilot signals, microwave power focusing

1. Introduction

Microwave power transmission has been actively pursued for more than 50 years as one of the possible technologies to deliver electrical power wirelessly [1–3]. The microwave power transmission technique employs propagating electromagnetic waves in the microwave frequency range as the carrier of wireless power. Compared with techniques based on induc-

tive coupling [4], microwave power transmission has the potential to reach longer distances (on the order of meters or even kilometers). Meanwhile, microwave power transmission enjoys several advantages relative to optical power transmission [5]. First, microwave has better penetration compatibility than optical waves. Second, the conversion efficiency between DC power and microwave power is usually higher than that between DC power and optical power. Third, microwave beams can be steered straightforwardly through the phase control, whereas beam steering without resorting to mechanical motion is much more difficult in the optical regime. In 1960s, Brown [6] successfully demonstrated supplying microwave power from a ground station to a helicopter, which is probably the first impactful demonstration of microwave power transmission in the history. Since 1970s, a range of research efforts are conducted on using microwave beam to deliver power from satellites to the earth, albeit to date its feasibility is still under evaluation [7]. A case study from 1997 to 2004 is reported in the studies of Lan Sun Luk [8] and Celeste et al. [9] to construct a point-to-point wireless electricity transmission to a small isolated village called Grand-Bassin in France. An antenna array was developed by the University of Colorado in 2008 to harvest 100 mW power from a transmitter 1 meter away [10]. In 2009, the feasibility of using a car-borne power broadcaster to power sensors installed over a bridge is studied in the work of Mascarenas et al. [11]. Today, many researchers are investigating taking advantage of microwave power transmission to eliminate/relieve the battery life bottleneck of mobile/portable electronic devices [12]. Despite of its long research history, several technical challenges remain to be resolved before microwave power transmission can be applied in practice, as elaborated below.

(i) Efficiency improvement

In microwave power transmission, power loss is mainly attributed to two factors: microwave-to-DC conversion and microwave propagation. With the development of novel rectennas, the microwave-to-DC conversion loss has been reduced to less than 20% [13, 14]. In order to improve the microwave propagation efficiency, beamforming (i.e., focusing electromagnetic fields in space) is the only effective means. Beamforming can be achieved straightforwardly using highly directive antennas when both the wireless power transmitter and wireless power receiver are stationary [8]; however, it is challenging when multiple mobile/portable devices residing in a large region need wireless power simultaneously. Traditional phased-array beamforming [15] does not constitute an ideal solution, since it fails when the line-of-sight path between the phased array and the target receiver is blocked by obstacles.

(ii) Safety assurance

Excessive microwave radiation may produce hazardous effects to human bodies as well as electrical devices. Thus, while wireless power is transmitted to target receivers, it is vital to ensure that humans and other electrical systems in the surroundings are not under intensive microwave illumination. As a matter of fact, a range of regulations have been established by various agencies for microwave radiation to safeguard human safety and electromagnetic compatibility [16–18].

(iii) Real-time reconfigurability

A practical microwave power transmission system must be capable of reconfiguring itself in reaction to the environmental changes (such as physical movements of portable devices) in real time, to maintain high efficiency and safety performance.

In order to address the above challenges, a retro-reflective beamforming scheme is proposed in this chapter. In the proposed scheme, one or more than one wireless power receiver(s) broadcast *pilot signals*, a wireless power transmitter receives the pilot signals, and based on analyzing the pilot signals, the wireless power transmitter constructs focused microwave beam(s) to deliver wireless power to the receiver(s). In other words, before transmitting wireless power, the wireless power transmitter plays the role of radar: it tracks the locations of mobile/portable receivers through analyzing pilot signals broadcasted by the receivers. Based on the outcome of radar tracking, the wireless power transmitter constructs spatially dedicated channels to deliver wireless power to the receivers, which minimizes the power loss associated with microwave propagation. As a radar, the wireless power transmitter is able to identify obstacles along the line-of-sight path toward the wireless power receivers such that it could avoid directly illuminating power beams onto humans or other objects. The proposed scheme is highly reconfigurable because wireless power transmission is guided by pilot signals. Specifically, wireless power is always focused onto the locations from which pilot signals stem. As a result, as long as the target receivers broadcast pilot signals periodically, wireless power beams would follow their motions dynamically. A range of numerical and experimental studies have been conducted to verify the feasibility of the proposed retro-reflective beamforming scheme [19–21]. The numerical and experimental results demonstrate that the proposed retro-reflective beamforming scheme is able to track mobile receivers' locations and focus wireless power onto the receivers' locations in real time.

2. Retro-reflective beamforming scheme and numerical modeling

The proposed retro-reflective beamforming scheme is illustrated in a typical indoor environment shown in **Figure 1**. The wireless power transmitter consists of a base station and multiple charging panels. The charging panels are mounted over the ceiling or walls. Each charging panel includes an array of planar antenna elements. The base station and charging panels are connected through cables. Mobile/portable devices in the room receive wireless power from the wireless power transmitter through the following two steps.

Step (1) One or more than one device(s) broadcast pilot signals.

Step (2) In response to the pilot signals, the charging panels jointly construct focused (that is, dedicated) microwave power beam(s) onto the target device(s).

When the mobile/portable devices are in motion, the microwave power beams would follow the devices' locations dynamically as long as the devices broadcast pilot signals periodically. A charging panel transmits power only if it has line-of-sight interaction with the target

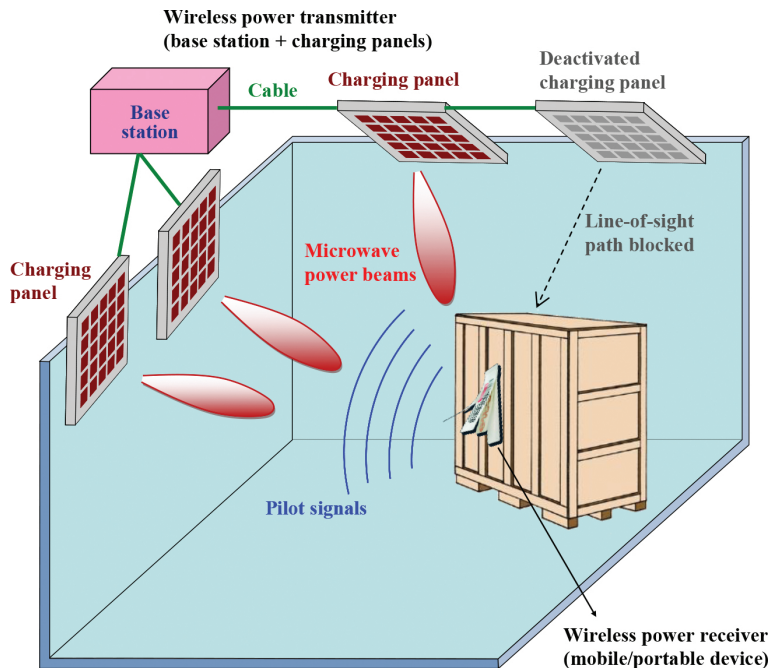


Figure 1. Depiction of wireless power transmission based on retro-reflective beamforming.

device(s); if the line-of-sight path is blocked by any obstacle, the charging panel is deactivated such that the obstacle, which might be human being, is not illuminated by power beams directly.

The underlying theory of retro-reflective beamforming is “time-reversal,” which takes advantage of channel reciprocity to accomplish a space-time matched filter [22]. Specifically, propagation of pilot signals follows the “channel from target devices to charging panels,” whereas propagation of microwave power beams follows the “channel from charging panels to target devices.” If these two channels are reciprocal to each other and if the microwave power transmission is tailored to be the retro-reflected version of pilot signals, microwave power is spatially focused onto the locations from which the pilot signals stem, that is, locations of the target devices. Furthermore, spatial focusing due to retro-reflection/time-reversal does not suffer from multipath environments [23–27].

The timing sequence of the retro-reflective beamforming scheme is depicted by a flow chart in **Figure 2**. Interactions between the wireless power transmitter and wireless power receiver are toggled among three modes: communication mode, radar mode, and charging mode. The process in **Figure 2** starts when a wireless power receiver (a mobile device, for instance) communicates a “charging request” signal to the wireless power transmitter. Once the wireless power transmitter acknowledges “charging request,” the system enters the radar mode in

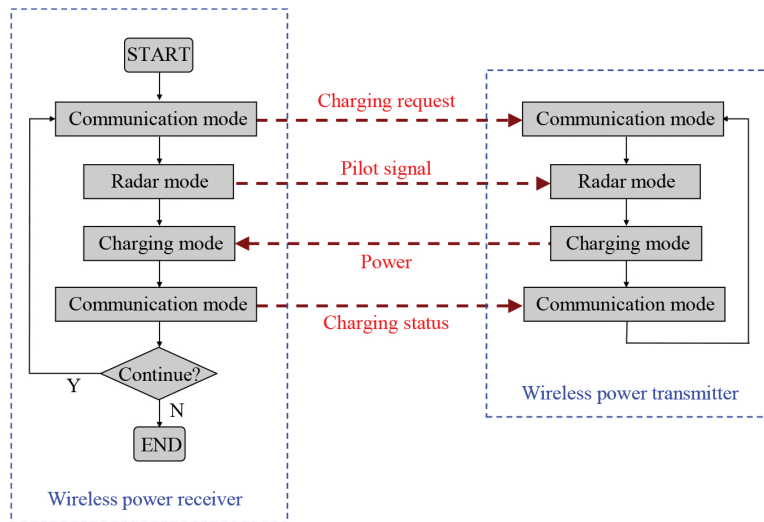


Figure 2. Timing sequence in the retro-reflective beamforming scheme.

which the wireless power receiver transmits pilot signal and the wireless power transmitter prepares for beamforming through analyzing the pilot signal. When the wireless power transmitter is ready, both the wireless power transmitter and wireless power receiver march into the charging mode and power is delivered to the receiver through spatially focused beams. In practice, the environment may change during the charging process; for example, the wireless power receiver may move and/or another wireless power receiver may request for charging. As a result, the beamforming plan must be adjusted accordingly. To accommodate these situations, the system is periodically switched from the charging mode to the communication mode and the radar mode such that the system would be reconfigured in reaction to the environmental changes.

A system block diagram of the retro-reflective beamforming scheme is plotted in **Figure 3**. The wireless power receiver is assumed to be a mobile/portable device, and thus, it is imperative to minimize its size, weight, and cost. To this end, the wireless power receiver only includes one antenna and two simple circuit blocks. The “pilot signal generator” block in the wireless power receiver is an impulse generator, which generates a periodic train of narrow impulses as the pilot signal. The other block in the wireless power receiver, “microwave-to-DC converter,” converts microwave power received from the wireless power transmitter to DC. The wireless power transmitter is composed of multiple antenna elements coordinated by a base station. Behind each antenna element, there are two circuit blocks: a “pilot signal analyzer” and a “microwave power generator.” The “pilot signal analyzer” analyzes the pilot signal received from the wireless power receiver, and the “microwave power generator” generates microwave power based on the outcome of analyzing pilot signal. Since the pilot signal is composed of an impulses train, its spectrum covers multiple discrete spectral lines. The

wireless power transmitter selects some of these discrete frequencies to analyze the pilot signal and transmit microwave power. At any discrete frequency, if the pilot signal has phase ϕ , microwave power is generated with phase $-\phi$; in other words, microwave power is configured to be the conjugate version of pilot signal because “phase conjugation in frequency domain” is equivalent to “reversal in time domain” [19].

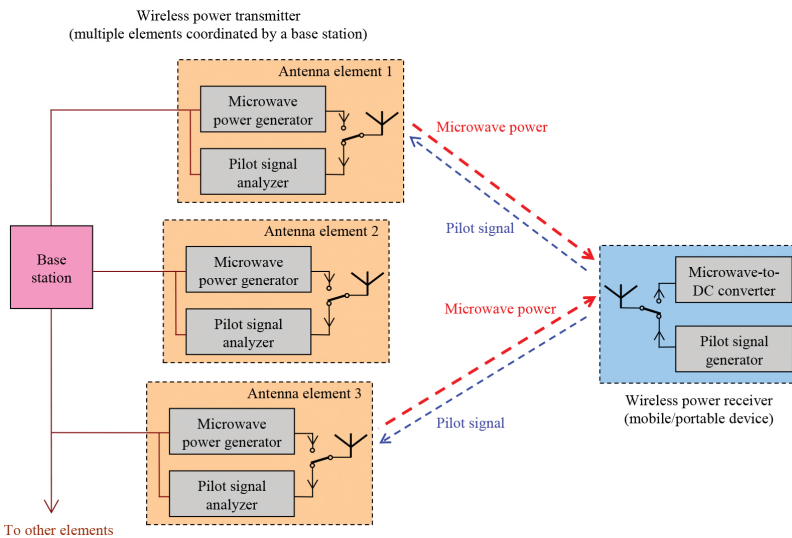


Figure 3. System block diagram of the retro-reflective beamforming scheme [20].

Employing narrow impulses as the pilot signal constitutes one of the major merits of the proposed retro-reflective beamforming scheme. In prior research efforts on retro-reflective beamforming, pilot signals are always generated by a microwave oscillator [28, 29]. Compared with microwave oscillators, impulse generators can be realized using relatively low-complexity and low-power circuitries [30] and hence is more suitable for mobile/portable devices. Because periodic impulses include information over multiple discrete frequencies, the wireless power transmitter has the flexibility of selecting multiple frequencies to transmit microwave power; in contrast, if the pilot signal is a continuous wave, the flexibility is limited to the pilot signal’s frequency and its high-order harmonics. Moreover, employing multiple frequencies to carry wireless power would result in better performance in spatial focusing, as demonstrated by some numerical results below.

Figures 4–6 show some numerical results for the retro-reflective beamforming scheme described above. The numerical model is illustrated in **Figure 4**. Eight charging panels are assumed to be deployed over a circular region with radius 3 m in the x - y plane. Each charging panel includes an antenna array with 5 by 5 elements equal spaced by 12 cm. Two devices reside in the region. The antennas over the charging panels and devices are all z -oriented dipoles. The devices transmit short impulses as pilot signals, which cover frequency band [4

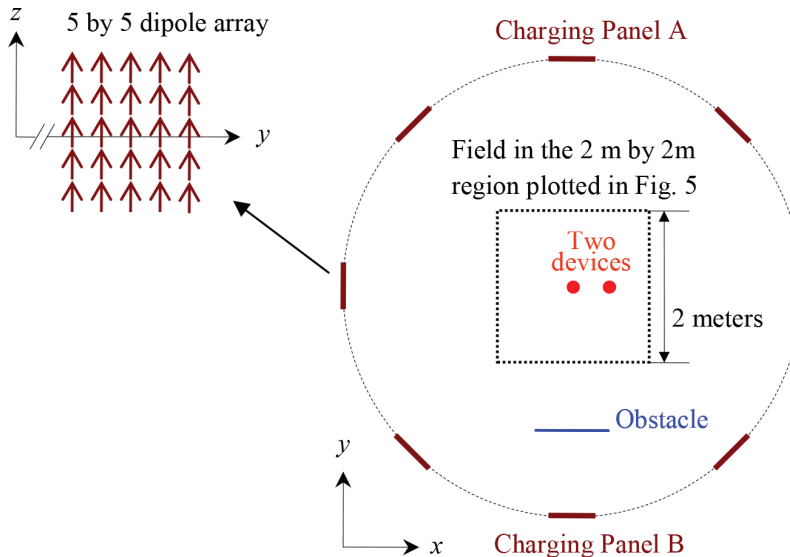


Figure 4. Numerical model of the retro-reflective beamforming scheme [19].

GHz, 6 GHz]. Charging power is allocated to N discrete frequencies in this band. To represent more realistic scenarios, a metallic plate with length 1 m and height 0.6 m is placed to block the line-of-sight path between the devices and one charging panel, which is Charging Panel B in **Figure 4**.

The model in **Figure 4** is simulated by a full-wave solver based on the Method of Moments [19]. Simulated E_z field distributions in a 2 m by 2 m region around the two devices are presented in **Figure 5**. When one device (the one at the center) sends pilot signals to the charging panels with the absence of obstacle, all the eight charging panels are active. If the charging panels only transmit power at one frequency 4.09 GHz (i.e., $N = 1$), the field distribution is shown in **Figure 5(a)**. Apparently, field is focused at many locations other than the device (the undesired focal points resemble side lobes of regular phased beamforming [31]). When N is chosen to be 30, only one focal point remains, which coincides with the device's location, as shown in **Figure 5(b)**. When both devices send pilot signals, the field is automatically focused onto the two devices (**Figure 5(c)**). In **Figure 5(d)**, the obstacle is assumed to be present, and Charging Panel B is blocked and turned off (the other seven charging panels are active). Field focusing does not rely on the obstacle's presence and the number of active charging panels, as shown in **Figure 5(d)**. With the presence of obstacle, which charging panels should be deactivated can be determined through analyzing the pilot signals. Two charging panels, Charging Panel A and Charging Panel B, are used as examples. After these two charging panels receive pilot signals from one device, phase differences between two local antenna elements are plotted in **Figure 6**; one of the two local elements is at the center and the other at the corner in the 5 by 5 array. As expected, since Charging Panel A has line-of-sight interaction with the device, its

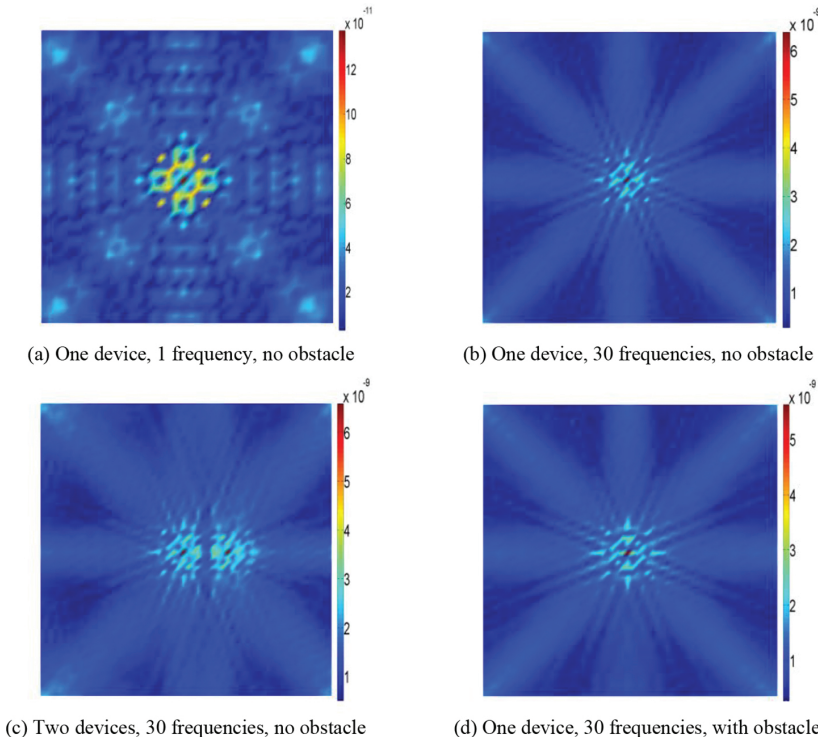


Figure 5. Simulated field distributions of the model in **Figure 4** (with $|E_z|$ represented by colors) [19]. (a) One device, 1 frequency, no obstacle. (b) One device, 30 frequencies, no obstacle. (c) Two devices, 30 frequencies, no obstacle. (d) One device, 30 frequencies, with obstacle

phase difference follows a straight line proportional to the frequency (corresponding to a time delay), whereas such a pattern does not appear at Charging Panel B.

3. Experimental verification of retro-reflective beamforming scheme

We have conducted a range of experimental studies to verify the retro-reflective beamforming scheme described in the previous section [20] [21]. Some of the experimental results are presented in this section.

One of the experimental setup is depicted in **Figure 7**. The wireless power transmitter includes one charging panel, which further includes four microstrip antenna elements. The wireless power receiver has one microstrip antenna. The power transmitter is stationary, whereas the wireless power receiver moves along the x axis in the experiments and it emulates a mobile/portable device. “ $x = 0$ ” denotes the location over the x axis right in front of the charging panel. The distance between “ $x = 0$ ” and the wireless power transmitter is 50 cm.

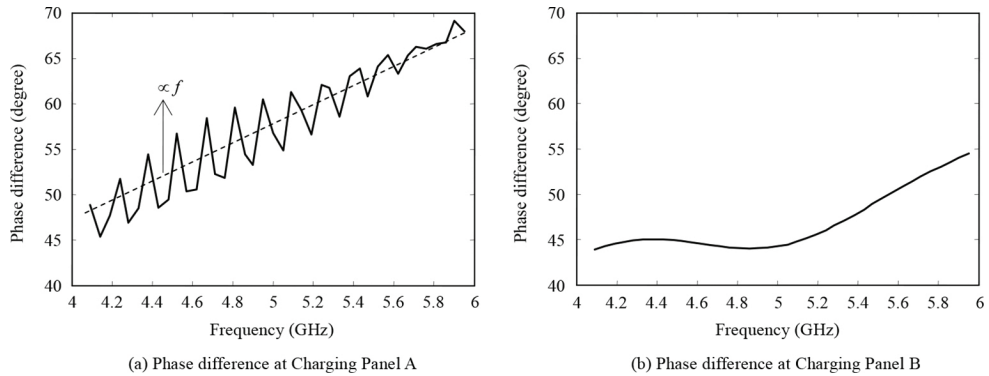


Figure 6. Numerical results of phase difference with the presence of obstacle [19]. (a) Phase difference at Charging Panel A. (b) Phase difference at Charging Panel B.

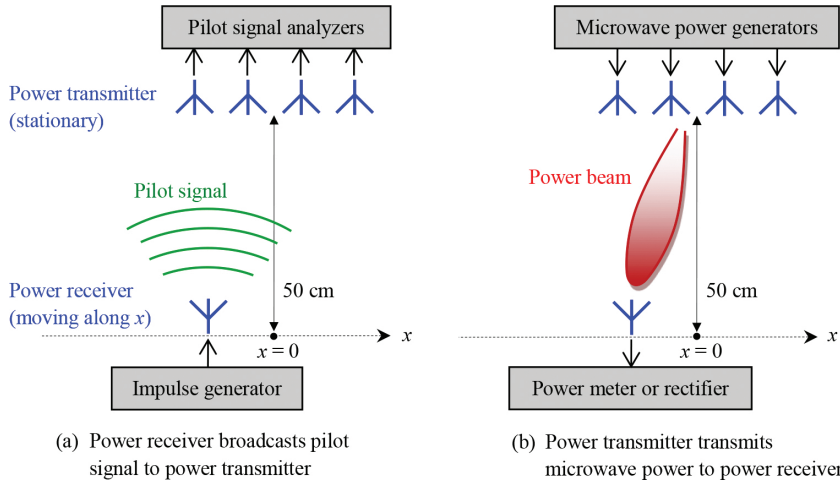


Figure 7. Depiction of an experimental setup with one charging panel [21]. (a) Power receiver broadcasts pilot signal to power transmitter. (b) Power transmitter transmits microwave power to power receiver.

The experimental procedure has the following two steps.

Step (1): Power receiver transmits pilot signal to power transmitter (**Figure 7(a)**). The power receiver's antenna is connected to an impulse generator. The impulses transmitted by the power receiver's antenna behave as the pilot signal. In our implementation, the impulses are generated through amplitude modulating a continuous wave at 2.08 GHz by periodic square impulses with a pulse width of 25 ns and a pulse repetition rate of 4 MHz (its waveform is illustrated in **Figure 8**). The pilot signal is received by the four antennas of the power transmitter and then analyzed by the “pilot signal analyzers.”

Step (2): Power transmitter transmits wireless power to power receiver (**Figure 7(b)**). In this step, the power transmitter's four antennas are fed by microwave power generators. The microwave power generators are configured according to the outcome of Step (1) so that a focused power beam is constructed toward the location from which the pilot signal is emitted. Wireless power collected by the power receiver's antenna is detected by either a power meter or a rectifier. The rectifier is implemented by following a voltage multiplier design in [32] and optimized around 2.1 GHz.

A photo of the experimental setup is shown in **Figure 9**: in Step (2), wireless power is delivered from the power transmitter to power receiver and wireless power reception is indicated by a light emitting diode (LED) on the power receiver.

The four antenna elements in the power transmitter are identical to one another. Each is a regular rectangular microstrip patch with dimensions 31.4 mm by 46 mm over FR4 substrate. The four antenna elements are equispaced with the distance between two adjacent elements 7

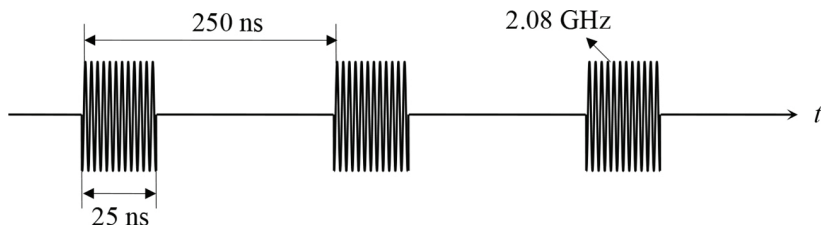


Figure 8. Illustration of the impulse pilot signal.

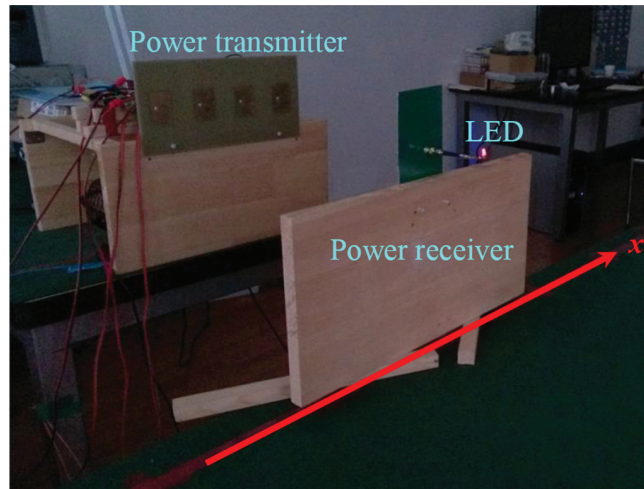


Figure 9. A photo of the experimental setup with one charging panel [21].

cm. Each antenna element's “−10 dB return loss frequency band” is roughly from 2.055 to 2.155 GHz. Each antenna element has a gain value of 3.8 dBi and half-power beamwidth of 136°. The microstrip antenna in the power receiver is the same as those in the power transmitter. All the antennas in **Figure 9** are linearly polarized, and the electric field is polarized along the x direction marked in **Figure 9**.

The two vital blocks in **Figure 7**, “pilot signal analyzers” and “microwave power generators,” are illustrated in **Figures 10** and **11**, respectively. In **Figure 10**, the pilot signals received by the four antennas are amplified by four low-noise amplifiers, down-converted through four mixers and a local oscillator at frequency f_{LO} , and then converted to the digital format by a four-channel analog-to-digital converter (ADC). The digital signals are stored within the memory of a personal computer and read by a signal processing program developed in the C++ language. The signal processing program calculates the phases of the four digital signals using short-time (20 μ s, to be specific) discrete Fourier transform at the frequency f_{IF} . With the calculated phases (denoted as ϕ_1 , ϕ_2 , ϕ_3 , and ϕ_4), a system control program operates a digital-to-analog converter (DAC), which provides four DC bias voltages (denoted as V_1 , V_2 , V_3 , and V_4) to control the phase shifters in **Figure 11**. The DAC also outputs a control signal V_{CTRL} that is used to turn on/off the oscillator in the microwave power generators. In **Figure 11**, a continuous wave generated by an oscillator at frequency f_i is split into four channels first; next, each channel goes through a phase shifter and power amplification before reaching the antenna. The retro-reflective beamforming is achieved by properly controlling the state of the four phase shifters so that the transmitting array is fed with phases $-\phi_1$, $-\phi_2$, $-\phi_3$, and $-\phi_4$, respectively. This is done by the system control program that determines the output DC bias voltages of the DAC based on the characteristics of the four phase shifters. The system control program is also responsible for controlling the operation sequence of the entire system. Specifically, in Step (1) of the experiment, the system control program activates the ADC and calls the signal processing program to analyze the pilot signal. In the meantime, the oscillator in the microwave power generators is turned off by the control signal V_{CTRL} to avoid the interference of microwave power to the pilot signal analyzers. In Step (2), the system control program deactivates the ADC and reset V_{CTRL} to turn on the oscillator so that the wireless power is transmitted.

The pilot signal analyzers and microwave power generators are implemented using commercial off-the-shelf components with model numbers listed in **Figures 10** and **11**. The mixers, amplifiers, and the oscillators are made by Analog Devices Inc. The four phase shifters are made by Beijing Tianhua Zhongwei Technology. The 1:4 power splitters are made by Mini-Circuits. The ADC and DAC are made by Beijing Art Technology Development Co. The ADC PCI8502 provides four synchronized channels with a sampling rate of 40 MHz and 12-bit resolution. The DAC PCI8250 provides eight synchronized channels with 16-bit resolution.

Employing impulses as the pilot signal leads to the flexibility of configuring f_i . The pilot signal's spectrum is centered at 2.08 GHz and contains discrete spectral lines with separation of 4 MHz. In one of the implementations, $f_i = 2.08$ GHz with $f_{LO} = 2.079$ GHz and $f_{IF} = 1$ MHz. f_i can be reconfigured to other frequencies straightforwardly; for instance in another implementation, f_i is reconfigured to be 2.108 GHz with $f_{LO} = 2.1$ GHz and $f_{IF} = 8$ MHz.

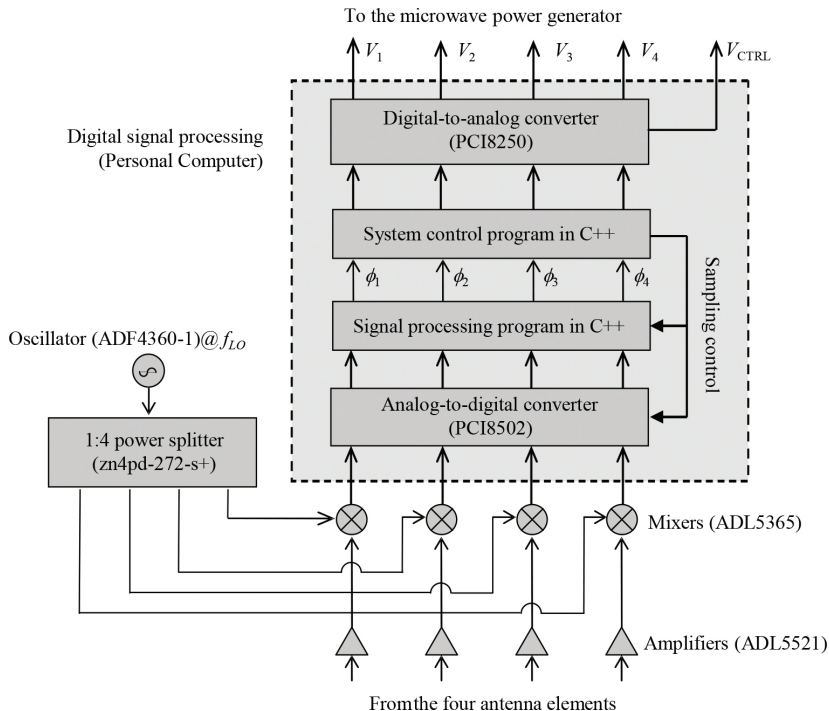


Figure 10. Block diagram of “pilot signal analyzers.”

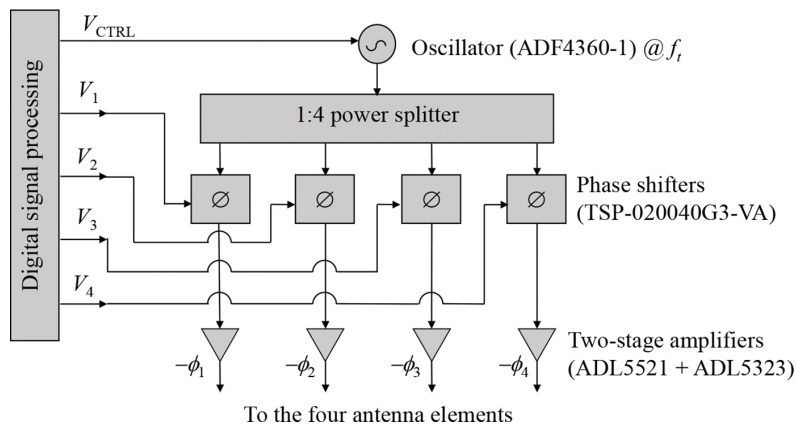


Figure 11. Block diagram of “microwave power generators.”

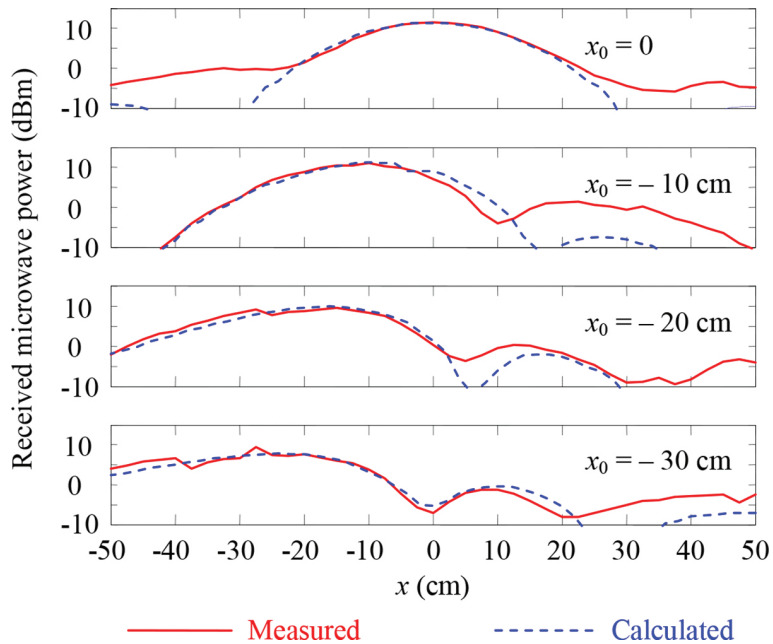


Figure 12. Received microwave power at frequency 2.08GHz [21].

In the experiments, a pilot signal is broadcasted by the power receiver at a location denoted as x_0 , and the pilot signal is received and analyzed by the power transmitter; then after the power transmitter is configured by analyzing the pilot signal, the power receiver moves along x axis to detect the wireless power. In all the experiments, the total power transmitted by the power transmitter is roughly 1 Watt (that is, 250 mW from each of its four antennas).

In **Figure 12**, microwave power measured by a power meter is plotted when $f_t = 2.08$ GHz. The four subplots in **Figure 12** correspond to “ $x_0 = 0$,” “ $x_0 = -10$ cm,” “ $x_0 = -20$ cm,” and “ $x_0 = -30$ cm,” respectively. The calculated curves in **Figure 12** are obtained using the Friis transmission equation [31]

$$P_r = P_t \left(\frac{\lambda}{4\pi d} \right)^2 G_t G_r$$

When $x_0 = 0$ and $x = 0$, the transmitted power $P_t = 1$ Watt, wavelength $\lambda = c/f_t$, c is the speed of light in free space, the transmitter-receiver distance $d = 50$ cm, the transmitting antenna's gain $G_t = 9.8$ dBi, the receiving antenna's gain $G_r = 3.8$ dBi, and the received power P_r is calculated to be 12 mW. In **Figure 12**, the measured data and calculated data generally match each other.

The measured data in reaction to “ $x_0 = 0$ ” have a peak at “ $x = 0$,” with peak value of the received power about 14 mW. The measured value (14 mW) is slightly larger than the calculated value (12 mW); we believe it is because the power receiver does not reside in the power transmitter’s far-zone, which makes Friis equation not very precise. When x_0 changes to -10 , -20 , and -30 cm, the power beam is steered and the beam center tracks x_0 . In our experiments, the beam cannot be steered beyond -30 cm due to the limitation of individual microstrip antennas’ radiation patterns. When x_0 takes positive values, the power beam is steered and the beam center tracks x_0 as well; beam steering for positive x_0 values is not demonstrated because it is symmetric to the negative x_0 values. Similar sets of results are displayed in **Figure 13**, after the power meter is replaced by the rectifier. The vertical axis in **Figure 13** represents the DC voltage measured over a $1.8\text{-k}\Omega$ load resistor in the rectifier. Beams in reaction to four x_0 values are clearly shown. When $x_0 = 0$, the peak voltage 3.5 V corresponds to $(3.5)^2/(1.8\text{ k}) \approx 7\text{ mW}$.

After f_t is reconfigured to 2.108 GHz , curves similar to those in **Figure 12** are plotted in **Figure 14**. The beamforming phenomena exhibited in **Figure 14** are basically the same as those in **Figure 12**.

On the basis of the experimental setup in **Figure 7**, another set of experiments are carried out as illustrated in **Figure 15**. As a progress with respect to **Figure 7**, the wireless power transmitter in **Figure 15** includes two charging panels, each consisting of four antenna elements. The two charging panels are placed over x axis and y axis, respectively. The wireless power receiver moves within a certain region in the x - y plane. **Figure 16** shows a photo of the

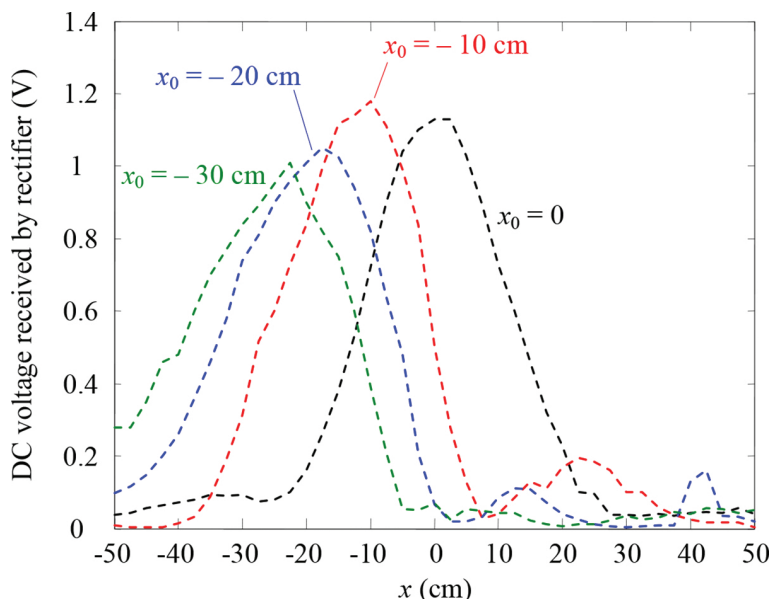


Figure 13. Received DC voltage at frequency 2.08GHz [21].

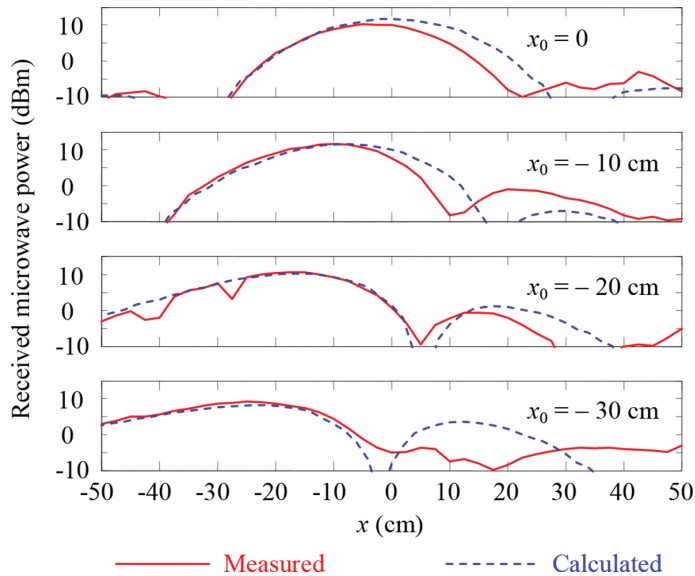


Figure 14. Received microwave power at frequency 2.108 GHz [21].

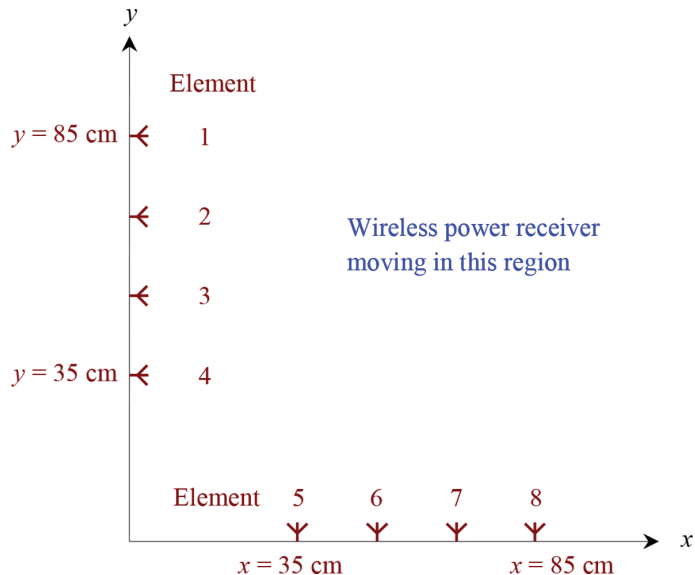


Figure 15. Illustration of an experimental setup with two charging panels [20].

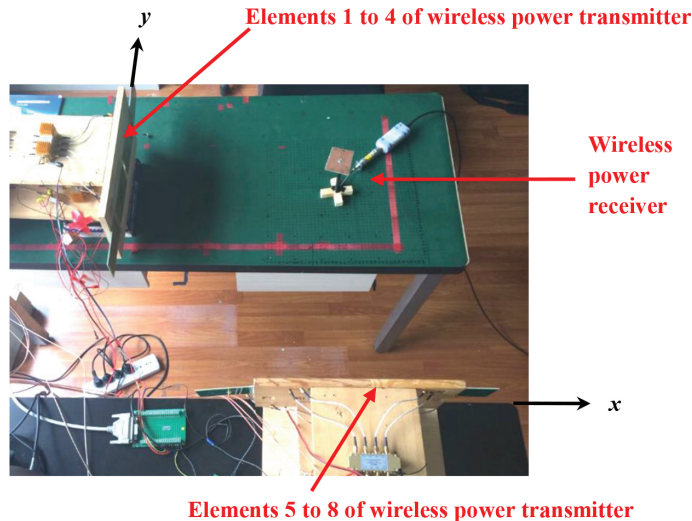


Figure 16. A photo of the experimental setup with two charging panels [20].

experimental setup corresponding to **Figure 15**. The antennas of the wireless power transmitter are microstrip antennas polarized along z direction; the antenna of the receiver is a monopole antenna, with omni-directional radiation pattern in the x - y plane.

Some results measured with the configuration in **Figures 15** and **16** are shown in **Figure 17**. The microwave power transmitted by each antenna element of the wireless power transmitter is roughly 175 mW, with a total of $175 \text{ mW} \times 8 = 1.4 \text{ Watt}$. A power meter is connected to the wireless power receiver's antenna, and the measured microwave power is plotted in **Figure 17**. The two plots in **Figure 17(a)** and **(b)** are obtained when the pilot signal is broadcasted from $(x = 60 \text{ cm}, y = 60 \text{ cm})$ and $(x = 70 \text{ cm}, y = 70 \text{ cm})$, respectively. **Figure 17** clearly demonstrates that the microwave power is focused onto the location from which the pilot signal is broadcasted as a result of retro-reflective beamforming.

4. Conclusion

This chapter presents a retro-reflective beamforming scheme aiming to supply microwave power to portable/mobile electronic devices over long distances (several meters or longer) efficiently. The preliminary numerical and experimental results demonstrate that the proposed retro-reflective beamforming scheme is capable of focusing microwave power onto target devices' locations through analyzing pilot signals broadcasted by the target devices. We are currently conducting research to verify the retro-reflective beamforming scheme more comprehensively.

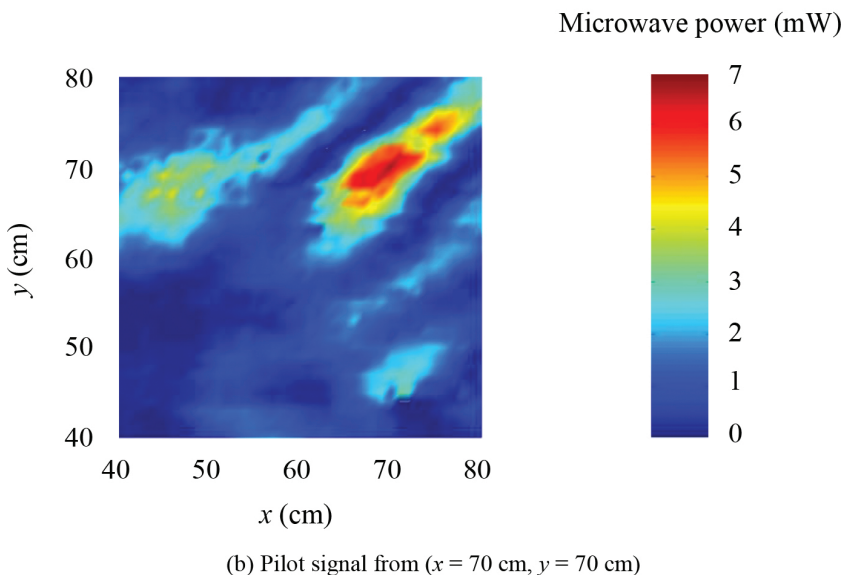
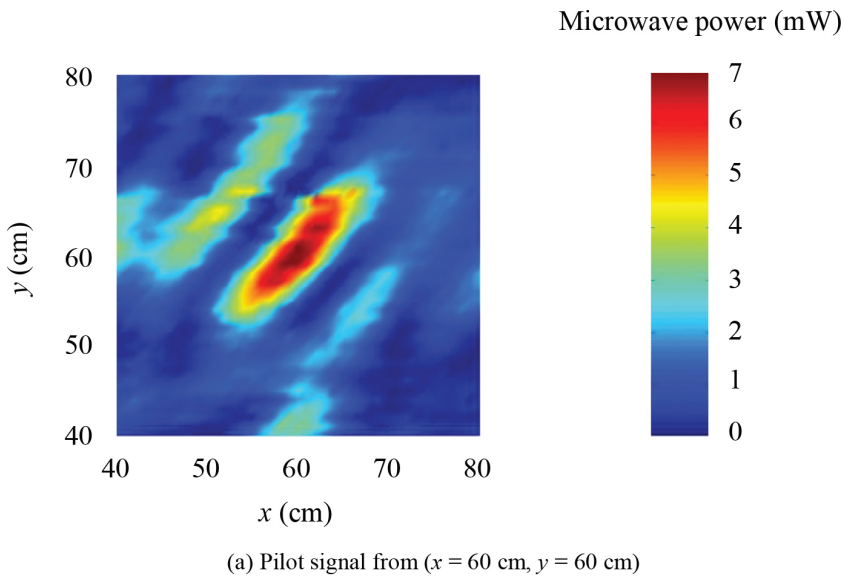


Figure 17. Microwave power distribution measured with the configuration in Figures 15 and 16 [20]. (a) Pilot signal from $(x = 60 \text{ cm}, y = 60 \text{ cm})$. (b) Pilot signal from $(x = 70 \text{ cm}, y = 70 \text{ cm})$.

Acknowledgements

This work was supported in part by National Science Foundation Grant ECCS 1303142, National Science Foundation Grant ECCS 1503600, and National Natural Science Foundation of China Grant 61471195

Author details

Xin Wang^{1*} and Mingyu Lu^{2*}

*Address all correspondence to: wang90@nuaa.edu.cn and mingyu.lu@mail.wvu.edu

1 College of Electronic and Information Engineering, Nanjing University of Aeronautics and Astronautics, Nanjing, China

2 Department of Electrical and Computer Engineering, West Virginia University Institute of Technology, Montgomery, WV, USA

References

- [1] Brown WC. The history of power transmission by radio waves. *Microwave Theory and Techniques, IEEE Transactions on.* 1984;32(9):1230–42.
- [2] Lee TH. *Planar microwave engineering: A practical guide to theory, measurement, and circuits.* Cambridge University Press; Cambridge, UK; New York, 2004.
- [3] Strassner B, Chang K. Microwave power transmission: Historical milestones and system components. *Proceedings of the IEEE.* 2013; 101(6):1379–96.
- [4] Garnica J, Chinga RA, Lin J. Wireless power transmission: From far field to near field. *Proceedings of the IEEE.* 2013; 101(6):1321–31.
- [5] Kim SM, Kim SM. Wireless optical energy transmission using optical beamforming. *Optical Engineering.* 2013; 52(4):043205.
- [6] Brown WC. Experimental airborne microwave supported platform. Spencer Lab Report, Raytheon CO: Burlington MA; 1965.
- [7] Dickinson RM. Safety issues in SPS wireless power transmission. *Space Policy.* 2000;16(2):117–22.

- [8] Lan Sun Luk JD, Celeste A, Romanacce P, ChaneKuang Sang L, Gatina JC. Point-to-point wireless power transportation in Reunion Island. In 48th International Astronautical Congress, Turin, Italy, October 1997.
- [9] Celeste A, Jeanty P, Pignolet G. Case study in Reunion Island. *Acta Astronautica*. 2004;54(4):253–8.
- [10] Zhao X, Qian T, Popovic Z, Zane R, Mei G. Wireless ultrasonic transducer network for structural health monitoring of an aircraft wing. In 17th World Conference on Non-destructive Testing. Shanghai, China, October 2008, pp. 1–8.
- [11] Mascarenas DL, Flynn EB, Todd MD, Overly TG, Farinholt KM, Park G, Farrar CR. Experimental studies of using wireless energy transmission for powering embedded sensor nodes. *Journal of Sound and Vibration*. 2010;329(12):2421–33.
- [12] Visser HJ, Vullers RJM. RF energy harvesting and transport for wireless sensor network applications: Principles and requirements. *Proceedings of the IEEE*. 2013; 101(6):1410–23.
- [13] McSpadden JO, Fan L, Chang K. Design and experiments of a high-conversion-efficiency 5.8-GHz rectenna. *Microwave Theory and Techniques, IEEE Transactions on*. 1998;46(12):2053–60.
- [14] Ren YJ, Chang K. 5.8-GHz circularly polarized dual-diode rectenna and rectenna array for microwave power transmission. *Microwave Theory and Techniques, IEEE Transactions on*. 2006;54(4):1495–502.
- [15] Landis GA, inventor; Nasa Glenn Research Center, Assignee. Charging of devices by microwave power beaming. United States patent US 6,967,462. 2005.
- [16] IEEE C95.1-2005: IEEE standard for safety levels with respect to human exposure to radio frequency electromagnetic fields, 3 kHz to 300 GHz. IEEE. 2006.
- [17] Rules & Regulations for Title 47, Federal Communications Commission. <https://www.fcc.gov/general/rules-regulations-title-47>.
- [18] ICNIRP (International Commission for Non-Ionizing Radiation Protection) Standing Committee on Epidemiology. Epidemiology of health effects of radiofrequency exposure. *Environmental Health Perspectives*. 2004;112(17):1741–54.
- [19] Zhai H, Pan HK, Lu M. A practical wireless charging system based on ultra-wideband retro-reflective beamforming. In *Antennas and Propagation Society International Symposium*, IEEE. Toronto, Ontario, July 2010.
- [20] He J, Wang X, Guo L, Shen S, Lu M. A distributed retro-reflective beamformer for wireless power transmission. *Microwave and Optical Technology Letters*. 2015;57(8):1873–6.

- [21] Wang X, Sha S, He J, Guo L, Lu M. Wireless power delivery to low-power mobile devices based on retro-reflective beamforming. *Antennas and Wireless Propagation Letters, IEEE*. 2014;13:919–22.
- [22] Henty BE, Stancil DD. Multipath-enabled super-resolution for RF and microwave communication using phase-conjugate arrays. *Physical Review Letters*. 2004;93(24):243904.
- [23] Fink M. Time reversal of ultrasonic fields. I. Basic principles. *Ultrasonics, Ferroelectrics, and Frequency Control, IEEE Transactions on*. 1992;39(5):555–66.
- [24] Wu F, Thomas JL, Fink M. Time reversal of ultrasonic fields. II. Experimental results. *Ultrasonics, Ferroelectrics, and Frequency Control, IEEE Transactions on*. 1992;39(5):567–78.
- [25] Fannjiang A, Solna K. Superresolution and duality for time-reversal of waves in random media. *Physics Letters A*. 2005;342(1):22–9.
- [26] Lerosey G, De Rosny J, Tourin A, Fink M. Focusing beyond the diffraction limit with far-field time reversal. *Science*. 2007;315(5815):1120–2.
- [27] De Rosny J, Fink M. Focusing properties of near-field time reversal. *Physical Review A*. 2007;76(6):065801.
- [28] Chang Y, Fetterman HR, Newberg IL, Panaretos SK. Microwave phase conjugation using antenna arrays. *Microwave Theory and Techniques, IEEE Transactions on*. 1998;46(11):1910–9.
- [29] Chiu L, Yum TY, Chang WS, Xue Q, Chan CH. Retrodirective array for RFID and microwave tracking beacon applications. *Microwave and Optical Technology Letters*. 2006;48(2):409–11.
- [30] Fontana R, Ameti A, Richley E, Beard L, Guy D. Recent advances in ultra wideband communications systems. In *IEEE Conference on Ultra Wideband Systems and Technologies*. Baltimore, Maryland, May 2002, pp. 129–133.
- [31] Balanis CA. *Antenna theory: analysis and design*. John Wiley & Sons; Hoboken, New Jersey, 2005.
- [32] Lamantia A, Maranesi PG, Radrizzani L. Small-signal model of the Cockcroft-Walton voltage multiplier. *Power Electronics, IEEE Transactions on*. 1994;9(1):18–25.

A Review of Dynamic Wireless Power Transfer for In-Motion Electric Vehicles

Kai Song, Kim Ean Koh, Chunbo Zhu, Jinhai Jiang,
Chao Wang and Xiaoliang Huang

Additional information is available at the end of the chapter

<http://dx.doi.org/10.5772/64331>

Abstract

Dynamic wireless power transfer system (DWPT) in urban area ensures an uninterrupted power supply for electric vehicles (EVs), extending or even providing an infinite driving range with significantly reduced battery capacity. The underground power supply network also saves more space and hence is important in urban areas. It must be noted that the railways have become an indispensable form of public transportation to reduce pollution and traffic congestion. In recent years, there has been a consistent increase in the number of high-speed railways in major cities of China, thereby improving accessibility. Wireless power transfer for train is safer and more robust when compared with conductive power transfer through pantograph mounted on the trains. Direct contact is subject to wear and tear; in particular, the average speed of modern trains has been increasing. When the pressure of pantograph is not sufficient, arcs, variations of the current, and even interruption in power supply may occur. This chapter provides a review of the latest research and development of dynamic wireless power transfer for urban EV and electric train (ET). The following key technology issues have been discussed: (1) power rails and pickups, (2) segmentations and power supply schemes, (3) circuit topologies and dynamic impedance matching, (4) control strategies, and (5) electromagnetic interference.

Keywords: dynamic wireless power transfer, magnetic coupler, circuit topologies, control strategies, electromagnetic interference

1. Introduction

In recent years, studies on DWPT have gained traction especially from The University of Auckland, Korea Advanced Institute of Science and Technology (KAIST), The University of Tokyo, Oak Ridge National Laboratory (ORNL), and many other international institutions. The topics discussed include system modeling, control theories, converter topologies, magnetic coupling optimization, and electromagnetic shielding technologies for DWPT.

The University of Auckland and Conductix-Wampfler manufactured the world's first WPT bus with 30 kW power. A demo ET with 100 kW WPT capability and a 400 m long track without any on-board battery was also constructed [1] as shown in **Figure 1**.

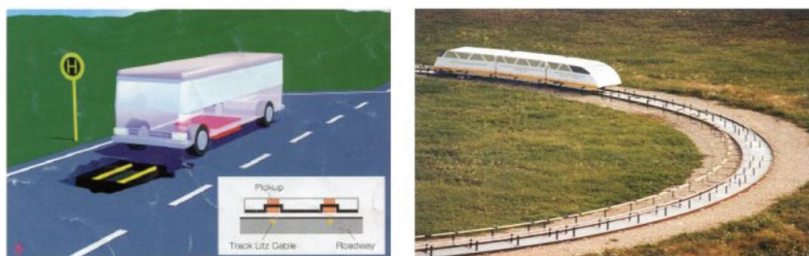


Figure 1. WPT for EV and ET.

KAIST constructed electric buses powered by an online electric vehicle (OLEV) system. The buses are deployed in Gumi city for public transportation, running on two fixed routes covering a total distance of 24 km as shown in **Figure 2**. The OLEV system on these routes is able to supply 100 kW power with 85% of transfer efficiency [2].



Figure 2. KAIST OLEV.

The research in Oak Ridge National Laboratory focuses on coupling configuration, transfer characteristics, medium loss, and magnetic shielding. The dynamic charging system as shown in **Figure 3** constructed by ORNL consists of a full bridge inverter powering two transmitters simultaneously through a series connection. The experimental results show that the positions of the electric vehicle significantly affect the transferred power and efficiency [3].



Figure 3. DWPT system of ORNL.

Researchers in The University of Tokyo proposed using the combination of a feedforward controller and a feedback controller to adjust the duty cycle of the power converters in the DWPT system to achieve optimum efficiency. With the advanced control method, a wireless in-wheel motor is developed as shown in **Figure 4**. The current WPT is from the car body to the in-wheel motor. In future, the wireless in-wheel motor can be powered directly from the ground using a dynamic charging system [4].

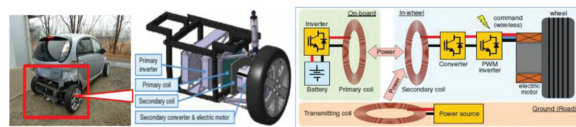


Figure 4. Wireless in-wheel motor.

On the other hand, the Korea Railroad Corporation (KRRI) designed a WPT system for the implementation in railway track. A 1 MW, 128-m-long railway track was developed to demonstrate the dynamic charging technology for EV. The coupling mechanism consists of a long transmitter track and two small U-shaped magnetic ferrites to increase the coupling strength. As a long transmitter track has high inductance, high voltage drop will occur when the current flows through it. In order to reduce this voltage stress, the compensation capacitors are distributed along the track as shown in **Figure 5** [5].

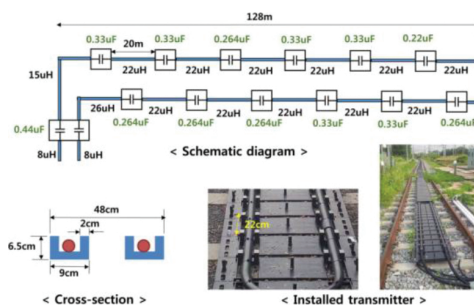


Figure 5. Wireless power rail developed by KRRI.

The researchers from the Japan Railway Technical Research Institute proposed a different design of coupling mechanism for the ET. The transmitters are long bipolar coils, and “figure-8” coils are used as the matching pickups as shown in **Figure 6**. The system is able to transfer 50 kW of power across a 7.5-mm gap with 10-kHz frequency [6].

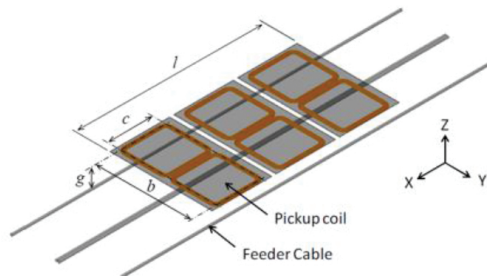


Figure 6. The non-contact power supply system for railway vehicle.

Bombardier Primove from Germany is currently leading in WPT technology for EV and ET. Studies have been primarily conducted for better exploitation of the technology. Apparently, the technical information of the WPT system developed by Bombardier Primove has not been published. In 2013, the company proposed a design shown in **Figure 7** to ensure high reliability when powering the EV. The main DC bus is supplied by k-number of AC/DC substations connected in parallel. This configuration is used to increase the robustness of the system. If one of the AC/DC substations breaks down, that particular substation will be disconnected from the system and other neighboring substations can continue functioning normally, thus avoiding power interruption. Each transmitter cluster is supplied by multiple high-frequency DC/AC inverters in parallel. Similar to the DC bus, the power supply at the AC bus will not be interrupted if an inverter breaks down. At the receiver side, the train contains a DC bus as shown in **Figure 7**. Multiple receivers are supplying to the DC bus simultaneously via AC/DC rectification. The DC bus powers the motor through a controller. If any of the rectifiers is damaged, other receivers can continue providing sufficient power to the DC bus [7].

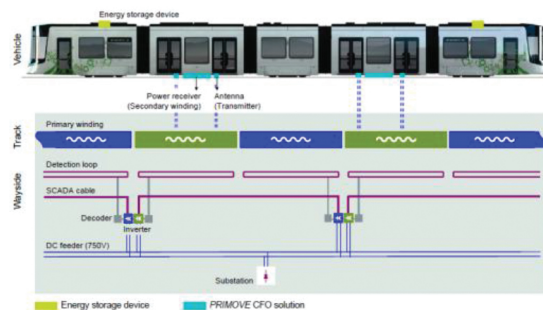


Figure 7. DWPT system for railway vehicle.

The Harbin Institute of Technology demonstrated dynamic charging using segmented transmitters with parallel connections to the inverter [8]. At the receiver side, two layers of flat coils wounded in the same direction are stacked against each other to cancel the points, where transferred power is zero, thereby increasing the overall efficiency. Using the decoupling principle to design the size and position of the two-phase coil, the cross-coupling is cancelled and high efficiency is then achieved at any position [9].

Although several studies have been conducted all over the world yielding exceptional results, factors such as power transfer performance, construction cost, and maintenance cost still require improvement. Other important considerations for practical DWPT implementation include high-power rail, robust control strategies, and EMC.

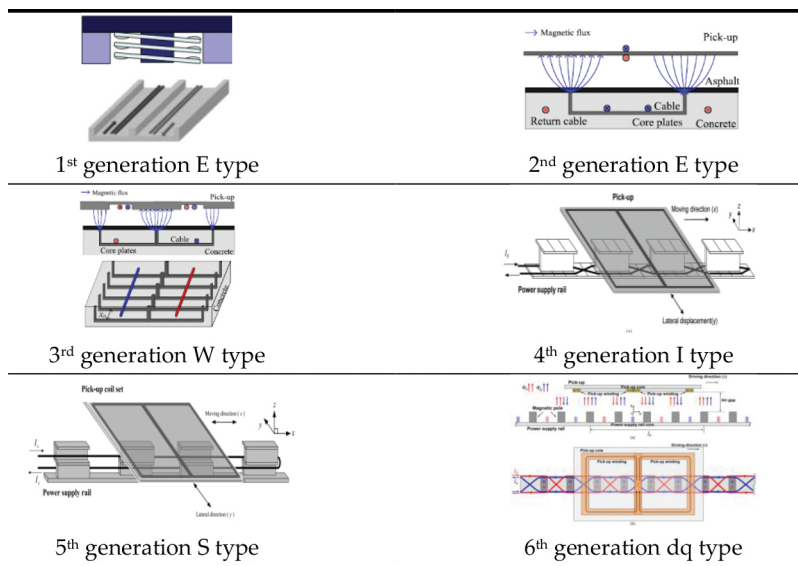
2. Power rails and pickups

Core-less rectangular coils and bipolar coils are the two general types of coils used in WPT. The University of Auckland proposed using long rectangular rails to transfer power. A larger surface area for road construction necessitates less amount of power to be transferred per surface area. The design is also sensitive to lateral displacement of the electric vehicles. Moreover, a high level of magnetic field leakage occurs at both sides of the rail [10]. KAIST proposed an improved version by adding a magnetic core with an optimized design. Compared to the transmitter rail proposed by the University of Auckland, the transfer efficiency and transfer distance are increased. However, the construction cost is also higher.

KAIST presented an advanced coupling mechanism design and optimization technology in their past research. In 2009, the first-generation OLEV was successfully produced. An E-shaped magnetic core is used as the power transmission rail. The air gap is only 1 cm and the transfer efficiency 80% [2]. A U-shaped transmission rail was also proposed in the same year by significantly increasing the transmission gap to 17 cm with an efficiency of 72%. In 2010, a skeleton-type W-shaped magnetic core is proposed, thus further increasing the transfer distance to 20 cm and efficiency to 83% [2]. From 2011 to 2015, researchers from KAIST designed fourth-generation I-shaped bipolar rails and fifth-generation S-shaped bipolar rails with even larger transfer gap, narrower frame, and higher efficiency [2]. With bipolar rails, the magnetic field path is parallel to the moving direction of the vehicle instead of being orthogonal to the moving direction. The new design is well suited for DWPT due to its advantages such as high power density, narrow frame, and therefore lower construction complexity, robust to lateral displacement, and lower magnetic field exposure on both sides of the rail [10–12] (**Tables 1 and 2**).

In 2015, KAIST proposed using a dq-two-phase transmitter rail for cancelling the zero coupling points along the moving direction [13] using the control method which is relatively complex. A double loop control is implemented by detecting the phase of the primary current. The amplitudes and phases of the d-q currents are controlled using a phase-locked loop and DC chopper according to the position of the receiver.

Type	Coreless long coil	Bipolar rail
Merits	Even magnetic field distribution, stable power transfer, coreless, and low manufacturing cost	High power density, narrow design, robust to lateral displacement, low construction complexity, and low level of magnetic field exposure
Demerits	Low power density, sensitive to lateral displacement, large surface area is needed for construction, and high level of magnetic field exposure	Uneven magnetic field distribution, zero coupling point. High cost due to the usage of ferrite core

Table 1. Advantages and disadvantages of commonly used powering rail.**Table 2.** Wireless power rails and receiving pickups developed by KAIST (From generation 1 to 6).

3. Segment and power supply scheme

In order to overcome the issues of low transfer efficiency and high sensitivity to the changing parameters in a centralized power supply system, a new segmented scheme is proposed [14]. The voltage at the 50 Hz AC bus is first stepped up to reduce transmission loss. Then, before the segmented transmitters, the voltage is stepped down via the inverter. Constant current is also used at the transmitters. Efficient converter topologies are also reviewed for implementing a centralized power supply system.

(1) Centralized power supply scheme (**Figure 8**)

With the increasing length of the transmitter rail, the bandwidth of the primary side channel becomes narrower. Therefore, the system is more sensitive to the variations of parameters, and the robustness is decreased. The controller for the centralized power supply is relatively

- a. High requirements of the components due to a single module supporting large power.
- b. The whole rail is activated and causes high loss.
- c. Low reliability due to any breakdown will affect the whole rail.
- d. The efficiency is low when the load is small.
- e. High self-inductance and therefore high voltage across capacitor.
- f. Highly sensitive toward the variations in parameters, causing low stability.

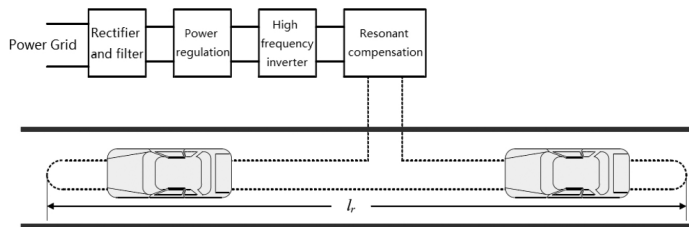


Figure 8. Centralized power supply scheme.

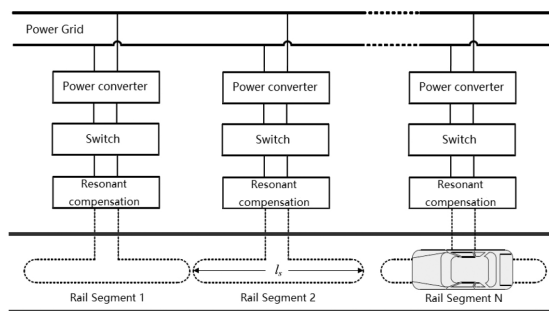


Figure 9. Power frequency scheme—segmented rail mode.

(2) Power frequency scheme—segmented rail mode (**Figure 9**)

The advantages of segmented rails are as follows:

- a. Different segments can be turned on at different time periods, decreasing the power loss;
- b. Smaller-sized power converters;
- c. Higher reliability, when one of the segments breaks down, other segments will still be functioning normally;

- d. Lower self-inductance, less sensitive to variations in parameters, and therefore increasing the system stability.

However, segmented rails also have the following disadvantages:

- a. High number converters, difficult to control and high maintenance and construction cost;
- b. High number of components is required and therefore low reliability of the whole system.

(3) High frequency scheme—segmented rail mode (**Figure 10**)

With segmented rails and centralized power supply, the advantages of this design are as follows:

- a. Lesser power converter units, easier to maintain;
- b. Different segments can be activated at different time periods, lesser power loss;
- c. Lower self-inductance, less sensitive to variations in parameters, increases the system stability.

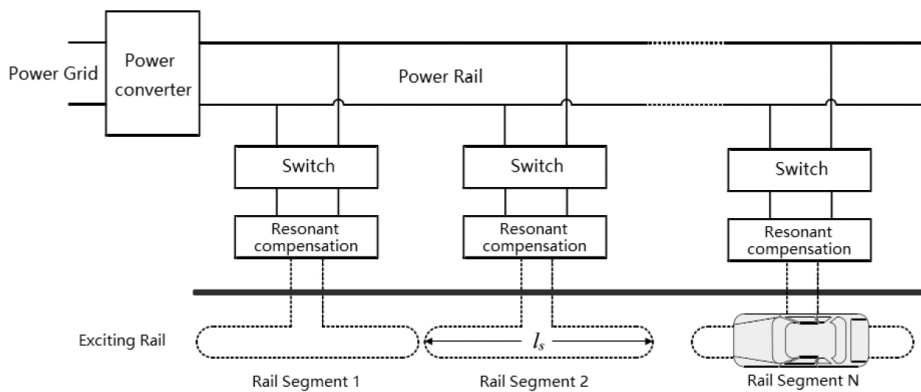


Figure 10. High frequency scheme—segmented rail mode.

However, this design has the following disadvantages:

- a. When the power supply breaks down, all of the segmented rails will stop functioning, thus lowering the system reliability;
- b. High loss in the cable connecting the power supply to the segmented rails;
- c. High capacity power supply and therefore large requirements of the components;

(4) High frequency and high voltage scheme and low voltage and constant current rail mode (**Figure 11**).

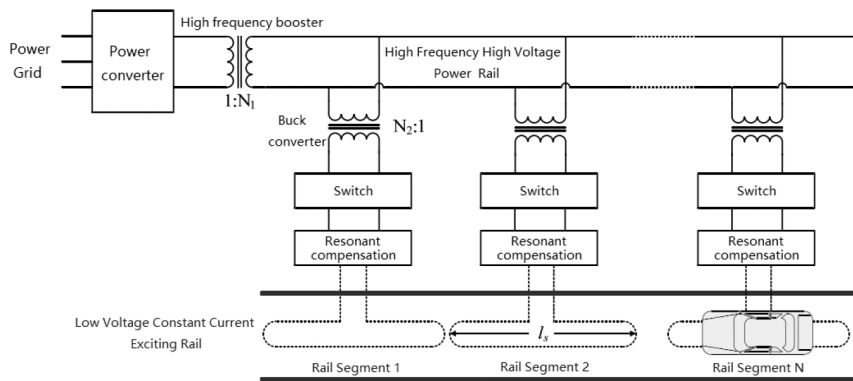


Figure 11. High frequency and high voltage scheme—low voltage and constant current rail mode.

(5) Combination scheme (Figure 12)

This type of rails combines the advantages of abovementioned rails; however, the system is complex and only suitable for a large-scale dynamic charging system.

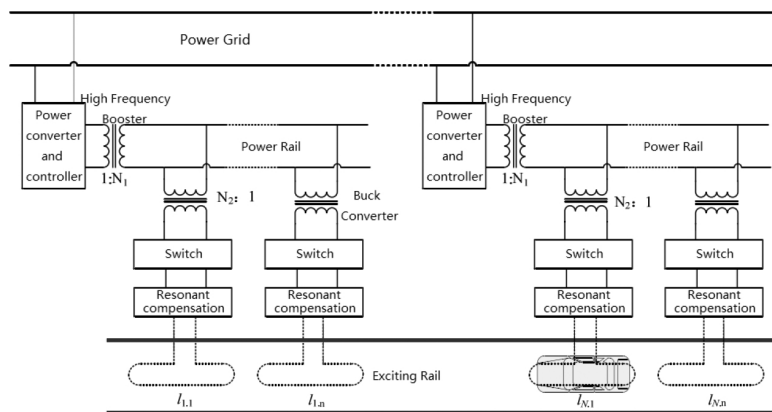


Figure 12. Combined type rail scheme.

4. Circuit topologies and impedance matching

In the DWPT system, the gap between the receiver and transmitter is always changing. Different cars have different heights with respect to the ground and the coupling coefficient will vary significantly. Coupling coefficient is an important parameter in WPT. If the value is too low, the efficiency may drop considerably. Contrarily, frequency splitting phenomena may occur if the coupling coefficient is too high, and the system functions in the unstable

region. Therefore, the circuit topology should be designed to be insensitive to coupling changes.

In order to achieve a steady power supply with variations in coupling and to increase the system stability in the light-load region, an LCLC topology can be used. The current at the primary is kept constant and stress on switches is reduced during on-off. At the receiver side, a parallel-T configuration can increase the tolerance of the system toward coupling variation. The proposed topology is shown in **Figure 13**.

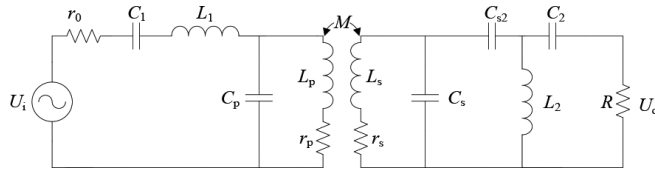


Figure 13. Circuit topology of double LCLC.

The transmitter current is written as follows:

$$i_p = (U_i - U_{r0}) / (\omega_0 L_p) \quad (1)$$

With $\lambda = L_s / L_2 < 1$ as the load coefficient, the receiver output voltage is as follows:

$$U_o = U_{oc} / \lambda = \omega_0 k \sqrt{L_p L_s} I_p / \lambda \quad (2)$$

The output voltage is $1/\lambda$ times the receiver voltage. A step-up voltage converter is used to provide sufficient power when coupling is low, therefore increasing the tolerance of the system against lateral displacement.

The voltage ratio and efficiency are given as follows:

$$\begin{cases} G = MR\lambda / L_0(R\lambda^2 + r_s) + r_0 C_p (M^2 \omega_0^2 + r_p(R\lambda^2 + r_s)) \\ \eta = \omega_0^2 M^2 R \lambda^2 L_0 / (\omega_0^2 M^2 + r_p(R\lambda^2 + r_s))(L_0(R\lambda^2 + r_s) + C_p r_0(\omega_0^2 M^2 + r_p(R\lambda^2 + r_s))) \end{cases} \quad (3)$$

where r_0 is the internal resistance of the inverter circuit, r_p is the resistance of the transmitter, and r_s is the resistance of the receiver.

The power and efficiency curves are given in **Figure 14**. The efficiency is high at the low-coupling region which is particularly important for the DWPT application.

As shown by the curves in **Figure 15**, the efficiency and power are significantly improved for different loads and coupling coefficient compared to series topology.

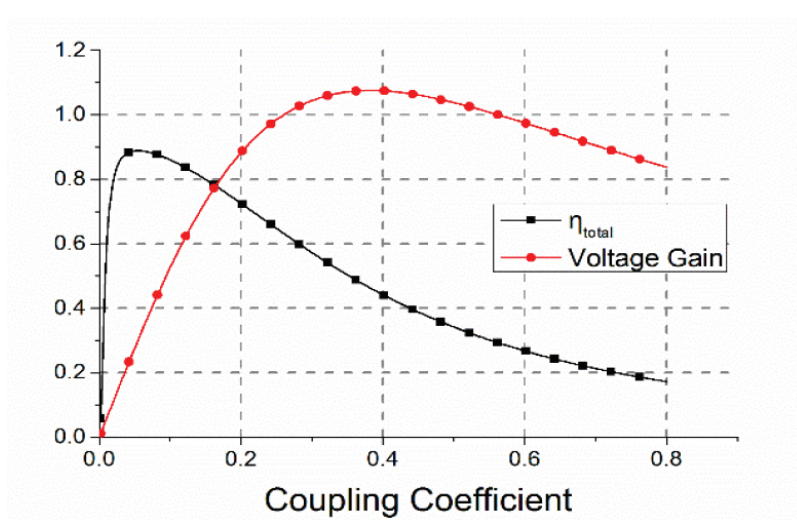


Figure 14. Efficiency and voltage gain vs. coupling coefficient.

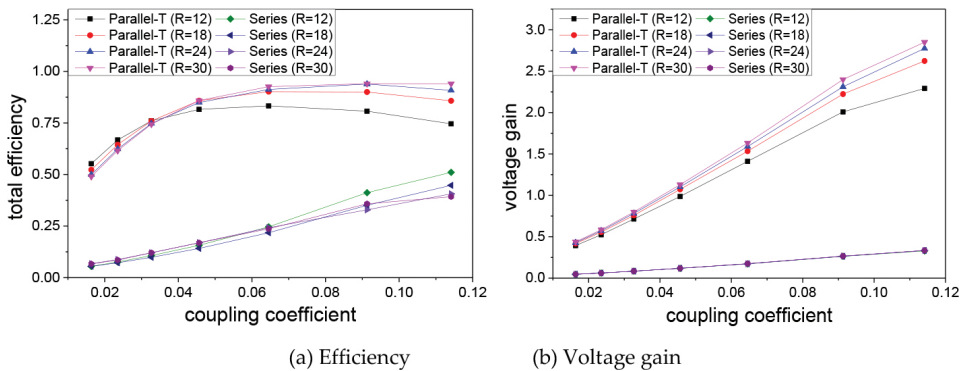


Figure 15. Power and efficiency of the two kinds of structure vs. coupling coefficient.

While designing the circuit of WPT, the compensation is performed under no-load condition. In normal operating condition, frequency tracking is used to ensure resonance by keeping the same phase between primary voltage and primary current [12]. Besides, to ensure the EMC and system stability, control is used to achieve constant current. The magnetic field from the transmitter is in steady state. For example, in the WPT system developed by KAIST, the input voltage of the inverter is adjusted using a three-phase thyristor converter shown in Figure 16 to achieve constant current at the transmitter.

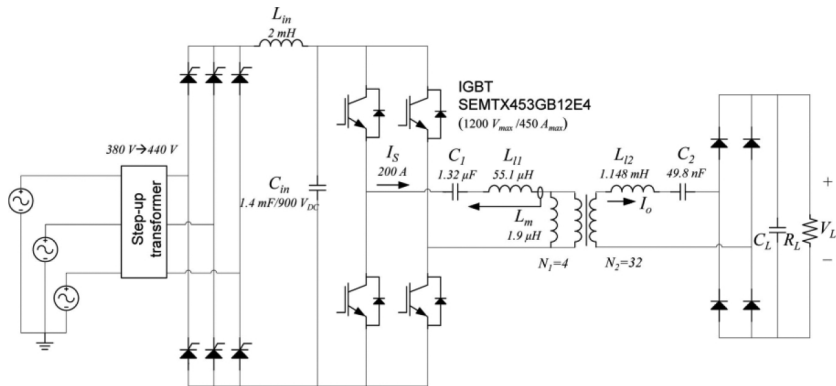


Figure 16. Diagram of the KAIST IPTS showing a power inverter, a power supply rail, and a pickup.

For the secondary side, in order to realize constant current, constant voltage, or constant power, a DC/DC converter is usually implemented. **Figures 17 and 18** show the DC/DC converters used in the WPT systems of the University of Auckland and KAIST [15, 16].

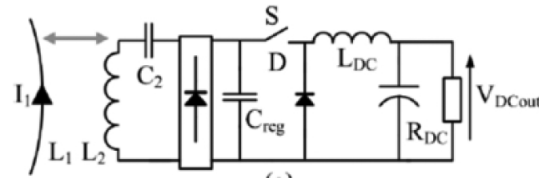


Figure 17. Secondary DC/DC converter.

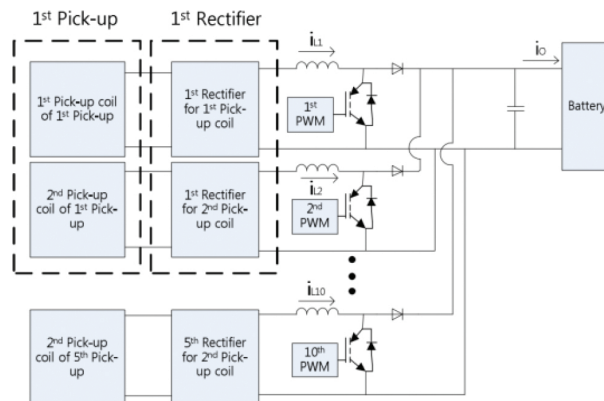


Figure 18. Functional diagram of OLEV power receiver system.

Figure 19 shows a secondary-side circuit which consists of both controllable rectifier and DC/DC converter. SPWM synchronous rectification is employed at the controllable rectifier. The duty cycle of the rectifier is regulated through SPWM; the effective resistance can be adjusted in the range of $R_{load} \sim \infty$. While for a boost converter, the effective resistance can be in the range of $0 \sim \infty$. Therefore, any desired values of the effective resistance can be realized to improve the system overall efficiency.

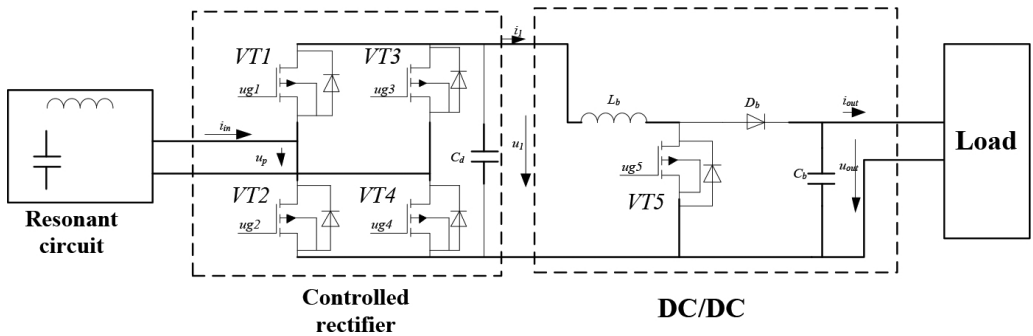


Figure 19. Dynamic impedance adjustment for secondary side pickups.

5. Control strategies

Three types of control were proposed for DWPT: primary control, secondary control, and double-side control. The University of Auckland proposed adjusting the duty cycle of the inverter to control primary resonant current, simplifying the system configuration [17]. KAIST designed constant current control at the primary. A DC/DC converter is added before the inverter, and the DC voltage from the main line is adjusted to achieve constant current for different loads [13]. The main objective of primary control is to produce constant magnetic field, then robust power control can be implemented. The University of Tokyo utilizes secondary control strategy. A buck converter is added after the rectifier [4]. General state space averaging (GSSA) is used to construct the small-signal model. Constant power or maximum efficiency is then realized using PI pole placement [18]. In addition, controllable rectifier and hysteresis comparator are also proposed for implementation at the secondary side to control the output power or maximum efficiency [19]. Double-side control can be with or without communication. ORNL combines the control of both sides, using a closed loop control and frequency adjustment with communication to realize wireless charging [3]. The Hong Kong University proposed simultaneous control of both power and maximum efficiency without communication. The smallest input power is searched to realize constant output power of the inverter [20] (Table 3).

Control strategy	Primary control	Secondary control	Both side control	
			With close-loop communication	Without close-loop communication
Merits	Constant current in transmitter, steady magnetic field, no need to consider reflected impedance	Constant charging current, constant charging voltage, or maximum efficiency	Both desired power and maximum efficiency are achievable simultaneously	Both desired power and maximum efficiency are achievable simultaneously
Demerits	Unable to control for maximum efficiency, limited control of output load, and constant current charging is not realizable	Adjustable range of the secondary side is limited, and accurate model is required	Additional wireless communication is required, lower the system reliability and real-time performance	Conflict control between primary side and secondary side

Table 3. Comparison of advantages and disadvantages of various control strategies.

The DWPT system is subject to disturbances such as variation of mutual inductance caused by movement of the vehicles. New robust control strategies, which are more superior to PID controllers [4,18,19] in disturbance suppression, are currently being studied.

6. Electromagnetic interference

The DWPT uses a high-frequency, strong magnetic field to transfer power wirelessly. The EMC is an important consideration as the DPWT system is surrounded by many sensitive electronic circuits. The requirements include shielding design, frequency allocation, and grounding design. According to the standard set by the International Commission on Non-Ionizing Radiation Protection (ICNIRP), the current density exposed to the public is 200 mA/m^2 , when the frequency is 100 kHz. The values may affect the nerve system of human body. The limit of specific absorption rate (SAR) is 2 W/kg and power density is 10 W/m^2 ; if the exposure to the human body is higher than these limits, heating of the human tissues may occur (**Table 4**).

Shielding method	Metal conductor	Magnetic material	Active shielding	Resonant reactive shielding
Merits	Fully enclosed metal conductor housing provide excellent shielding effect	Magnetic field shaping, increasing coupling coefficient and therefore low loss	Flexible placement, good shielding effect	Does not consume power from the system, controllable
Demerits	Eddy loss affecting the system efficiency	Limited shielding effect	Additional coil lower the system efficiency	Difficult to design, complex configuration

Table 4. Comparison of merit and demerit of various magnetic shielding methods.

The suppression of the leakage field can be divided into active shielding and passive shielding. In passive shielding, a magnetic path is created using magnetic material or canceling field using a low magnetic permeability metallic conductor [21–23]. The self-inductance and mutual inductance are increased when using magnetic material. The magnetic flux distribution is improved due to higher coupling coefficient, and transfer loss is decreased. However, the shielding effect is limited. Metallic shield is widely used in a high-frequency magnetic field to suppress electromagnetic interference. Both KAIST and ORNL utilize this kind of shielding method. The advantages include simple design and easy to use. However, metallic shielding cannot cover the transmitter and receiver completely. The exposed conductor is subject to friction and eddy current which will increase the heat loss. KAIST proposed a new active shielding method in 2015. A conventional ferrite plate is embedded in multiple metallic sheets as shown in **Figure 20**. Experimental results show that the magnetic interference is effectively reduced [24].

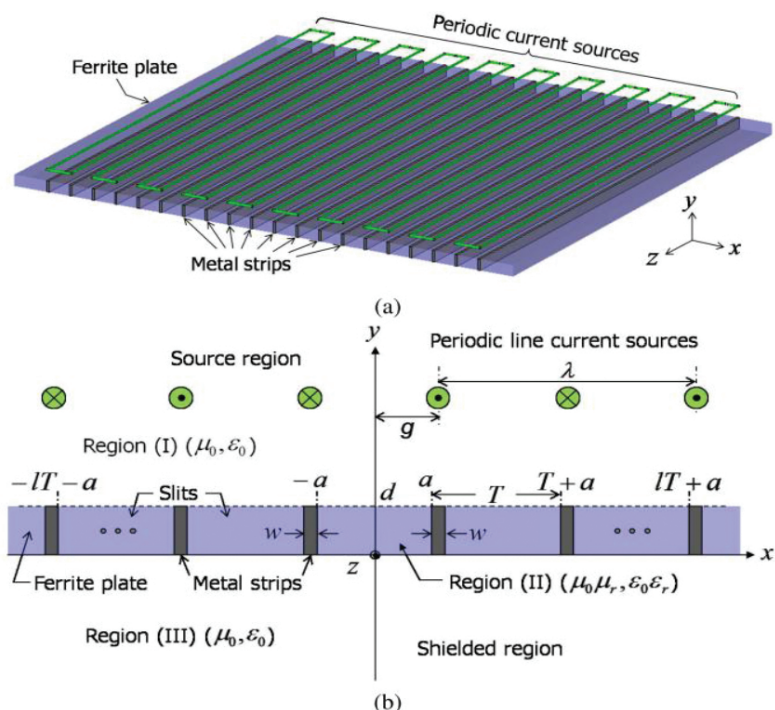


Figure 20. Ferrite shielding structure using an embedded metal sheet.

Regarding active shielding, additional coils with or without power supply are implemented at the WPT system to create a cancelling field as shown in **Figure 21**. Compared to metallic shielding, the space required is smaller.

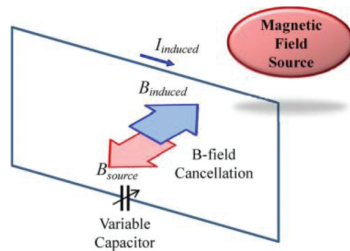


Figure 21. Magnetic field cancellation using a resonant coil.

KAIST published a paper in 2013, proposing an active shielding method using a resonant coil. A switching array is used to change the values of compensated capacitors, thereby controlling the amplitude and phase of the cancelling field. An experiment was performed using green public transportation [25]. In 2015, an improved version using double loop and phase adjustment to achieve resonance was proposed to achieve an active shielding without power supply. The shielding coils are placed at the side of the coupling mechanism as shown in **Figure 22**. The current induced by leakage field is then sensed. Magnetic field with the same amplitude but opposite polarity with the leakage is then created for field cancellation [26].

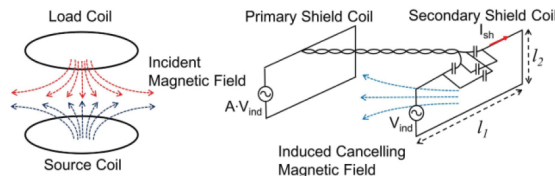


Figure 22. Resonant reactive power shielding with double coils and four capacitors.

In 2013, ORNL proposed using an aluminum board to reduce electromagnetic interference [27]. As shown in **Figure 23**, a 1-mm-thick aluminum shield is placed above the cables. The magnetic field measured at the passenger-side front tire is reduced from $18.72 \mu\text{T}$ to $3.22 \mu\text{T}$.

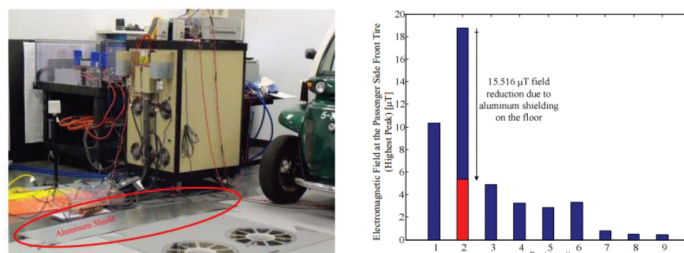


Figure 23. Suppression of magnetic field after adding aluminum plate and its effect.

7. Conclusions

With the advancement of EV and ET, the significance of DWPT has been consistently growing. Recent developments in DWPT for EV and ET have been presented throughout this chapter. Five different aspects of this technology, such as power rail and pickup design, power supply schemes, circuit topologies and impedance matching, control strategies, and EMC, are reviewed. Despite obtaining significant results post study in this field, some issues of concern are yet to be resolved. Previous results as well as the challenges in deployment of DWPT in real application have been highlighted in this chapter.

Author details

Kai Song^{1*}, Kim Ean Koh², Chunbo Zhu¹, Jinhai Jiang¹, Chao Wang¹ and Xiaoliang Huang²

*Address all correspondence to: kaisong@hit.edu.cn

1 School of Electrical Engineering, Harbin Institute of Technology, Harbin, China

2 Department of Electrical Engineering, The University of Tokyo, Tokyo, Japan

References

- [1] Chen L, Nagendra G.R, Boys J.T, Covic G.A. Double-Coupled Systems for IPT Roadway Applications. *IEEE Journal of Emerging and Selected Topics in Power Electronics*. 2015;3(1):37–49. DOI: 10.1109/JESTPE.2014.2325943
- [2] Choi S.Y, Gu B.W, Jeong S.Y, Rim C.T. Advances in Wireless Power Transfer Systems for Roadway-Powered Electric Vehicles. *IEEE Journal of Emerging and Selected Topics in Power Electronics*. 2015;3(1):18–36. DOI: 10.1109/JESTPE.2014.2343674
- [3] Miller J.M, Onar O.C, Chinthalvali M. Primary-Side Power Flow Control of Wireless Power Transfer for Electric Vehicle Charging. *IEEE Journal of Emerging and Selected Topics in Power Electronics*. 2015;3(1):147–162. DOI: 10.1109/JESTPE.2014.2382569
- [4] Kobayashi D, Imra T, Hori Y. Real-time coupling coefficient estimation and maximum efficiency control on dynamic wireless power transfer for electric vehicles. In: *IEEE WoW 2015 - IEEE PELS Workshop on Emerging Technologies: Wireless Power*, Proceedings ; June 5, 2015 - June 6, 2015; Daejeon, Korea. Piscataway, United States: Institute of Electrical and Electronics Engineers Inc.; 2015. p. 1–6. DOI: 10.1109/WoW.2015.7132799

- [5] Kim J.H, Lee B.S, Lee J.H, Lee S.H, Park C.B, Jung S.M. Development of 1-MW Inductive Power Transfer System for a High-Speed Train. *IEEE Transactions on Industrial Electronics*. 2015;62(10):6242–6250. DOI: 10.1109/TIE.2015.2417122
- [6] Ukita K, Kashiwagi T, Sakamoto Y, Sasakawa T. Evaluation of a non-contact power supply system with a figure-of-eight coil for railway vehicles. In: *IEEE WoW 2015 - IEEE PELS Workshop on Emerging Technologies: Wireless Power, Proceedings*; June 5, 2015 - June 6, 2015; Daejeon, Korea. Piscataway, United States: Institute of Electrical and Electronics Engineers Inc.; 2015. p. 1–6. DOI: 10.1109/WoW.2015.7132807
- [7] Winter J, Mayer S, Kaimer S, Seitz P, Pagenkopf J, Streit S. Inductive power supply for heavy rail vehicles. In: *2013 3rd International Electric Drives Production Conference, EDPC 2013 - Proceedings*; October 29, 2013 - October 30, 2013; Nuremberg, Germany. Piscataway, United States: IEEE Computer Society; 2013. p. 1–9. DOI: 10.1109/EDPC.2013.6689749
- [8] Song K, Zhu C, Li Y, Guo Y, Jiang J, Zhang J. Wireless power transfer technology for electric vehicle dynamic charging using multi-parallel primary coils. *Zhongguo Dianji Gongcheng Xuebao/Proceedings of the Chinese Society of Electrical Engineering*. 2015;35(17):4445–4453. DOI: 10.13334/j.0258-8013.pcsee.2015.17.020
- [9] Zhu C, Song K, Wei G, Zhang Q. Novel power receiver for dynamic wireless power transfer system. In: *Industrial Electronics Society, IECON 2015 - 41st Annual Conference of the IEEE*; 9 November 2015-12 November 2015; Yokohama. Piscataway, United States: Institute of Electrical and Electronics Engineers Inc.; 2015. p. 002247– 002251. DOI: 10.1109/IECON.2015.7392436
- [10] Chen L, Nagendra G.R, Boys J.T, Covic G.A. Ultraslim S-Type Power Supply Rails for Roadway-Powered Electric Vehicles. *IEEE Transactions on Power Electronics*. 2015;30(11):6456–6468. DOI: 10.1109/TPEL.2015.2444894
- [11] Lee W.Y, Huh J, Choi S.Y, Thai X.V, Kim J.H, Al-Ammar E.A. Finite-Width Magnetic Mirror Models of Mono and Dual Coils for Wireless Electric Vehicles. *IEEE Transactions on Power Electronics*. 2013;28(3):1413–1428. DOI: 10.1109/TPEL.2012.2206404
- [12] Huh J, Lee S.W, Lee W.Y, Cho G.H, Rim C.T. Narrow-Width Inductive Power Transfer System for Online Electrical Vehicles. *IEEE Transactions on Power Electronics*. 2011;26(12):3666–3679. DOI: 10.1109/TPEL.2011.2160972
- [13] Park C, Lee S, Jeong S.Y, Cho G.H, Rim C.T. Uniform Power I-Type Inductive Power Transfer System With DQ Power Supply Rails for On-Line Electric Vehicles. *IEEE Transactions on Power Electronics*. 2015;30(11):6446–6455. DOI: 10.1109/TPEL.2015.2420372
- [14] Tian Y. Research on Key Issues of Sectional Track-Based Wireless Power Supply Technology for Electric Vehicles [thesis]. Chongqing, China: Chongqing University; 2012.

- [15] Keeling N.A, Covic G.A, Boys J.T. A Unity-Power-Factor IPT Pickup for High-Power Applications. *IEEE Transactions on Industrial Electronics*. 2010;57(2):744–751. DOI: 10.1109/TIE.2009.2027255
- [16] Shin J, Shin S, Kim Y, Ahn S, Lee S, Jung G, et al. Design and Implementation of Shaped Magnetic-Resonance-Based Wireless Power Transfer System for Roadway-Powered Moving Electric Vehicles. *IEEE Transactions on Industrial Electronics*. 2014;61(3):1179–1192. DOI: 10.1109/TIE.2013.2258294
- [17] Abdolkhani A, Hu A.P. Improved autonomous current-fed push-pull resonant inverter. *Iet Power Electronics*. 2014;7(8):2103–2110. DOI: 10.1049/iet-pel.2013.0749
- [18] Hata K, Imura T, Hori Y. Maximum efficiency control of wireless power transfer via magnetic resonant coupling considering dynamics of DC-DC converter for moving electric vehicles. In: Conference Proceedings - IEEE Applied Power Electronics Conference and Exposition - APEC; March 15, 2015 - March 19, 2015; Charlotte, NC, United states. Piscataway, United States: Institute of Electrical and Electronics Engineers Inc.; 2015. p. 3301–3306. DOI: 10.1109/APEC.2015.7104826
- [19] Gunji D, Imura T, Fujimoto H. Envelope model of load voltage on series-series compensated wireless power transfer via magnetic resonance coupling. In: IEEE WoW 2015 - IEEE PELS Workshop on Emerging Technologies: Wireless Power, Proceedings; June 5, 2015 - June 6, 2015; Daejeon, Korea. Piscataway, United States: Institute of Electrical and Electronics Engineers Inc.; 2015. p. 1–6. DOI: 10.1109/WoW.2015.7132853
- [20] Zhong W.X, Hui S.Y.R. Maximum Energy Efficiency Tracking for Wireless Power Transfer Systems. *IEEE Transactions on Power Electronics*. 2015;30(7):4025–4034. DOI: 10.1109/TPEL.2014.2351496
- [21] Kim J, Kim H, Kim M, Ahn S, Kim J, Kim J. Analysis of EMF noise from the receiving coil topologies for wireless power transfer. In: cccc2012 Asia-Pacific Symposium on Electromagnetic Compatibility, APEMC 2012 - Proceedings; May 21, 2012 - May 24, 2012; Singapore, Singapore. Piscataway, United States: IEEE Computer Society; 2012. p. 645–648. DOI: 10.1109/APEMC.2012.6237964
- [22] Kim H, Song C, Kim J, Kim J. Shielded Coil Structure Suppressing Leakage Magnetic Field from 100W-Class Wireless Power Transfer System with Higher Efficiency. *International Microwave Workshop Series on Innovative Wireless Power Transmission: Technologies*. 2012;16(3):83–86. DOI: 10.1109/IMWS.2012.6215825
- [23] Ahn S, Park H.H, Choi C.S, Kim J, Song E, Paek H.B, et al. Reduction of electromagnetic field (EMF) of wireless power transfer system using quadruple coil for laptop applications. In: 2012 IEEE MTT-S International Microwave Workshop Series on Innovative Wireless Power Transmission: Technologies, Systems, and Applications, IMWS-IWPT 2012 - Proceedings; May 10, 2012 - May 11, 2012; Kyoto, Japan. Piscataway, United States: IEEE Computer Society; 2012. p. 65–68. DOI: 10.1109/IMWS.2012.6215821

- [24] Park H.H, Lwon J.H, Kwak S.I, Ahn S. Magnetic Shielding Analysis of a Ferrite Plate with a Periodic Metal Strip. *IEEE Transactions on Magnetics*. 2015;51(8):1–8. DOI: 10.1109/TMAG.2015.2425796
- [25] Kim J, Kim J, Kong S, Kim H, Suh I.S, Suh N.P, et al. Coil Design and Shielding Methods for a Magnetic Resonant Wireless Power Transfer System. *Proceedings of the IEEE*. 2013;101(6):1332–1342. DOI: 10.1109/JPROC.2013.2247551
- [26] Moon H, Kim S, Park H.H, Ahn S. Design of a Resonant Reactive Shield With Double Coils and a Phase Shifter for Wireless Charging of Electric Vehicles. *IEEE Transactions on Magnetics*. 2015;51(3):1–4. DOI: 10.1109/TMAG.2014.2360701
- [27] Ahn S, Park J, Song T, Lee H, Byun J, Kang D, et al. Low frequency electromagnetic field reduction techniques for the On-Line Electric Vehicle (OLEV). In: *IEEE International Symposium on Electromagnetic Compatibility*; July 25, 2010 - July 30, 2010; Fort Lauderdale, FL, United states. Piscataway, United States: Institute of Electrical and Electronics Engineers Inc.; 2010. p. 625–630. DOI: 10.1109/ISEMC.2010.5711349